UNIVERSIDADE ESTADUAL DE CAMPINAS
FACULDADE DE ENGENHARIA MECÂNICA

CRISTIANO PIMENTA SILVA

A Fast Numerical Framework to Compute Acoustic Scattering by Poro-elastic Plates of Arbitrary Geometry

Uma Metodologia Numérica Rápida para o Cálculo de Espalhamento Acústico em Placas Poro-elásticas de Geometrias Arbritárias

CAMPINAS
2018

Cristiano Pimenta Silva

A Fast Numerical Framework to Compute Acoustic Scattering by Poro-elastic Plates of Arbitrary Geometry

Uma Metodologia Numérica Rápida para o Cálculo de Espalhamento Acústico em Placas Poro-elásticas de Geometrias Arbritárias

Dissertation presented to the School of Mechanical Engineering of the University of Campinas in partial fulfillment of the requirements for the degree of Master in Mechanical Engineering, in the area of Thermal and Fluids.

Dissertação apresentada à Faculdade de Engenharia Mecânica da Universidade Estadual de Campinas como parte dos requisitos exigidos para a obtenção do título de Mestre em Engenharia Mecânica na área de Térmica e Fluidos.

Orientador: William Roberto Wolf

Este exemplar corresponde à versão final da dissertação defendida pelo aluno Cristiano Pimenta Silva, e orientada pelo Prof. Dr. William Roberto Wolf.

Assinatura do Orientador

Campinas

2018

Agência(s) de fomento e nº(s) de processo(s): CAPES, 1581546

Ficha catalográfica
Universidade Estadual de Campinas
Biblioteca da Área de Engenharia e Arquitetura
Luciana Pietrosanto Milla - CRB 8/8129

Si38f

Silva, Cristiano Pimenta, 1987-
A fast numerical framework to compute acoustic scattering by poro-elastic plates of arbitrary geometry / Cristiano Pimenta Silva. – Campinas, SP : [s.n.], 2018.

Orientador: William Roberto Wolf.
Dissertação (mestrado) – Universidade Estadual de Campinas, Faculdade de Engenharia Mecânica.

1. Interação fluido-estrutura. 2. Controle de ruído. 3. Métodos de elementos de contorno. 4. Porosidade. 5. Aeroelasticidade. I. Wolf, William Roberto, 1980-. II. Universidade Estadual de Campinas. Faculdade de Engenharia Mecânica. III. Título.

Informações para Biblioteca Digital

Título em outro idioma: Uma metodologia numérica rápida para o cálculo de espalhamento acústico em placas poro-elasticas de geometrias arbritárias
Palavras-chave em inglês:
Fluid-structure interaction
Noise control
Contour element methods
Porosity
Aeroelasticity
Área de concentração: Térmica e Fluídos
Titulação: Mestre em Engenharia Mecânica
Banca examinadora:
William Roberto Wolf [Orientador]
Marcelo Leite Ribeiro
Flávio de Campos Bannwart
Data de defesa: 05-03-2018
Programa de Pós-Graduação: Engenharia Mecânica

UNIVERSIDADE ESTADUAL DE CAMPINAS

FACULDADE DE ENGENHARIA MECÂNICA

COMISSÃO DE PÓS-GRADUAÇÃO EM ENGENHARIA MECÂNICA

DEPARTAMENTO DE TERMICA E FLUIDOS

DISSERTAÇÃO DE MESTRADO ACADÊMICO

A Fast Numerical Framework to Compute Acoustic Scattering by Poro-elastic Plates of Arbitrary Geometry

Uma Metodologia Numérica Rápida para o Cálculo de Espalhamento Acústico em Placas Poro-elásticas de Geometrias Arbritárias

Autor: Cristiano Pimenta Silva

Orientador: William Roberto Wolf

A Banca Examinadora composta pelos membros abaixo aprovou esta dissertação:

Prof. Dr. William Roberto Wolf

UNICAMP

Prof. Dr. Marcelo Leite Ribeiro

USP

Prof. Dr. Flávio de Campos Bannwart

UNICAMP

A Ata da defesa com as respectivas assinaturas dos membros encontra-se no processo de vida acadêmica do aluno.

Campinas, 05 de Março de 2018.

I dedicate this dissertation to the loves of my life ....
Carolina and Jão

Acknowledgments

I would first like to many thanks to my adviser, Professor William Wolf, for his support and encouragement during the development of this dissertation. The door to Prof. Wolf office was always open whenever I ran into a trouble spot or had a question about my research or writing. He consistently allowed this paper to be my own work, but steered me in the right the direction whenever he thought I needed it. He is an inspiration to make things different and better.

I would also like to thank Professors Flávio Bannwart and Marcelo Ribeiro, who served on my dissertation reading committee, and Professors José Arruda and Flávio Bannwart who served on my qualification examination committee.

I gratefully acknowledge the financial support received from CNPq as a MSc scholarship. I also thank the National Center for High Performance Computing, CENAPAD-SP, and CEPID-CeMEAI for providing access to the Euler cluster. The financial support from the US Army Research Laboratory is also gratefully acknowledged. We thank Dr. Tim Pritchett and Dr. Rajneesh Singh, from ARL, for supporting this research.

I wish to thank all the members from Professor Wolf's group for the great time during this journey. I would like to give special thanks to my friends Walter Ramirez, Schiavo, Miotto, Túlio, Bruno Backes, Brenner, Paulo, Hugo, Gabriel, Lucas and Vitor.

I thank all my family for their love and kindness. I wish to give a special thanks to my brothers Ciro and Célio for always encourage me.

Finally, I must express my very profound gratitude to my wife Carolina for providing me with unfailing support and continuous encouragement throughout my years of study and through the process of researching and writing this dissertation. This accomplishment would not have been possible without her. Many thanks my lover.

If you don't like how things are, change it!
You're not a tree.
Jim Rohn

Resumo

Uma metodologia numérica de baixo custo computacional é apresentada para o cálculo de espalhamento acústico em placas poro-elásticas de geometrias arbitrárias. O método de elementos de contorno, BEM, é aplicado para resolver a equação de Helmholtz submetida a condições de contorno relacionadas às vibrações estruturais da placa. Esta análise é realizada reescrevendo as condições de contorno do BEM em termos de uma base modal da placa poro-elástica que é calculada por uma ferramenta numérica que resolve o problema estrutural. A formulação atual permite uma solução direta do problema de interação fluido-estrutura completamente acoplado. A fim de acelerar a solução dos grandes sistemas lineares densos decorrentes da formulação BEM em problemas tridimensionais, um método de multipólos rápidos, FMM, com multi-níveis adaptativos de banda larga é empregado. Um estudo paramétrico é realizado para o espalhamento acústico de bordos de fuga para várias fontes acústicas, representativas de vórtices turbulentos não correlacionados ou de um jato turbulento não compacto. Os mecanismos físicos relacionados à redução de ruído devido à porosidade e elasticidade em frequências baixas e altas são discutidos. A redução de ruído pela combinação de porosidade e elasticidade com bordos de fuga enflexados e com extensões de serrilhados é investigada. As aplicações de espalhamento acústico também são apresentadas para aplicações aquáticas, onde as reduções de ruído são mais efetivas. Em geral, este trabalho mostra que as placas elásticas finitas são mais efetivas na redução do ruído espalhado para frequências mais altas. Por outro lado, a porosidade é mais eficaz na redução de ruído espalhado para frequências mais baixas. Os resultados demonstram que a elasticidade e a porosidade podem ser combinadas com bordos de fuga enflexados e com serrilhados no bordo de fuga para reduzir o ruído espalhado em um espectro mais amplo de freqüências para placas poro-elásticas. Diferentes configurações de interação fluido-estrutura são analisadas para placas com alongamentos baixos e altos. Uma avaliação do espalhamento acústico por placas isotrópicas metálicas e anisotrópicas de materias compósitos também é apresentada. Com a ferramenta numérica proposta, novos dispositivos podem ser projetados e otimizados para obter um espalhamento acústico mais eficiente para aplicações aéreas e aquáticas.

Palavras-chave: Interação fluido estrutura, redução de ruído, porosidade, elasticidade, ruído de bordo de fuga, materiais compósitos, método de multipolos rápidos, método de elementos de contorno.

Abstract

We present a fast numerical framework for the computation of acoustic scattering by poro-elastic plates of arbitrary geometries. A boundary element method, BEM, is applied to solve the Helmholtz equation subjected to boundary conditions related to structural vibrations. This analysis is performed by rewriting the BEM boundary conditions in terms of a modal basis of the poro-elastic plate which is computed by a structural solver. The current formulation allows a direct solution of the fully coupled fluid-structure interaction problem. In order to accelerate the solution of the large dense linear systems arising from the BEM formulation in three-dimensional problems, a wideband adaptive multi-level fast multipole method, FMM, is employed. A parametric study is carried out for the trailing-edge scattering of sample acoustic sources, representative of either uncorrelated turbulent eddies or a non-compact turbulent jet. We discuss about the physical mechanisms related to the reduction of noise scattering due to porosity and elasticity at low and high frequencies. Noise reduction by the combination of porosity and elasticity with swept and serrated trailing edges is demonstrated. Applications of acoustic scattering are also shown for underwater applications, where the most effective noise reductions are obtained. Overall, it is shown that finite elastic plates are more effective in reducing the scattered noise at higher frequencies. On the other hand, porosity is more effective in reducing the radiated sound for lower frequencies. Results demonstrate that elasticity and porosity can be combined with trailing-edge sweep and serrations to reduce the scattered noise at a broad range of frequencies for poro-elastic plates. Different fluid-structure interaction configurations are analyzed for plates of low and high aspect ratios. We also present an assessment of noise scattering by isotropic metallic and anisotropic composite plates. With the current numerical framework, novel low-noise-emission devices can be designed for aerial and underwater applications.

Keywords: Fluid-structure interaction, noise reduction, porosity, elasticity, trailing-edge noise, composite materials, fast multipole method, boundary element method.

List of Figures

List of Tables

List of Symbols

Latin Letters

B_0	bending stiffness
B	bending stiffness modified by porosity
c_0	speed of sound
D_{ij}	bending stiffness tensor
E	Young's modulus
G	free-field Green's function
h	plate thickness
$h_n^{(1)}$	spherical Hankel function of the first king and order n
i	imaginary number
j_n	spherical Bessel function of order n
k_0	acoustic wavenumber
k_B	bending wavenumber
k_x	bending wavenumber component along x-axis
k_y	bending wavenumber component along y-axis
K_R	Rayleigh conductivity
L	reference chord length
t	time
m	mass per unit area
n	normal direction
p	acoustic pressure
P_n	Legendre polynomial of degree n
P_n^m	associated Legendre functions
R	pore radius
$\mathcal{S}$	acoustic source
w	plate displacement
w_a	fluid displacement in the pores
Y_n^m	spherical harmonics
x, y, z	Cartesian components

Greek Letters

α_H	open area fraction
β	modal basis eigenvalue (non-dimensional frequency)
ϵ	intrinsic fluid load factor
λ	wavelength
Λ	sweep angle
ν	poisson ratio
ρ_f	fluid density
ρ_s	surface density
ϕ	modal basis eigenvector
Ω	vacuum bending wave Mach number
ω	angular frequency
ω_c	coincidence frequency

Acronyms

BEM	Boundary Element Method
CSM	Collocation Spectral Method
FEM	Finite Element Method
FMM	Fast Multipole Method
P2M	Particle-to-multipole
M2M	Multipole-to-multipole
M2L	Multipole-to-local
L2L	Local-to-local
L2P	Local-to-particle
P2P	Particle-to-particle
PWL	Sound Power Level
RMS	Root-mean-square

Contents

1 INTRODUCTION

The convection of turbulent structures past an airfoil trailing edge leads to noise generation through a scattering mechanism (Ffowcs Williams and Hall, 1970). In this sense, the unsteady flow generates surface pressure fluctuations which are scattered and propagated to the far-field (Curle, 1955). Several problems in engineering involve noise scattering by solid surfaces; for example, the development of turbulent boundary layers along an airfoil finds application in the noise generated by wings, rotorcrafts, wind turbines and high-lift devices. In these cases, trailing-edge noise is a fundamental mechanism of noise generation (Ffowcs Williams and Hall, 1970) and it remains one of the hardest to control as it depends on a complex interaction of turbulent flow, acoustics and material properties.

As an impressive solution from nature, owls possess the ability to fly and hunt silently, even with very low ambient noise levels (Bachmann *et. al*, 2012; Sarradj *et. al*, 2011; Geyer *et. al*, 2013; Chen *et. al*, 2012). The low self-noise of owls is attributed to their wing and feather structure, which consist of both *serrated* and *swept poro-elastic* trailing edges that completely eliminate airfoil noise in the audible frequency range (see Fig. 1.1). If we can emulate and understand poro-elastic edges using computational techniques it will be possible to utilise innovative owl-inspired airfoil technology in the next generation of aeroengines, rotorcrafts, wind turbines, cooling fans and wings that will be quiet, efficient and reduce environmental noise pollution.

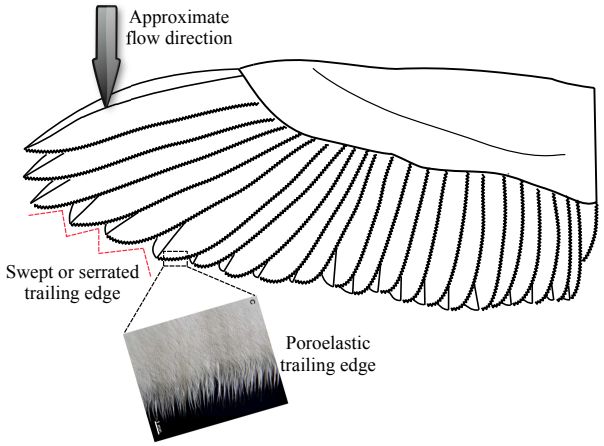

Figure 1.1: Owl wing features: serrated and poro-elastic trailing edge.

Recently, Jaworski and Peake (2013) performed a theoretical analysis and demonstrated that the noise scattered by a trailing edge can be mitigated by the

application of edge elasticity and porosity for certain parameter ranges. The Wiener-Hopf technique was employed to solve the acoustic scattering problem including the effects of the free-stream flow velocity U. In this theoretical analysis, the assumption of a semi-infinite poro-elastic edge is made and, therefore, its application is well suited for trailing-edge scattering in the high-frequency regime. In order to investigate how the far-field acoustic power scales, these authors carried out an asymptotic analysis of porous and elastic edges and compared with a rigid impermeable one which has the well-known U^5 dependence according to Ffowcs Williams and Hall (1970). In this sense, the far-field acoustic power for a porous edge reveals to scale proportional to U^6 and, for an elastic edge, it presents a scaling with U^7. It is shown that the poro-elastic edge produces the weakest edge amplification but no considerable modification in the velocity exponent over the frequency range of interest to the owl noise. The human hearing range hints that flow velocity exponents of order 6 or greater are easy to obtain for the poro-elastic edge at low frequencies, and that the edge properties may be custom-designed to produce improved noise reductions over a wider frequency range in the human audition.

More recently, Ayton (2016) presented a theoretical formulation to investigate the scattered sound by a finite rigid plate with a two-dimensional poro-elastic plate extension interacting with an acoustic source. In this work, the effects of porosity and elasticity were evaluated for different lengths of the plate extension. The problem was also solved using the Wiener-Hopf technique and the importance of having a finite chord-length effects were taken into account, mainly the interaction of the rigid leading-edge secondary diffraction combined with the acoustic scattering along the poro-elastic trailing edge. Results show that the length of the plate extension modify the phase shift between the leading and trailing-edge radiation indicating that constructive or destructive interference in the sound scattering can occur. The effects of porosity are more pronounced for low frequencies and became more efficient as the length of the plate extension was increased. The length of the plate extension was shown to change the behavior of the elasticity effects. Small chord lengths induced vibration of the first modes of the structural problem, which interacted with the acoustic scattering. It was demonstrated that the length of the poro-elastic section is a key parameter in the reduction of noise levels and longer plate extensions permit more the appearance of further resonant modes and more effective reduction in the total sound scattered.

Aerodynamic configurations with finite chord and span need to be considered to investigate the effects of low- and mid-frequency scattering along poro-elastic trailing edges. Finite edges are susceptible to physical effects such as structural resonance (Leppington, 1976, 1978; Leppington *et. al*, 1986) and leading-edge back-scattering of trailing-edge sound. Furthermore, secondary scattering may occur along lateral edges

and corners as discussed by Cavalieri *et. al* (2014a). Both these topics have been investigated analytically for rigid plates by Roger and Moreau (2005) and Assier and Peake (2012). While the former investigated the effect of backscattering on leading edges using Amiet's theory, the latter employed the Wiener Hopf technique to investigate the noise scattering in a rigid corner of a semi-infinite plate. Other more fundamental concerns include the possibility of secondary scattering of turbulence and elastic waves by the rigid-elastic junctions (Crighton, 1972), which may affect the overall far-field acoustic signature. Regarding the problem of fluid-structure interaction, Crighton (1989) discussed in details the fundamentals of the fluid loading parameters for structures immersed in air or submerged in water. He showed that several parameters are important for the scattering of acoustic waves in elastic structures. In this context, three non-dimensional parameters can be defined based on the fluid and material properties: the non-dimensional wavenumber, or Helmholtz number, which represents a non-dimensional frequency; the bending wave Mach number which represents the Mach number of the propagation of elastic waves, in comparison to the acoustic waves; and the intrinsic fluid loading parameters. The bending wave Mach number also relates the acoustic wavenumbers to the bending wavenumbers and according to Howe (1998), reductions in the noise scattering occur for low subsonic bending wave Mach numbers. The fluid loading factor relates the properties of the fluid and the plate and one should expect significant noise reductions for intense fluid loads, for instance, plates submerged in water.

Porosity effects on noise scattering have also been investigated in the literature. A theoretical analysis was performed by Williams (1972) to analyze the dynamic of the generation and scattering of sound by an infinite rigid plane with a homogeneous layer of perforations. In this work, it was showed that low porosity values leads to a monopole scattered field with the strength dependent only on the aperture geometry. On the other hand, high porosity leads to a weaker dipole radiated field where the strength is independent of the aperture geometry. Leppington and Levine (1973) analysed the reflexion and transmission for a rigid plane screen that contains periodic arrangements of circular or elliptical apertures. An asymptotic solution was obtained for the scattered waves and the relationship among aperture dimension, spacing distribution and acoustic wavelength was investigated. A theoretical model was proposed by Howe (1979b) to study the effects of unsteady motion caused by the fluctuations in the driving pressure of a high Reynolds number mean flow through circular apertures in a thin rigid plate. In this work, the Rayleigh conductivity for a circular aperture was computed. Hughes and Dowling (1990) presented an experimental investigation of a perforated lining which was inserted in the afterburner section of aircraft engines to reduce the level of sound radiated driven by combustion instabilities. Experimental results showed that perforated screens lead

to an efficient sound absorber when compared with similar rigid surfaces, showing good agreement with theoretical predictions. Another interesting aspect presented was that the perforations can be properly designed in order to maximize the sound absorption for a specific range of frequencies.

Howe (1979a) employed the theory of unsteady potential flows through a rigid perforated trailing edge of an airfoil immersed in a uniform mean flow to investigate the problem of the generation of aerodynamic sound by turbulence. It was shown that as the number of perforations increases, the acoustic field generated with and without the perforations differ only in phase. Results showed that the noise scattering was efficiently attenuated for different configurations of perforated trailing edges when compared with rigid ones. Details of the influence of shape perforations and mean flow effects on the Rayleigh conductivity was also studied by Howe *et. al* (1996a); Grace *et. al* (1998a); Howe (1998).

Recently, Cavalieri *et. al* (2016) developed a novel formulation for the study of acoustic scattering by two dimensional poro-elastic plates (plates with finite chord but infinite span). Results showed that both elasticity and porosity of the plate tend to reduce the scattered sound, in agreement with previous work considering semi-infinite plates. Finite elastic plates are shown to reduce the strength of acoustic scattering when excited near a resonant frequency and at high Helmholtz numbers based on the plate chord. At low Helmholtz numbers, finite elastic plates produce only modest reductions in far-field sound relative to the rigid case. On the other hand, porosity seems to be more effective in reducing the radiated sound for lower Helmholtz numbers. The combined beneficial effects of elasticity and porosity are shown to be effective in reducing the scattered sound for a broader range of Helmholtz numbers for 2D poro-elastic plates.

In the present work, we develop a fast numerical framework for the study of acoustic scattering by fully three-dimensional poro-elastic plates. With the present formulation we obtain results directly comparable with experiments. The numerical methodology employs a 3D wideband adaptive fast multipole boundary element method (FMM-BEM) (Wolf and Lele, 2011) which is modified to solve the acoustic problem due to a source in the proximity of a finite poro-elastic edge. The solution of the structural problem for the finite elastic plate is obtained using a modal basis computed by either a pseudo-spectral method or a more general finite element method. The structural and acoustic problems are coupled by adequate boundary conditions relating the plate displacement to the acoustic pressure.

1.1 Motivation and Objectives

The goals of this effort are to extend beyond the analytical work of Jaworski and Peake (2013) and the numerical work of Cavalieri *et. al* (2016) and, hence, to evaluate finite chord and span effects. The aims of these dissertation can be summarized in the followin way:

- To develop a fast numerical framework to investigate the isolated and combined effects of porosity and elasticity in airfoil trailing-edge noise scattering. In order to accomplish this objective, we present a numerical methodology which can handle arbitrary three-dimensional configurations of poro-elastic plates. The current numerical methodology solves the Helmholtz equation for the acoustic scattering and the fluid-structure interaction problem is fully coupled via the boundary conditions of the Helmholtz integral equation. A boundary element method is applied to solve the Helmholtz equation for the acoustic scattering simulation and a fast multipole method is employed to reduce the computational cost of the computations. The methodology requires a preliminary calculation of a structural modal basis which is employed in the acoustic scattering simulation of elastic plates. The structural solutions are obtained either by a collocation spectral method or a finite element method. The porosity effect is solved through a Rayleigh conductivity model which is incorporated to the acoustic formulation.

- To implement and couple several numerical techniques including the boundary element method, BEM, the fast multipole method, FMM, the collocation spectral method, CSM, and the finite element method, FEM. As discussed, the BEM is accelerated by the FMM to solve the acoustic scattering problem. The current wideband FMM formulation allows the study of low- and high-frequency problems through the combination of two FMM methodologies. For low frequencies, we employ a partial wave expansion of the free-field Green's function. On the other hand, for high frequencies, a plane wave expansion of the Green's function is applied. While the latter method is more efficient in terms of computational cost, the former method is stable at all frequencies. With a proper combination of both techniques, a fast and stable method is presented. Moreover, the present implementation employs an adaptive mesh refinement in the FMM which improves the performance of the FMM through the creation of several lists of interactions at the different levels. A complete description of the wideband adaptive FMM is provided along the work. The FEM and the CSM are employed to obtain the solution of the vibration problem of elastic plates and the different methodologies are employed to validate

the modal bases. Along this work, we provide a validation of the methodology for the computation of the structural modal basis for higher order modes which is not found in the literature. Here, the CSM is also extended to solve problems of plates with swept trailing edges and the FEM is a more general methodology that allows the study of arbitrary geometries. In order to employ the methods described here, several tools were developed to couple the structural and acoustic solvers.

- To analyze different fluid-structure interaction configurations consisting of plates with swept trailing edges and trailing-edge serrations considering compact and non-compact sources. These analyses are performed for noise scattering at low and high-frequencies showing the trends in terms of noise reduction both for directivity plots and for integrated far-field sound power level. A parametric study is presented along this work allowing a full assessment of the effects of porosity, elasticity and their combination. Moreover, the effects of sweep on trailing-edge noise reduction are also investigated for different sweep angles and trailing-edge serrations. Problems involving different noise sources are solved using the present fast methodology. We show that the current method allows the study of noise scattering by complex noise sources described from analytical models, high-fidelity numerical simulations and models educed from experiments. Considering the latter case, we employ a turbulent jet wavepacket to investigate the problem of jet-wing noise installation using a poro-elastic plate with a swept trailing edge.

- To analyze the noise scattering of plates with low and high aspect ratios. In the former case, the plate structural configuration considers a clamped leading edge, simulating typical flap configurations. For the latter case, the plate is clamped along one of its lateral edges, simulating helicopter rotor blades or a high aspect ratio aircraft wing. The poro-elastic plates are excited by acoustic source configurations positioned at different locations representing relevant physical mechanisms of noise generation such as turbulent boundary layer noise and tip vortex noise. To study acoustic and vibration effects for excitation by two and three-dimensional acoustic sources representing coherent and weakly correlated vortical structures, such as vortex shedding and turbulent eddies, respectively.

- To investigate the effects of noise reduction by the application of anisotropic composite materials. One of the main achievement of this work is the extension of the proposed numerical framework to be able to analyze both isotropic materials and anisotropic composite materials. Composite materials can offer structural properties similar to those of typical aeronautical metallic materials while having lower weight. The numerical formulation for the structural vibration problem is

modified to handle anisotropic materials with the aim of investigating the effects of noise reduction in elastic trailing edges. We present a study of laminated composite plates with different configurations of stacking sequences. We believe that the current methodology can be employed together with an optimization procedure to design low-weight, low-noise-emission wings for drones and other devices.

- To perform preliminary calculations of poro-elastic plates submerged in water. In this study, we show that even higher noise reductions can be obtained for poro-elastic plates in noise scattering calculations in underwater applications. For these cases, the elastic plates are subjected to intense fluid loading and the applications should consider the reduction of noise signature by submarines and other devices.

1.2 Contributions of the present work

Here, we develop a fast computational framework to handle fully 3D problems of acoustic scattering by poro-elastic plates including the possibility of predicting sound generation by compact and non-compact sources. With the present numerical framework, it is possible to evaluate the effects of scattering by trailing and leading edges, along with lateral edges and corners. Moreover, one can further assess the effects of plate aspect ratio and scattering by 2D and 3D acoustic sources for different ranges of acoustic and plate vibration frequencies along with different poro-elastic characteristics. The numerical framework can be applied for the study of both isotropic metallic materials and anisotropic composite materials.

To solve the structure problem, the modal basis is computed *a priori* and used as an auxiliary solution for the boundary condition of Helmholtz equation. Collocation spectral method, CSM, is implemented in generalized curvilinear coordenates in order to compute the modal basis of a quadrilateral plate. In this work, we focous to study cantilever configurations that is well representative of realistic applications like wings, rotorcrafts, wind turbines and high-lift devices. The verification and validation of the spectral method implemantion is performed using a well-known commercial package ANSYS Mechanical. This software uses the classical finite element method, FEM, to solve structure problem of general geometries. The solution provide by ANSYS consider a dimensional domain whereas the spectral solver is implemented for dimensionless variables. To compare these different solutions the output from ANSYS need to be post processed with a developed script.

Different numerical methods was employed to solve the fluid-structure interaction problem. In this sense, acoustic scattering has a mesh to solve accurately the acoustic

waves, and the bending waves propagating in the structure is computed by another mesh. To obtain the solution of the fully coupled problem, it is required an interpolation of the bending waves into to BEM mesh, and several algorithm was developed to execute this step. Moreover, a convergence analysis was performed for mesh discretization to ensure that acoustic and bending wavelength is solved with accuracy.

To validate the current theoretical formulation and its numerical solution. Here, we present a validation procedure of the current methodology for acoustic predictions of poro-elastic plates. In order to do so, we compare the numerical results obtained by the fully three-dimensional problems to those obtained by a two-dimensional implementation of the current formulation. We show that the solutions of both formulations have a good agreement for plates of high aspect ratio excited by two-dimensional sources.

2 MATHEMATICAL MODEL

2.1 Acoustic Predictions

The model problem at hand is shown schematically in Fig. 2.1. A sound source $\mathcal{S}$, representative of a turbulent eddy in the plate boundary layer, is placed on the vicinity of one of the edges of a finite poro-elastic plate, and we wish to determine the scattered sound at a given observer position r. Figure 2.1(a) illustrates a plate with finite span and finite chord, with one clamped leading edge and free trailing and lateral edges. However, other combinations of structural boundary conditions can also be handled with the numerical formulation described herein.

The main physical processes in the problem are represented in Fig. 2.1(b), which shows a side view of the configuration analyzed. The turbulent eddy in the vicinity of the trailing edge generates an incident quadrupolar sound field. A quadrupole in free field has a near-field pressure that is mostly reactive and does not propagate efficiently to the far acoustic field. However, due to the source proximity to the edge, the said near-field pressure is now scattered by the plate and radiates to the far-field by this mechanism (Crighton, 1975). Depending on the frequency range, the scattered sound radiates as a more efficient dipolar or cardioid sound field, increasing the far-field noise. At the same time, the incident acoustic field excites structural bending waves along the plate which propagate through the surface. These waves hit the clamped leading edge of the plate and are reflected towards the trailing edge if no structural damping is set. The elastic waves also propagate along the span of the plate hitting its lateral edges and corners. Therefore, a secondary acoustic scattering takes place at the leading and lateral edges of the plate due to acoustic diffraction and due to the impingement of the bending waves.

To obtain the scattered sound, we solve the following non-homogeneous Helmholtz equation

$$\nabla^2 \tilde{p} + \tilde{k}_0^2 \tilde{p} = -\tilde{\mathcal{S}}, \tag{2.1}$$

where $\tilde{\mathcal{S}}$ is the acoustic source model and $\tilde{k}_0$ is the acoustic wavenumber given by $\tilde{\omega}/\tilde{c}_0$ for angular frequency $\tilde{\omega}$ and speed of sound $\tilde{c}_0$. The overhead tildes indicate dimensional terms and an $\exp\left(-\mathrm{i}\tilde{\omega}\tilde{t}\right)$ time dependence is assumed throughout. Equation (2.1) is subject to boundary conditions matching velocities of the fluid and vibrating plate at the fluid-solid interface. The solution of the plate vibration is obtained through a modal basis

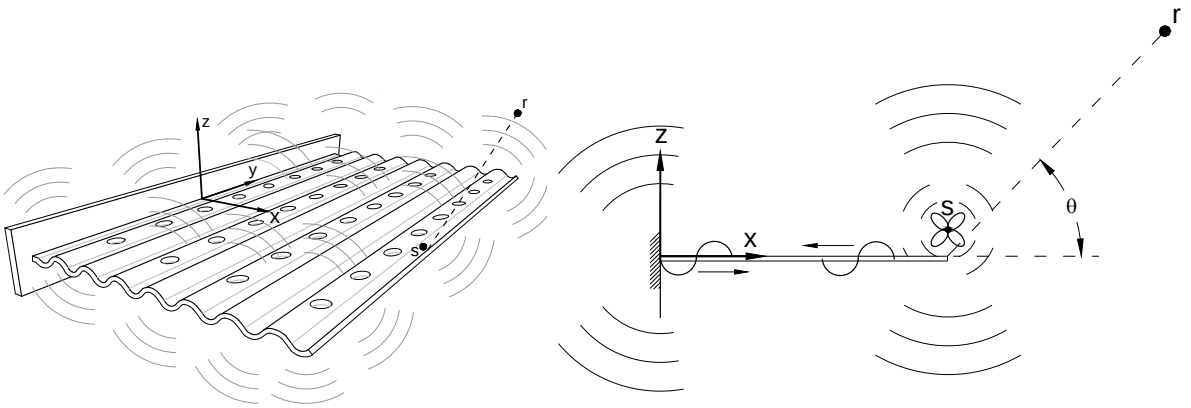

(a) (b)

Figure 2.1: (a) Schematic of a rectangular poro-elastic plate with finite chord and span, where one edge is clamped along the y axis and the other edges are free, subject to acoustic radiation from a source S; (b) Cross section at $y = 0$, illustrating the main physical features of the model problem.

and it is possible to consider any type of plate material. In this work, we provide the detailed formulations for isotropic and anisotropic materials. Here, the external medium is considered quiescent and results are shown for poro-elastic plates immersed in air and submerged in water. The fluid and structural problems are fully coupled in the present methodology. However, the incident source is not modified by the displacement of the plate, which is considered small in the current analysis. External flow convective effects are not investigated in the current formulation as well as dissipative effects occurring in the porous formulation.

2.2 Isotropic Materials

The equation for a harmonic load applied to a thin poro-elastic plate composed of an isotropic material (Jaworski and Peake, 2013; Howe, 1998) is given by

$$(1-\alpha_H)\tilde{B}\nabla^4\tilde{w} - \tilde{m}\tilde{\omega}^2\tilde{w} = \left(1 + \frac{2\alpha_H\tilde{K}_R}{\pi\tilde{R}}\right)\Delta\tilde{p}, \tag{2.2}$$

where $\tilde{w}$ is the plate displacement, $\tilde{B}$ is the effective bending stiffness of the plate (modified by porosity), $\tilde{m}$ is the mass per unit area, and $\Delta\tilde{p}$ is the applied pressure load in the positive $\tilde{z}$ direction, based on Fig. 2.1. The thin-plate model assumes that the bending wavelength is much longer than the plate thickness. The porosity of the plate is characterised by the open area fraction α_H, the Rayleigh conductivity $\tilde{K}_R$ and the pore radius $\tilde{R}$. Note that Eq. (2.2) is valid for $\alpha_H^2 \ll 1$ and $\tilde{k}_0 R \ll 1$ and is the

result of area averaging of the plate and the pores, where the local details of individual pores are neglected in favor of their overall influence (Howe, 1998). $\tilde{B}$ is defined by $\tilde{B} = (1 - 2\alpha_H \nu/(1-\nu))\,\tilde{B}_0$, where $\tilde{B}_0$ is the bending stiffness of a plate without porosity and ν is the Poisson ratio. The previous terms are only valid for a plate composed of an isotropic material. The present formulation will be later extended to handle anisotropic materials.

The Rayleigh conductivity $\tilde{K}_R$ relates $\tilde{w}_a$, the fluid displacement in the pores, to $\Delta\tilde{p}$ by

$$\tilde{w}_a = -\frac{\tilde{K}_R \Delta\tilde{p}}{\pi\tilde{\rho}_f\tilde{\omega}^2\tilde{R}^2}, \tag{2.3}$$

where $\tilde{\rho}_f$ is the fluid density. Finally, the pressure at the plate surface and the plate and fluid displacements are related by the linearised Euler equation as

$$\tilde{\rho}_f\tilde{\omega}^2\left[(1-\alpha_H)\tilde{w} + \alpha_H\tilde{w}_a\right] = \left.\frac{\partial\tilde{p}}{\partial n}\right|_S \tag{2.4}$$

where $\left.\frac{\partial\tilde{p}}{\partial n}\right|_S$ is the derivative of the pressure in the normal direction, computed along the plate surface S.

When the flexural and acoustic waves are strongly coupled, the speed of bending waves is comparable to the speed of sound in the fluid (Howe, 1998) and the fluid pressure loading becomes important. Crighton (1989) presents the fluid loading mechanisms for plates of isotropic materials. In order to determine the important fluid-structural interaction parameters, firstly, we assume a plate immersed in vacuum, i.e., $\Delta p = 0$, to evaluate the free vibration problem. Considering plane waves propagating in an arbitrary direction φ relative to the x axis (chordwise) of the plate, the displacement is given by

$$\tilde{w}(x,y,t) = \hat{w}e^{i(k_x x + k_y y - \omega t)}, \tag{2.5}$$

where the wavenumber components are $k_x = k\cos\varphi$ and $k_y = k\sin\varphi$. The bending wavenumber, k_B, is obtained by solving the characteristic equation as in Doyle (1997), considering only the waves propagating without attenuation at phase speed ω/k_B. Considering the bending stiffness $\tilde{B}$ for an isotropic material, the bending wavenumber is written as,

$$\tilde{k}_B = \left(\frac{\tilde{m}\tilde{\omega}^2}{\tilde{B}}\right)^{1/4}. \tag{2.6}$$

Here, $\tilde{m} = \tilde{\rho}_s\tilde{h}$ is the mass per unit area of the plate and the bending stiffness is defined as $\tilde{B} = \tilde{E}\tilde{h}^3/\left[12(1-\nu^2)\right]$. Here, $\tilde{E}$ is the elasticity modulus, ν is the Poisson ratio, $\tilde{h}$ is the plate thickness and $\tilde{\rho}_s$ is the density of the plate material. The phase speed of the

elastic waves increases with frequency and, when it is equal to the speed of sound for the in vacuum case (Howe, 1993b), we can define the coincidence frequency $\tilde{\omega}_c$ as

$$\tilde{\omega}_c = \left(\tilde{m}\tilde{c}_0^4/\tilde{B}\right)^{1/2}. \tag{2.7}$$

Following Jaworski and Peake (2013) and Crighton and Innes (1984), we proceed to obtain non-dimensional equations of the current fluid-structure interaction problem. The fluid pressure loading is characterized by two important parameters defined by Crighton (1989) as $\alpha = \tilde{\rho}_f\tilde{c}_0/\tilde{m}\tilde{\omega}$ and $\Omega = \tilde{k}_0/\tilde{k}_B$. One should observe that these two parameters are both frequency dependent. In order to define a parameter independent of frequency, the intrinsic fluid loading parameter ϵ is obtained by the choice of the coincidence frequency, which depends solely on properties of the fluid and the plate as shown by Howe (1998)

$$\epsilon = \frac{\tilde{\rho}_f\tilde{c}_0}{\tilde{m}\tilde{\omega}_c} = \frac{\tilde{\rho}_f}{\tilde{\rho}_s}\left(\frac{E}{12\tilde{\rho}_s\tilde{c}_0^2(1-\nu^2)}\right)^{1/2}. \tag{2.8}$$

Therefore, the only parameter which depends on the frequency is the vacuum bending wave Mach number, Ω, that represents the ratio between the phase speed of the structural waves on the plate (placed in vacuum) and the speed of sound in the medium

$$\Omega = \frac{\tilde{c}_p(k_B)}{\tilde{c}_0} = \frac{\tilde{k}_0}{\tilde{k}_B} = \sqrt{\frac{\tilde{\omega}}{\tilde{\omega}_c}}. \tag{2.9}$$

From the literature (Jaworski and Peake, 2013; Howe, 1998), one should expect reductions in the noise scattering mechanism for bending waves with phase speeds lower than the speed of sound, *i.e.*, for subsonic bending wave Mach numbers. Moreover, one should mention that, in the present structural model, only flexural waves are considered via the bending-wave equation (2.2).

The non-dimensional Rayleigh conductivity, $K_R = 2\tilde{K}_R/(\pi\tilde{R})$, is obtained for circular apertures where $\tilde{K}_R = 2\tilde{R}$, and thus $K_R = 4/\pi$. Extensions of the Rayleigh conductivity concept to non-circular orifices and external flow effects may be considered by the methods described by Howe *et. al* (1996b); Grace *et. al* (1998b) but are not pursued here.

After identifying the following dimensionless variables,

$$w = \frac{\tilde{w}}{\tilde{L}}, \tag{2.10}$$

$$R = \frac{\tilde{R}}{\tilde{L}}, \tag{2.11}$$

$$k_0 = \tilde{k}_0 \tilde{L}, \tag{2.12}$$

$$p = \frac{\tilde{p}}{\tilde{\rho}_f \tilde{c}_0^2}, \tag{2.13}$$

$$\mathcal{S} = \frac{\tilde{\mathcal{S}}}{\tilde{\rho}_f \tilde{c}_0^2 \tilde{L}^2}, \tag{2.14}$$

$$(x, y, z) = \frac{1}{\tilde{L}}(\tilde{x}, \tilde{y}, \tilde{z}), \tag{2.15}$$

where $\tilde{L}$ is the reference chord length of the finite poro-elastic plate, we arrive at the non-dimensional versions of Eqs. (2.1)-(2.4):

$$\nabla^2 p + k_0^2 p = -\mathcal{S}, \tag{2.16}$$

$$(1 - \alpha_H)\nabla^4 w - \frac{k_0^4}{\Omega^4} w = (1 + \alpha_H K_R)\frac{\epsilon}{\Omega^6} k_0^3 \Delta p, \tag{2.17}$$

$$(1 - \alpha_H) k_0^2 w - \frac{\alpha_H K_R}{2R} \Delta p = \left.\frac{\partial p}{\partial n}\right|_S . \tag{2.18}$$

The system of equations (2.16), (2.17), and (2.18) constitute the acoustic problem (2.16) subject to boundary conditions (2.17) and (2.18) that relate the pressure and its normal derivative on the plate surface. For a given set of plate parameters, the structural-acoustic interaction is governed by three non-dimensional parameters: ϵ, Ω, and k_0. To close the problem, the boundary conditions of the vibration problem (2.17) must be provided.

2.3 Anisotropic Materials

In this section, we extend the previous formulation of the structural problem to be able to solve problems of acoustic scattering by elastic plates of composite anisotropic materials. Hence, it is important to understand how the variations of the material properties can affect the fluid-structure interaction. In order to perform such assessment, the classical laminate plate theory (CLPT) is assumed for an orthotropic material with laminated plates. Here, each lamina can have an arbitrary orientation with respect to the coordinate directions of the plate.

The coupling between acoustic and structural waves is dominated by the transverse

direction and, hence, it is reasonable to neglect the effect of longitudinal waves. The laminates are stacked in a symmetric fashion related to the z-axis so that both the geometry and material properties are assumed mirrored about the mid surface of the plate. In this way, there is no coupling between bending-extension or shear-extension and the only concern here are bending waves. Considering the assumptions above, the general form of the equation for an unsteady pressure load applied to a composite plate is given as (Doyle, 1997)

$$\tilde{D}_{11}\frac{\partial^4\tilde{w}}{\partial x^4} + 4\tilde{D}_{16}\frac{\partial^4\tilde{w}}{\partial x^3\partial y} + 2(\tilde{D}_{12}+2\tilde{D}_{66})\frac{\partial^4\tilde{w}}{\partial x^2\partial y^2} + 4\tilde{D}_{26}\frac{\partial^4\tilde{w}}{\partial x\partial y^3} + \tilde{D}_{22}\frac{\partial^4\tilde{w}}{\partial y^4} - \tilde{\rho}_s\tilde{h}\frac{\partial^4\tilde{w}}{\partial t^2} = \Delta\tilde{p}. \tag{2.19}$$

Here, $\tilde{w}$ is the plate displacement of flexural waves, $\tilde{D}_{ij}$ is the bending stiffness tensor (Jones, 1998) of the plate, and $\Delta\tilde{p}$ is the applied fluid pressure loading. For isotropic materials the bending stiffness tensor reduces to $\tilde{D}_{11} = \tilde{D}_{12} = \tilde{D}_{22} = \tilde{B}$, $\tilde{D}_{16} = \tilde{D}_{26} = \tilde{D}_{66} = 0$.

Similarly to the plate of isotropic material, the pressure at the plate surface and the transverse displacements are related by the linearized Euler equation as

$$\tilde{\rho}_f\tilde{\omega}^2\tilde{w} = \frac{\partial\tilde{p}}{\partial\tilde{z}}. \tag{2.20}$$

In the above equations, tildes indicate dimensional quantities and a periodic time dependence $\exp(-i\tilde{\omega}\tilde{t})$ is, again, implicitly assumed. In the derivations for anisotropic materials, the medium is still considered quiescent.

For composite materials the bending stiffness $\tilde{D}_{11}$ is considered as a reference value following the x axis ($\varphi = 0$). Hence, the bending wavenumber becomes,

$$\tilde{k}_B = \left(\frac{\tilde{m}\tilde{w}^2}{\tilde{D}_{11}}\right)^{1/4}. \tag{2.21}$$

Here, the bending stiffness in the chordwise direction is defined as $\tilde{D}_{11} = \tilde{E}_{11}\tilde{h}^3/\left[12(1-\nu_{12}^2)\right]$ where $\tilde{E}_{11}$ is the elasticity modulus in the principal direction of the material and ν_{12} is the Poisson ratio. For composite materials, we also choose to define the coincidence frequency as a function of the bending stiffness $\tilde{D}_{11}$

$$\tilde{\omega}_c = \left(\frac{\tilde{m}\tilde{c}_0^4}{\tilde{D}_{11}}\right)^{1/2}. \tag{2.22}$$

The intrinsic fluid loading parameter ϵ for composite plates is obtained by the choice of the coincidence frequency represented by Eq. 2.22, which depends solely on properties

of the fluid and the plate as

$$\epsilon = \frac{\tilde{\rho}_f \tilde{c}_0}{\tilde{m}\tilde{\omega}_c} = \frac{\tilde{\rho}_f}{\tilde{\rho}_s}\left(\frac{E_{11}}{12\tilde{\rho}_s\tilde{c}_0^2(1-\nu^2)}\right)^{1/2}. \tag{2.23}$$

and the vacuum bending wave Mach number, Ω, is still computed by

$$\Omega = \frac{\tilde{c}_p(k_B)}{\tilde{c}_0} = \frac{\tilde{k}_0}{\tilde{k}_B} = \sqrt{\frac{\tilde{\omega}}{\tilde{\omega}_c}}. \tag{2.24}$$

Here, the structural parameters are normalized by the bending stiffness tensor in the chordwise direction $D_{ij} = \tilde{D}_{ij}/\tilde{D}_{11}$. Thus, the non-dimensional equations obtained using the dimensionless variables defined above can be finally written as

$$\mathcal{L}(w) - \frac{k_0^4}{\Omega^4} w = \frac{\epsilon}{\Omega^6} k_0^3 \Delta p, \tag{2.25}$$

and

$$k_0^2 w = \frac{\partial p}{\partial z}, \tag{2.26}$$

where $\mathcal{L}$ is the linear operator related to the fourth-order spatial derivatives in Eq. (2.19), written as

$$\mathcal{L}(w) = \frac{\partial^4 w}{\partial x^4} + 4D_{16}\frac{\partial^4 w}{\partial x^3 \partial y} + 2(D_{12}+2D_{66})\frac{\partial^4 w}{\partial x^2 \partial y^2} + 4D_{26}\frac{\partial^4 w}{\partial x \partial y^3} + D_{22}\frac{\partial^4 w}{\partial y^4}. \tag{2.27}$$

The system of equations (2.16), (2.25), and (2.26) can be seen as the acoustic scattering problem, where (2.16) is subject to boundary conditions (2.25) and (2.26) that relate the pressure and its normal derivative on the composite plate surface. To close the problem, the boundary conditions of the vibration problem given by Eq. (2.25) must be provided. In the present work, the boundary conditions are zero displacement and rotation for clamped edges and zero applied forces and moments for free edges.

2.4 Classical Theory of Plates

The classical theory of plates or Kirchhoff-Love plate model is the fundamental formulation used in this work for the propagation of the bending waves in thin plates using the collocation spectral method (CSM). Therefore, for completeness, some details of this theory are provided in this section. The displacement field for this theory is based in the Kirchhoff hypothesis which consists in the following three assumptions (Reddy, 2006):

(i) Straight lines perpendicular to the mid-surface before deformation remain straight after deformation;

(ii) The transverse normals do not experience elongation;

(iii) The transverse normals rotate such that they remain perpendicular to the mid-surface after deformation.

In order to obtain the dynamic equilibrium equations for a thin flat plate using the classical plate theory, we start from the displacement field to compute the strain tensor and then apply the constitutive equations for linear elastic isotropic solids to obtain the stress tensor. Subsequently, the strain energy can be obtained from strains and stresses and, with the strain energy, the kinetic energy, and the virtual work of the external forces, we can obtain the equations of motion using Hamilton's principle (Dym and Shames, 2013).

In other words, in the Kirchhoff hypothesis the displacement is constant throughout the thickness of the plate, since there is no shear deformation and considering that the effects of rotational inertia are negligible. We will consider a plate of uniform thickness $\tilde{h}$ and the rectangular Cartesian coordinates $(\tilde{x}, \tilde{y}, \tilde{z})$ with the xy-plane at the geometric middle plane of the plate. The total domain of the plate is the tensor product $S \times (-\tilde{h}/2, \tilde{h}/2)$, where S is the surface of the plate mid-plane. The boundary is represented by ∂S with outward normal $\vec{n}$ and the displacement field under these assumptions can be written as

$$\begin{aligned} \tilde{u}(\tilde{x}, \tilde{y}, \tilde{z}, \tilde{t}) &= \tilde{u}_0(\tilde{x}, \tilde{y}, \tilde{t}) - \tilde{z}\frac{\partial \tilde{w}_0}{\partial \tilde{x}} \ , \\ \tilde{v}(\tilde{x}, \tilde{y}, \tilde{z}, \tilde{t}) &= \tilde{v}_0(\tilde{x}, \tilde{y}, \tilde{t}) - \tilde{z}\frac{\partial \tilde{w}_0}{\partial \tilde{y}} \ , \text{ and} \\ \tilde{w}(\tilde{x}, \tilde{y}, \tilde{z}, \tilde{t}) &= \tilde{w}_0(\tilde{x}, \tilde{y}, \tilde{t}) \ , \end{aligned} \tag{2.28}$$

where the terms with subscript 0 refer to the stretching actions of the mid-surface.

From the kinematic assumptions, the strain-displacement equations are written as

$$\begin{aligned} \epsilon_{xx} = \ -\tilde{z}\frac{\partial \tilde{w}^2}{\partial \tilde{x}^2} \quad , \quad \epsilon_{yy} = -\tilde{z}\frac{\partial \tilde{w}^2}{\partial \tilde{y}^2} \quad , \quad \epsilon_{zz} = 0 \ , \\ \epsilon_{xy} = \ -\tilde{z}\frac{\partial \tilde{w}^2}{\partial \tilde{x}\partial \tilde{y}} \quad , \quad \epsilon_{xz} = 0 \quad , \quad \epsilon_{yz} = 0 \ . \end{aligned} \tag{2.29}$$

Using the generalized Hook's law to relate the stress and strain tensors, the constitutive equations for the plane stress state in terms of the engineering elastic constants (E, ν, G)

are

$$\begin{aligned}\sigma_{xx} &= \frac{\tilde{E}}{1-\nu^2}\left(\epsilon_{xx}+\nu\epsilon_{yy}\right) \ , \\ \sigma_{yy} &= \frac{\tilde{E}}{1-\nu^2}\left(\epsilon_{yy}+\nu\epsilon_{xx}\right) \ , \text{ and} \\ \sigma_{xy} &= 2\tilde{G}\epsilon_{xy} = \frac{\tilde{E}}{1+\nu}\epsilon_{xy} \ ,\end{aligned} \tag{2.30}$$

and substituting Eq. (2.29) into Eq. (2.30), we have

$$\begin{aligned}\sigma_{xx} &= -\frac{\tilde{E}\tilde{z}}{1-\nu^2}\left(\frac{\partial\tilde{w}^2}{\partial\tilde{x}^2}+\nu\frac{\partial\tilde{w}^2}{\partial\tilde{y}^2}\right) \ , \\ \sigma_{yy} &= -\frac{\tilde{E}\tilde{z}}{1-\nu^2}\left(\frac{\partial\tilde{w}^2}{\partial\tilde{y}^2}+\nu\frac{\partial\tilde{w}^2}{\partial\tilde{x}^2}\right) \ , \\ \sigma_{xy} &= -2\tilde{G}\tilde{z}\frac{\partial\tilde{w}^2}{\partial\tilde{x}\partial\tilde{y}} \ .\end{aligned} \tag{2.31}$$

One should mention that we assume the stress component σ_{zz} to be negligible.

Finally, the equations of motion are derived using the principle of virtual displacement where, for a linear elastic behavior, the strain energy U of the plate is presented by Dym and Shames (2013) as follows

$$U = \frac{1}{2}\int_S\int_{-\tilde{h}/2}^{\tilde{h}/2}\sigma_{ij}\epsilon_{ij}dzdxdy. \tag{2.32}$$

Neglecting the rotational inertia, the kinetic energy may be expressed as

$$K = \frac{1}{2}\int_S\int_{-\tilde{h}/2}^{\tilde{h}/2}\tilde{m}\dot{\tilde{w}}^2dzdxdy, \tag{2.33}$$

and the work of the external forces is written as

$$W = -\int_S\tilde{q}\tilde{w}dxdy - \int_{\partial S}\int_{-\tilde{h}/2}^{\tilde{h}/2}\left[\sigma_{xx}\frac{\partial\tilde{w}}{\partial\tilde{x}}+\sigma_{yy}\frac{\partial\tilde{w}}{\partial\tilde{y}}+\sigma_{xy}\tilde{w}\right]dzds, \tag{2.34}$$

where $\tilde{q}(\tilde{x},\tilde{y})$ represents the distributed external shear forces.

Using Hamilton's principle expressed as

$$\delta\int_{t_1}^{t_2}\left(K-U+W\right)dt = 0, \tag{2.35}$$

and the virtual kinetic energy, the virtual strain energy and the virtual work of the external forces can be derived by applying the inexact operator δ. The Hamilton equation can thus

be written as

$$\int_{t_1}^{t_2}\Bigg[\int_S\left(\tilde{B}_0\nabla^4\tilde{w}+\tilde{m}\tilde{h}\ddot{\tilde{w}}^2-\tilde{q}\right)\delta\tilde{w}dxdy-\int_{\partial S}M_{xx}\frac{\partial\delta\tilde{w}}{\partial\tilde{x}}dy+\int_{\partial S}M_{yy}\frac{\partial\delta\tilde{w}}{\partial\tilde{y}}dx$$
$$-\int_{\partial S}M_{xy}\frac{\partial\delta\tilde{w}}{\partial\tilde{y}}dy+\int_{\partial S}M_{xy}\frac{\partial\delta\tilde{w}}{\partial\tilde{x}}dx-\int_{\partial S}Q_y\delta\tilde{w}dx+\int_{\partial S}Q_x\delta\tilde{w}dy\Bigg]dt=0, \quad (2.36)$$

where $\tilde{B}_0$ is the constant called the bending rigidity written as $\tilde{B}_0=\tilde{E}\tilde{h}^3/12(1-\nu^2)$, and Q_x and Q_y are called the Kirchhoff shear forces or effective shear forces, which can be written as functions of the bending moments M_{xx}, M_{xy} and M_{yy} as

$$Q_x=\frac{\partial M_{xx}}{\partial\tilde{x}}+\frac{\partial M_{xy}}{\partial\tilde{y}},$$
$$\text{and} \quad (2.37)$$
$$Q_y=\frac{\partial M_{xy}}{\partial\tilde{x}}+\frac{\partial M_{yy}}{\partial\tilde{y}}.$$

The equation of motion in its final form is presented by Eq. (2.36) and, applying the equilibrium conditions, it is possible to obtain the strong and weak forms of this equation and the boundary conditions for the individual edges of the plate. In the present work, we will present two numerical methodologies that solve this equation in both strong and weak forms.

2.4.1 Solution of the problem using a structural modal basis

The classical Kirchhoff-Love plate theory is applied to model the structural problem. We consider here the three-dimensional acoustic scattering for plates with finite chord and span. In this case, we rewrite Eq. (2.17) as

$$(1-\alpha_H)\mathcal{L}(w)-\frac{k_0^4}{\Omega^4}w=(1+\alpha_H K_R)\frac{\epsilon}{\Omega^6}k_0^3\Delta p, \quad (2.38)$$

where $\mathcal{L}=\nabla^4$ is the bi-harmonic operator for plates of isotropic materials, or the linear operator that relates the fourth-order spatial derivatives in Eq. (2.27), for plates composed of anisotropic materials. Such operator is subject to the appropriate boundary conditions. In this work, we employed clamped and free edges as will be described. Let us consider now the eigenvalue problem $\mathcal{L}(w)=\beta^4 w$ whose solutions form a complete orthonormal basis ϕ_i for functions satisfying the boundary conditions of the problem (Rayleigh, 1945;

Gatti and Ferrari, 2002), such that

$$\mathcal{L}(\phi_i) = \beta_i^4 \phi_i, \quad \text{where} \quad \langle \phi_i, \phi_j \rangle = \delta_{ij}. \tag{2.39}$$

In what follows we shall call ϕ_i the *modal basis*. The eigenvalues of this problem are real and positive, and the convention β^4 is thus justified allowing the identification of β_i as the bending wavenumber of a vibration mode ϕ_i of the plate. This modal basis comprises the *in vacuo*, free-vibration modes of the plate. We will use these modes as an auxiliary basis to solve the fluid-loaded plate problem, where the plate is saturated with fluid and the pressure is coupled to the plate and fluid displacements. For cases with light fluid loading ($\epsilon \ll 1$), the free-vibration modes are expected to be close to those for fluid-loaded plates, and the convergence of the plate displacement in terms of free-vibration modes is expected to be rapid.

Since the modal basis is a complete orthonormal set for functions satisfying the boundary conditions of the problem, we can write

$$w = \sum_i a_i \phi_i \tag{2.40}$$

for any solution w of the problem composed of (2.38) and the associated boundary conditions. The coefficients a_i are determined by substituting (2.40) into (2.38), using (2.39), and then taking the inner product with ϕ_j. Thus, the displacement (2.40) is

$$w = \frac{1 + \alpha_H K_R}{1 - \alpha_H} \frac{\epsilon k_0^3}{\Omega^6} \sum_j \left[\frac{\langle \Delta p, \phi_j \rangle}{\beta_j^4 - \frac{k_0^4}{(1-\alpha_H)\Omega^4}} \phi_j \right], \tag{2.41}$$

and the derivative of the pressure in the transverse direction evaluated at the plate surface (2.18) is

$$\left. \frac{\partial p}{\partial n} \right|_S = (1 + \alpha_H K_R) \frac{\epsilon k_0^5}{\Omega^6} \sum_j \left[\frac{\langle \Delta p, \phi_j \rangle}{\beta_j^4 - \frac{k_0^4}{(1-\alpha_H)\Omega^4}} \phi_j \right] - \frac{\alpha_H K_R}{2R} \Delta p, \tag{2.42}$$

where the term $\langle \Delta p, \phi_j \rangle$ is the inner product $\int_S \Delta p(x,y) \phi_j(x,y) dx dy$.

Equation (2.42) relates the pressure difference between the two sides of the plate Δp with the transverse pressure gradient evaluated at the plate surface $\partial p / \partial n|_S$ by the solution of the vibration problem. The acoustic problem, formulated with a boundary element method, is based on an integral equation where p and $\partial p / \partial n$ are to be solved for; thus, (2.42) couples these two quantities through the vibration of the plate. The particular case of an impermeable elastic plate can be obtained by setting $\alpha_H = 0$ in (2.42); similarly, results for a porous rigid plate can be obtained by setting $\epsilon = 0$ in

(2.42). A poro-elastic plate has both $\epsilon \neq 0$ and $\alpha_H \neq 0$ and requires the use of the full form of Eq. (2.42).

The modal expansion is written using M modes and we observe in (2.42) that the important modes will be those for which $\beta_j \approx k_B$, which will happen when the plate is excited near a resonance frequency. We expect only limited contributions of modes that are far from satisfying either condition and, thus, the truncation of the expansion is chosen such that β_M, the eigenvalue of the last mode in the expansion, is significantly higher than the bending wavenumber k_B.

3 NUMERICAL METHODS

3.1 Boundary Element Method

In the present work, we solve the problem of acoustic scattering along a finite poro-elastic plate. The sound waves are produced by acoustic sources positioned near the plate trailing edge. The present methodology can handle arbitrary compact and non-compact sources obtained from experiments, simulations or analytical models. The following non-homogeneous Helmholtz equation represents the pressure disturbances induced by acoustic sources in a quiescent medium,

$$\nabla^2 p(\vec{x}) + k_0^2 p(\vec{x}) = -\mathcal{S}_i. \tag{3.1}$$

In Eq. (3.1), $\mathcal{S}_i$ represents the i^{th} source strength, and all terms are written as non-dimensional quantities following the procedure previously discussed. A fundamental solution for the Helmholtz equation is the free space Green function, $G(\vec{x}, \vec{y})$, written as

$$G(\vec{x}, \vec{y}) = \frac{e^{ik_0|\vec{x}-\vec{y}|}}{4\pi|\vec{x}-\vec{y}|}, \tag{3.2}$$

for a 3D formulation. Applying Green's second identity to the Helmholtz equation it is possible to write the following boundary integral equation

$$p(\vec{x}) = \int_S \left[\frac{\partial p(\vec{y})}{\partial n_y} G(\vec{x}, \vec{y}) - \frac{\partial G(\vec{x}, \vec{y})}{\partial n_y} p(\vec{y}) \right] dS - \mathcal{S}(\vec{z}_i), \tag{3.3}$$

where the derivatives with respect to the inward normal direction of the boundary surface are represented by $\partial(.)/\partial n_y$ and $\vec{n}_y$ is an inward unit normal computed at position $\vec{y}$. The i^{th} source location is $\vec{z}_i$. The sound sources considered in this report are acoustic point-quadrupoles, representative of uncorrelated turbulent eddies in a boundary layer, 2D quadrupoles, representative of coherent turbulent structures, and a turbulent jet wavepacket, representative of a non-compact source (Cavalieri *et. al*, 2012). The present turbulent jet source has been successfully applied for the study of the interaction between a jet and a rigid plate in Cavalieri *et. al* (2014a); Piantanida *et. al* (2016).

The boundary conditions specified on the surface of the plate are calculated using the derivative of the pressure in the transverse direction, obtained by the solution of the

vibration problem using a modal basis, given as (Cavalieri *et. al*, 2014b):

$$\partial p/\partial n|_S = n_i \partial p/\partial y_i = n_3(1+\alpha_H K_R)\frac{\epsilon k_0^5}{\Omega^6}\sum_{j=1}^{M}\frac{\langle \Delta p(x), \phi_j\rangle}{\beta_j^4 - \frac{k_0^4}{(1-\alpha_H)\Omega^4}}\phi_j - n_3\frac{\alpha_H K_R}{2R}\Delta p. \quad (3.4)$$

In the equation above, n_3 is the y_3 component of the unit normal vector along the z Cartesian axis. One should note that the Sommerfeld radiation condition, which admits only solutions with outgoing waves, is naturally satisfied for the BEM formulation.

The use of boundary integral equations, such as the BEM, for solving scattering and radiation problems provides several advantages over finite element and finite difference methods. Among these, one can cite the advantage of requiring only the boundary discretization and the accurate modeling of infinite domains. Furthermore, the BEM formulation has non-dispersive and non-dissipative numerical properties. Despite all the advantages of the BEM, the solution of the generally non-symmetric dense matrices appearing in a 3D BEM formulation makes the method prohibitive to use for large-scale problems. In the present work, the boundary discretizations need to accurately resolve both the acoustic and elastic waves in the plate. Therefore, several boundary elements are required to discretize the plate surface. In order to overcome this drawback of the 3D formulation, we apply a fast multipole method (FMM) to accelerate the solution of the BEM linear systems. The FMM is an attractive algorithm that leads to major improvements in simulation time and memory storage of the BEM. In the present work, a wideband adaptive multi-level FMM, stable and efficient at all frequencies, is used for the solution of the acoustic scattering along a finite poro-elastic plate.

3.2 Fast Multipole Method

The fast multipole method is listed as one of the top 10 algorithms of the twentieth century (Cipra, 2000). It was developed by Greengard and Rokhlin (1987) for the solution of $N-$body problems. The application of the FMM for simulations of acoustic scattering was introduced by Rokhlin (1990) for the solution of 2D integral equations. Since then, the FMM has been used to accelerate the solution of electromagnetic and acoustic scattering simulations in several studies, and different formulations have been developed based on the range of frequencies analyzed.

Epton and Dembart (1995) presented the mathematical theory of the partial wave expansion and plane wave expansion formulations for the three-dimensional Helmholtz equation. Song *et. al* (1997) applied the multi-level FMM for 3D electromagnetic scattering problems and discussed the effects of preconditioning and the treatment of

singular integrals. Dembart and Yip (1998) discussed the errors associated with the truncation of multipole expansions. Gyure and Stalzer (1998) presented formulation details for the implementation of the multi-level FMM for the solution of the Helmholtz equation. They also presented a discussion on interpolation and filtering computations required by the multi-level method. Koc and Chew (1998) compared the multi-level FMM with the FMM-FFT method for simulations of acoustic scattering and they found that the multi-level FMM outperformed the FMM-FFT method.

Darve (2000b) presented details for the numerical implementation of the plane wave expansion formulation including techniques for the acceleration of the method and memory usage optimization. Darve also presented a rigorous error analysis and the asymptotic complexity of the FMM for the plane wave expansion formulation (Darve, 2000a). Ohnuki and Chew (2001) performed a study on the error controllability of the multi-level FMM and Yoshida (2001) presented a detailed description of the partial wave expansion formulation for the multi-level FMM. Sakuma and Yasuda (2002); Yasuda and Sakuma (2003) applied the FMM to accelerate BEM calculations of acoustic scattering on an acoustic tube. They also studied the effects of numerical parameters in the plane wave expansion formulation. Gumerov and Duraiswami (2004) derived recurrence relations for the computation of multipole translation and rotation coefficients for the partial wave expansion formulation. Cheng *et. al* (2006), Gumerov and Duraiswami (2009) and Wolf and Lele (2011) presented wideband fast multipole methods applying mixed formulations at different frequency ranges for the solution of the 3D Helmholtz equation.

In this work, we employ the adaptive multi-level FMM from Carrier *et. al* (1988). It consists of clustering boundary elements at different spatial lengths and using multipole expansions to evaluate the interactions among clusters that are well separated from each other. We define two well-separated clusters as sets of elements that are circumscribed by spheres and whose centroids are distant from each other by a length of at least four times their radius. One can improve accuracy in the FMM calculations by increasing this parameter. However, this will reduce the performance of the method because more direct BEM computations will be performed. The nearby elements are computed by the direct solution of the boundary integral equations as in any typical BEM formulation. In the FMM-BEM, the surface boundary is discretized into elements and the entire boundary object is surrounded by a cubical box. Then, a recursive algorithm for the refinement of this box is applied in order to form different expansion levels of the multi-level FMM.

When the FMM algorithm starts, the entire computational box is at level 0 and surrounds the scattering body of interest, which is discretized by boundary elements. The general idea consists of refining the computational box into eight smaller boxes that will be at level 1 and inspecting the number of elements contained in each of the new

boxes. This process continues until the number of boundary elements inside all the boxes is smaller than or equal to a certain prescribed number. In Fig. 3.1, one can observe a computational box surrounding an airfoil with all the smaller boxes showing the adaptive refinement in regions where the number of boundary elements exceeds the maximum allowed per box. This prescribed number of elements per box will define the maximum stage in the refinement level of the FMM. Boxes of level $l+1$ are children of the parent boxes of level l. Each parent box is divided into eight children and these are direct neighbors among themselves, which means that they share a common node, edge or surface. Following the algorithm, one can write an oct-tree structure containing all the children from all boxes at all levels. At every level of refinement, a table of nonempty boxes is maintained, so that once an empty box is encountered, its existence is forgotten and it is not used in the subsequent process.

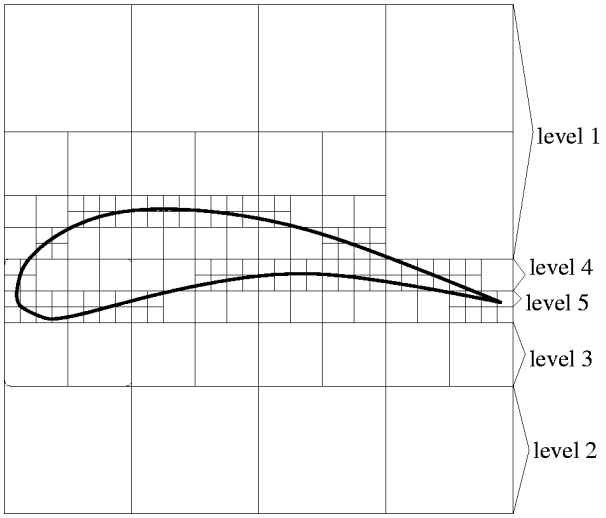

Figure 3.1: Different box levels of the adaptive refinement.

In order to implement the FMM we define a set of lists containing some specific boxes, such as direct neighbors, parent neighbors and others. These lists will help with the computation of multipole expansions and translations and with the acceleration of the FMM. List L_1 of a box b consists of box b itself and all boxes which do not contain children boxes and which share a node, edge or surface with b. If b is a parent box then $L_1 = \emptyset$. List L_2 of a box b is the iterative list from the original FMM (Greengard and Rokhlin, 1987) and it consists of all children of b's parent neighbors that are well separated from b. Boxes on list $L_2(b)$ are in the same level of refinement as b. List L_3 is empty if b is a parent box, and it consists of all children of b's neighbors, at any level, which do not share borders with b. Finally, list L_4 of box b is formed by all boxes c such that $b \in L_3(c)$. One can observe that all boxes in $L_3(b)$ are at higher levels than b, *i.e.*, are smaller than b, and all boxes in $L_4(b)$ are at lower levels than b, *i.e.*, are larger than b. Beyond that, all boxes in $L_4(b)$ do not have children. In Fig. 3.2, one can observe the lists associated with a box b.

In this figure, all the boxes are marked with numbers corresponding to the respective lists which they are associated with. The boxes marked with number 5 are those that are well separated from b's parent, which means that they are in $L_2(b's\,parent)$ or $L_4(b's\,parent)$. We suggest the papers from Carrier *et. al* (1988) and Nishimura (2002) for a more detailed explanation on the FMM implementation including the adaptive refinement procedure and the several steps described in the following paragraphs.

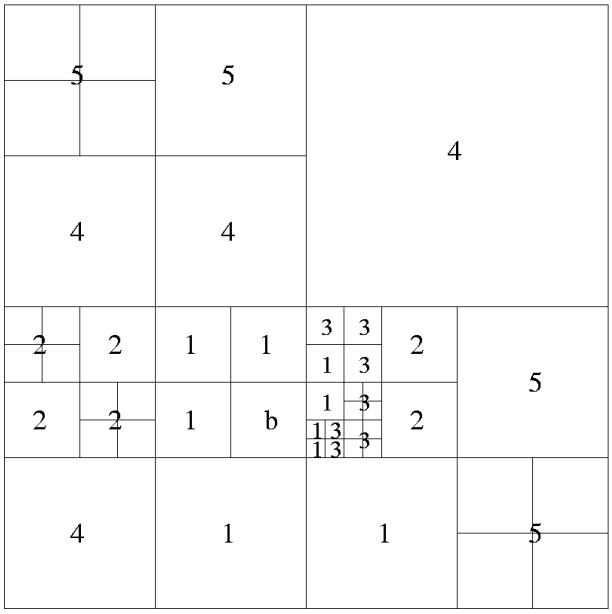

Figure 3.2: Associated lists of box b.

The FMM is often applied to integral or summation equations that contain degenerate kernels. The Green's function, $G(\vec{x},\vec{y})$, is the degenerate kernel one wants to expand in a suitable form in order to apply the FMM. Instead of computing the influence of all source elements at $\vec{y}$ to all field elements at $\vec{x}$ directly, one can write the Green's function as

$$G(\vec{x},\vec{y}) = \sum_i k_i^{(1)}(\vec{x}-\vec{z})k_i^{(2)}(\vec{y}-\vec{z}), \tag{3.5}$$

and, then, compute multipole approximations of clusters of boundary elements representing the acoustic field generated by the sources inside the clusters on far away observer locations. Thus, the first step in the FMM algorithm consists of computing multipole expansions around the centroids of all childless boxes, represented by $\vec{z}$ in Eq. 3.5. These multipole expansions hold for distances $|\vec{x}-\vec{z}|$ larger than $|\vec{y}-\vec{z}|$ and one can write them as

$$M_i(\vec{z}) = \int_{S_0}\left[\frac{\partial p(\vec{y})}{\partial n_y}k_i^{(2)}(\vec{y}-\vec{z}) - \frac{\partial k_i^{(2)}(\vec{y}-\vec{z})}{\partial n_y}p(\vec{y})\right]dS, \tag{3.6}$$

where S_0 is a set of discrete elements inside the box with centroid $\vec{z}$. Each element inside

the box is represented in a multipole expansion and all the multipoles are summed to form a total multipole representation of the sources inside the box. This step is represented as “STEP 1" in Fig. 3.3.

Subsequently, all the multipole expansions from the childless boxes at all levels are shifted to the centroids of their parent boxes up to level 2 of adaptive refinement. Thus, we have multipole expansions for the boxes in level 2 representing their influence on the field outside each one of these boxes. The translation of multipoles from centroids of boxes of level $l+1$ to their parents centroids at level l is commonly called multipole-to-multipole (M2M) translation or upward pass, and it can be seen in “STEP 2" of Fig. 3.3. In the next step, represented in Fig. 3.3 as “STEP 3", the multipole expansions for the boxes in $L_2(b)$ are converted to local expansions about b's centroid and added up forming a local expansion around b's centroid representing the field of the elements from the well separated boxes at the same level of b. These conversions from multipole expansions to local representations around centroids of well-separated boxes are called multipole-to-local (M2L) expansions in the literature. All the local representations from L_2 are then shifted to b's children until the highest refinement level is reached. One can observe these calculations in “STEP 4" of Fig. 3.3. This step is referred in the literature as local-to-local (L2L) translation or downward pass.

Finally, all the calculations can be performed in order to represent the influence of far-field sources to each of the boundary elements. In Fig. 3.3, one can observe this type of calculation in “STEP 5", where the local coefficients computed for the centroids of the boxes in the highest level of refinement are used to compute the effects of far-field sources to each of the elements contained inside box b. Once the influence of the far elements is considered, a further step includes the evaluation of the influence of nearby elements. The interactions from elements on $L_1(b)$ are calculated using direct BEM formulations. For interactions among elements on $L_3(b)$ and $L_4(b)$, we can either use direct BEM calculations if the maximum number of elements inside the boxes is small or compute multipole expansions for the elements inside these boxes and, then, compute the effects of these multipoles to each of the elements inside b. These near-field calculations can be observed in “STEP 6" of Fig. 3.3.

3.2.1 Fast Multipole Method Formulations for the 3D Helmholtz Equation

Here, we describe the FMM formulations employed for the solution of the 3D Helmholtz equation. These include the partial wave expansion method appearing in Yoshida (2001), the rotation-coaxial translation method appearing in Wolf and Lele (2011)

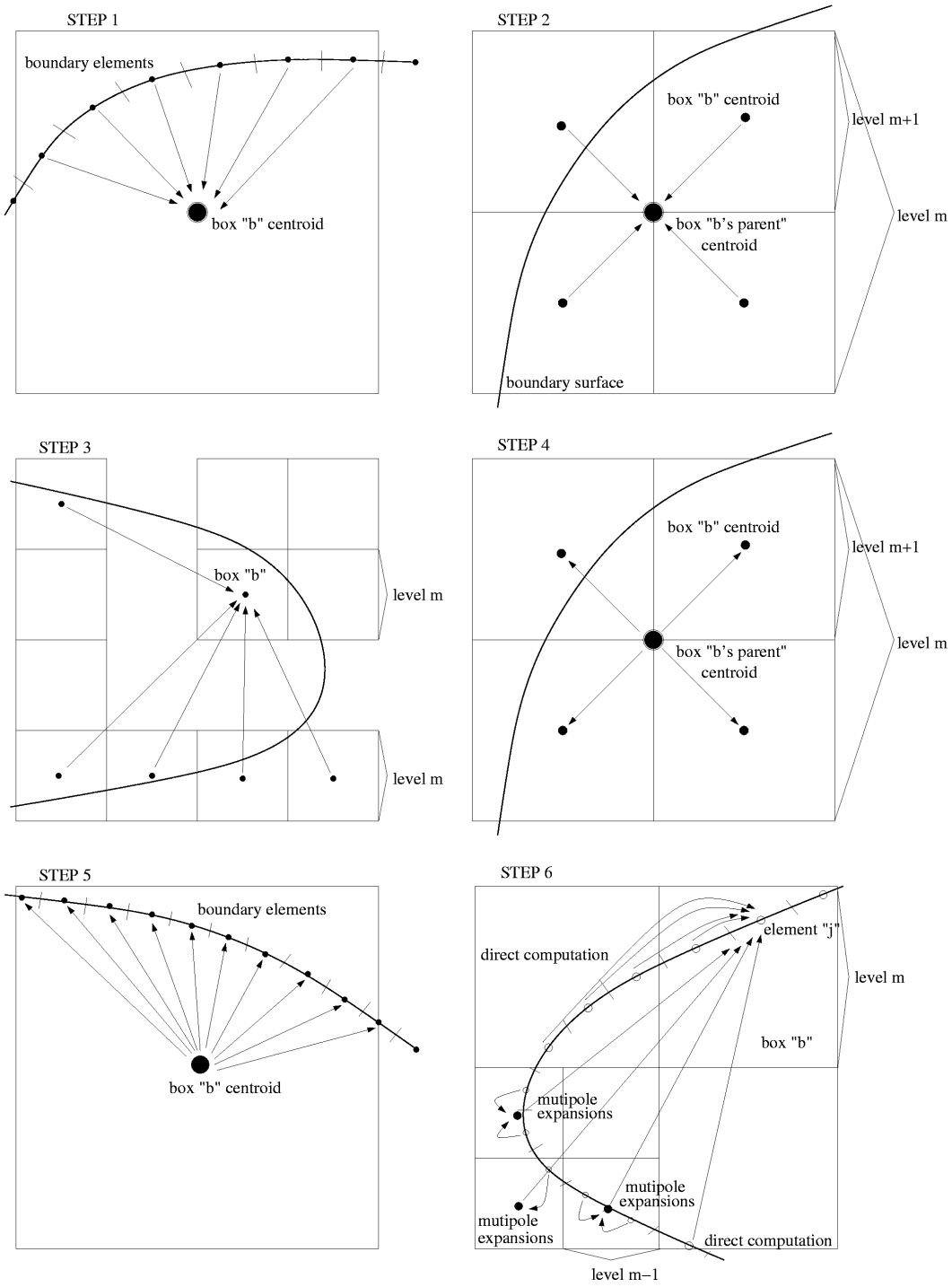

Figure 3.3: Schematic diagram for the several steps in the FMM.

and the plane wave expansion method appearing in Darve (2000b). The rotation-coaxial translation method employs the same series expansions as the partial wave expansion but it reduces the overall computational cost of the algorithm through the application of appropriate rotations of the spherical harmonics. This formulation is still more expensive than the plane wave expansion. However, it will be discussed that the latter is unstable for low-frequency scattering problems and/or for higher levels of refinement in the FMM.

More details about the necessity to use different FMM formulations will be given in the following sections.

3.2.2 Partial Wave Expansion Method

In the partial wave expansion method the free space Green's function is written as

$$G(\vec{x},\vec{y}) = \frac{ik}{4\pi}\sum_{n=0}^{\infty}(2n+1)\sum_{m=-n}^{n} O_n^m(\overrightarrow{o\vec{x}})\overline{I_n^m}(\overrightarrow{o\vec{y}}), \tag{3.7}$$

where the function O_n^m is defined as

$$O_n^m(\vec{X}) = h_n^{(1)}(kr)Y_n^m(\theta,\phi) \tag{3.8}$$

and $\overline{I_n^m}$ is the complex conjugate of I_n^m, defined as

$$I_n^m(\vec{X}) = j_n(kr)Y_n^m(\theta,\phi). \tag{3.9}$$

In the expressions above, j_n represents the $n-th$ order spherical Bessel function of the first kind, $h_n^{(1)}$ is the $n-th$ order spherical Hankel function of the first kind and Y_n^m are the spherical harmonics defined as

$$Y_n^m(\theta,\phi) = \sqrt{\frac{(n-m)!}{(n+m)!}}P_n^m(cos\,\theta)e^{im\phi}, \tag{3.10}$$

where P_n^m stand for the associated Legendre functions. The terms r,θ,ϕ represent the spherical coordinates of some vector $\vec{X}$, which can be $\overrightarrow{o\vec{x}}$ or $\overrightarrow{o\vec{y}}$, for instance. The vectors $\overrightarrow{o\vec{x}}$ and $\overrightarrow{o\vec{y}}$ point from some box center, $\vec{o}$, to a far-field source location, $\vec{x}$, and a near-field source location, $\vec{y}$, respectively. Using the partial wave expansion, the boundary integral in Eq. 3.3 can be written as

$$\int_{S_0}\left[\frac{\partial p(\vec{y})}{\partial n_y}G(\vec{x},\vec{y}) - \frac{\partial G(\vec{x},\vec{y})}{\partial n_y}p(\vec{y})\right]dS = \frac{ik}{4\pi}\sum_{n=0}^{\infty}(2n+1)\sum_{m=-n}^{n} O_n^m(\overrightarrow{o\vec{x}})M_n^m(\vec{o}). \tag{3.11}$$

Therefore, following the notation from Eq. 3.6, one can write multipole expansions $M_n^m(\vec{o})$ as

$$M_n^m(\vec{o}) = \int_{S_0}\left[\frac{\partial p(\vec{y})}{\partial n_y}\overline{I_n^m}(\overrightarrow{o\vec{y}}) - \frac{\partial \overline{I_n^m}(\overrightarrow{o\vec{y}})}{\partial n_y}p(\vec{y})\right]dS \tag{3.12}$$

where the term $\partial\overline{I_n^m}(\overrightarrow{o\vec{y}})/\partial n_y$ is computed as

$$\frac{\partial\overline{I_n^m}(\overrightarrow{o\vec{y}})}{\partial n_y} = \frac{\partial\overline{I_n^m}(\overrightarrow{o\vec{y}})}{\partial r}\frac{\partial r}{\partial n_y} + \frac{\partial\overline{I_n^m}(\overrightarrow{o\vec{y}})}{\partial \theta}\frac{\partial \theta}{\partial n_y} + \frac{\partial\overline{I_n^m}(\overrightarrow{o\vec{y}})}{\partial \phi}\frac{\partial \phi}{\partial n_y}. \tag{3.13}$$

The multipole to multipole (Eq. 3.14), multipole to local (Eq. 3.15) and local to local (Eq. 3.16) expansions and translations are given by

$$M_n^m(\vec{o}^{\,'}) = \sum_{n'=0}^{\infty}\sum_{m'=-n'}^{n'}\sum_{l=|n-n'|}^{n+n'}(2n'+1)(-1)^{m'}W_{n,n',m,m',l}I_l^{-m-m'}(\overrightarrow{o'o})M_{n'}^{-m'}(\vec{o}), \tag{3.14}$$

$$L_n^m(\vec{o}^{\,'}) = \sum_{n'=0}^{\infty}\sum_{m'=-n'}^{n'}\sum_{l=|n-n'|}^{n+n'}(2n'+1)W_{n',n,m',m,l}\widetilde{O_l}^{-m-m'}(\overrightarrow{oo'})M_{n'}^{m'}(\vec{o}), \tag{3.15}$$

$$L_n^m(\vec{o}^{\,'}) = \sum_{n'=0}^{\infty}\sum_{m'=-n'}^{n'}\sum_{l=|n-n'|}^{n+n'}(2n'+1)(-1)^{m}W_{n',n,m',-m,l}I_l^{m-m'}(\overrightarrow{oo'})L_{n'}^{m'}(\vec{o}). \tag{3.16}$$

In Eq. 3.14, $\vec{o}^{\,'}$ is the center of a parent box and $\vec{o}$ is the center of one of its children. In Eq. 3.15, $\vec{o}^{\,'}$ is the center of a box b and $\vec{o}$ is the center of some box in $L_2(b)$ and, in Eq. 3.16, $\vec{o}^{\,'}$ is the center of a child box with parent box centroid at $\vec{o}$ position. For all these expressions, the summations in l, $\sum_{l=|n-n'|}^{n+n'}$, are performed only for even values of $n+n'-l$. Also in these formulas, the term $\widetilde{O_n^m} = h_n^{(1)}(kr)\overline{Y_n^m}(\theta,\phi)$, and the term $W_{n,n',m,m',l}$ is computed using the formula

$$W_{n,n',m,m',l} = (2l+1)i^{n'-n+l}\begin{pmatrix} n & n' & l \\ 0 & 0 & 0 \end{pmatrix}\begin{pmatrix} n & n' & l \\ m & m' & t \end{pmatrix} \tag{3.17}$$

where $t=-m-m'$ and $\begin{pmatrix} a & b & c \\ d & e & f \end{pmatrix}$ denotes the Wigner 3j symbol, which can be computed using the Racah formula (Messiah, 1981). Finally, we can also write the boundary integral equation as a function of the local expansions

$$\int_{S_0}\left[\frac{\partial p(\vec{y})}{\partial n_y}G(\vec{x},\vec{y}) - \frac{\partial G(\vec{x},\vec{y})}{\partial n_y}p(\vec{y})\right]dS = \frac{ik}{4\pi}\sum_{n=0}^{\infty}(2n+1)\sum_{m=-n}^{n}\overline{I_n^m}(\overrightarrow{o\vec{x}})L_n^m(\vec{o}). \tag{3.18}$$

3.2.3 Rotation-Coaxial Translation Method

The rotation-coaxial translation method uses the same boundary integral equations as the partial wave expansion method. However, multipole to multipole, multipole to

local and local to local translations are accelerated through an adequate rotation of the spherical harmonics. The method consists of performing a rotation of the z Cartesian axis towards the direction of translation, then executing the translation along the new z axis and, finally, performing another rotation to the original Cartesian system. While in the partial wave expansion method the computational complexity of translations are proportional to $O(p^5)$, with p equal to the number of truncation terms in the FMM series, in the rotation-coaxial translation method the computational complexity is proportional to $O(p^3)$ since rotations and translations along the z direction (coaxial translations) require $O(p^3)$ operations. As shown by White and Head-Gordon (1996), coaxial translations do not change the orders of the translated coefficients and translations are performed for each order independently. Making use of this property we can compute the coaxial translation matrices $T^m_{n,n'}(M2M)$, $T^m_{n,n'}(M2L)$ and $T^m_{n,n'}(L2L)$ given by

$$T^m_{n,n'}(M2M) = \sum_{n'=0}^{\infty} \sum_{l=|n-n'|}^{n+n'} (2n'+1)(-1)^{-m} W_{n,n',m,-m,l} j_l(k|\overrightarrow{o'o}|), \tag{3.19}$$

$$T^m_{n,n'}(M2L) = \sum_{n'=0}^{\infty} \sum_{l=|n-n'|}^{n+n'} (2n'+1)(-1)^{-m} W_{n',n,-m,m,l} h_l(k|\overrightarrow{o'o}|) \tag{3.20}$$

and

$$T^m_{n,n'}(L2L) = \sum_{n'=0}^{\infty} \sum_{l=|n-n'|}^{n+n'} (2n'+1)(-1)^{m} W_{n',n,m,-m,l} j_l(k|\overrightarrow{o'o}|). \tag{3.21}$$

In Eqs. 3.19 and 3.21, o' is the centroid of box b's parent and o is the centroid of box b. In Eq. 3.20, o' is the centroid of some box in $L_2(b)$ and o is the centroid of box b.

Arbitrary rotations in three dimensions can be defined in terms of the Euler angles, $(\alpha_E, \beta_E, \gamma_E)$. For the forward rotation of the z axis towards the direction of translation we apply a rotation in the direction $(\alpha_E, \beta_E, 0)$ and for the backward rotation we apply a rotation in the direction $(-\alpha_E, -\beta_E, 0)$. As pointed out by White and Head-Gordon (1996), the degree of the spherical harmonics do not change under rotations. Making use of this property we can compute the rotation matrices $R_n^{m,m'}(\beta_E) = R_n^{m',m}(-\beta_E)$ by

$$R_n^{m,m'}(\beta_E) = \left[\left(n+m'\right)!\left(n-m'\right)!\,(n+m)!\,(n+m)!\right]^{1/2}$$

$$\times \sum_{s=max(0,m-m')}^{min(n+m,n-m')} \frac{(-1)^{m'-m+s}(cos\frac{\beta_E}{2})^{2n+m-m'-2s}(sin\frac{\beta_E}{2})^{m'-m+2s}}{(n+m-s)!\,(m'-m+s)!\,(n-m'-s)!s!}. \tag{3.22}$$

Therefore, the multipole to multipole expansions are given by Eqs. 3.23, 3.24 and 3.25

$$\widehat{M_n^m}(\vec{o}) = \sum_{m'=-n}^{n} R_n^{m',m}(\beta_E) e^{im'\alpha_E} M_n^{m'}(\vec{o}), \tag{3.23}$$

$$\widehat{M_n^m}(\vec{o'}) = \sum_{n'=0}^{\infty} T_{n,n'}^{m}(M2M) \widehat{M_{n'}^m}(\vec{o}), \tag{3.24}$$

$$M_n^m(\vec{o'}) = \sum_{m'=-n}^{n} R_n^{m,m'}(\beta_E) e^{-im\alpha_E} \widehat{M_n^{m'}}(\vec{o'}), \tag{3.25}$$

where the angles α_E and β_E are the azimuthal and polar angles of $\vec{o}$, respectively. The multipole to local expansions are given by Eqs. 3.26, 3.27 and 3.28

$$\widehat{M_n^m}(\vec{o}) = \sum_{m'=-n}^{n} R_n^{m',m}(\beta_E) e^{im'\alpha_E} M_n^{m'}(\vec{o}), \tag{3.26}$$

$$\widehat{L_n^m}(\vec{o'}) = \sum_{n'=0}^{\infty} T_{n,n'}^{m}(M2L) \widehat{M_{n'}^{-m}}(\vec{o}), \tag{3.27}$$

$$L_n^m(\vec{o'}) = \sum_{m'=-n}^{n} R_n^{m,m'}(\beta_E) e^{-im\alpha_E} \widehat{L_n^{m'}}(\vec{o'}). \tag{3.28}$$

The local to local expansions are given by Eqs. 3.29, 3.30 and 3.31

$$\widehat{L_n^m}(\vec{o}) = \sum_{m'=-n}^{n} R_n^{m',m}(\beta_E) e^{-im'\alpha_E} L_n^{m'}(\vec{o}), \tag{3.29}$$

$$\widehat{L_n^m}(\vec{o'}) = \sum_{n'=0}^{\infty} T_{n,n'}^{m}(L2L) \widehat{L_{n'}^m}(\vec{o}), \tag{3.30}$$

$$L_n^m(\vec{o'}) = \sum_{m'=-n}^{n} R_n^{m,m'}(\beta_E) e^{im\alpha_E} \widehat{L_n^{m'}}(\vec{o'}). \tag{3.31}$$

Finally, one can solve the Helmholtz boundary integral equation as a function of the local expansions as in Eq. 3.18.

3.2.4 Plane Wave Expansion Method

In the plane wave expansion method the free space Green's function is written as the integral over plane waves along the unit sphere

$$G(\vec{x}, \vec{y}) = \frac{ik}{16\pi^2} \oint e^{-i\vec{k}\cdot\vec{oy}} D(\vec{ox}, \vec{k}) d(\vec{k}/|\vec{k}|), \tag{3.32}$$

and the diagonal translation operator is given by

$$D(\overrightarrow{ox},\vec{k}) = \sum_{n=0}^{\infty} i^n(2n+1)h_n^{(1)}(k|\overrightarrow{ox}|)P_n\left(\vec{k}/|\vec{k}|\cdot\overrightarrow{ox}/|\overrightarrow{ox}|\right). \tag{3.33}$$

Here, P_n stands for the $n-th$ degree Legendre polynomial. Thus, the boundary integral in Eq. 3.3 can be written as

$$\int_{S_0}\left[\frac{\partial p(\vec{y})}{\partial n_y}G(\vec{x},\vec{y}) - \frac{\partial G(\vec{x},\vec{y})}{\partial n_y}p(\vec{y})\right]dS = \frac{ik}{16\pi^2}\oint D(\overrightarrow{ox},\vec{k})M(\vec{o},\vec{k})d(\vec{k}/|\vec{k}|). \tag{3.34}$$

Therefore, following the notation from Eq. 3.6, one can write multipole expansions $M(\vec{o},\vec{k})$ as

$$M(\vec{o},\vec{k}) = \int_{S_0}\left[\frac{\partial p(\vec{y})}{\partial n_y}e^{-i\vec{k}\cdot\overrightarrow{oy}} - ik(\vec{n}_y\cdot\vec{k})e^{-i\vec{k}\cdot\overrightarrow{oy}}p(\vec{y})\right]dS. \tag{3.35}$$

In the plane wave expansion method, multipole to multipole and local to local translations are performed by plane waves represented along the unit sphere. The plane wave directions on the unit sphere, $\vec{k}$, are given by the polar and azimuthal angles (θ_{lv},ϕ_{lv}). For each refinement level, lv, the number of wave samples is increased if the translation is from an upper level to a lower level (M2M) or decreased if the translation is from a lower level to an upper level (L2L). Therefore, interpolation and filtering of multipole and local expansions are performed over the sphere surface. The interpolation/filtering method used in this work is the spherical truncation method presented by Jakob-Chien and Alpert (1997). The wave samples along the ϕ_{lv} directions are equispaced on the interval $[0,2\pi]$ and the wave samples along the θ_{lv} directions are given by $\arccos(\lambda_h)$, where λ_h are the nodes of the H-point Gaussian quadrature on the interval $[-1,1]$. The computations for multipole to multipole expansions are split in 2 steps given by interpolation and shifting. The interpolation step is performed as

$$f^n(\theta_h^{lv+1}) = \frac{2\pi}{J}\sum_{j=1}^{J} M(\vec{o},\theta_h^{lv+1},\phi_j^{lv+1})e^{-in\phi_j^{lv+1}}, \tag{3.36}$$

$$\widehat{f^n}(\theta_h^{lv}) = \sum_{h^{lv+1}=1}^{H^{lv+1}} f^n(\theta_h^{lv+1})\omega_h^{lv+1}\epsilon_{N+1}^n \tag{3.37}$$

$$\times\left[\frac{P_{N+1}^n(\cos(\theta_h^{lv}))P_{N+1}^n(\cos(\theta_h^{lv+1}))}{\cos(\theta_h^{lv})-\cos(\theta_h^{lv+1})} - \frac{P_{N+1}^n(\cos(\theta_h^{lv}))P_{N+1}^n(\cos(\theta_h^{lv+1}))}{\cos(\theta_h^{lv})-\cos(\theta_h^{lv+1})}\right]$$

and

$$M(\vec{o}, \theta_h^{lv}, \phi_j^{lv}) = \frac{1}{2} \sum_{n=-N}^{N} \widehat{f^n}(\theta_h^{lv}) e^{in\phi_j^{lv}}. \tag{3.38}$$

In Eq. 3.37, the term $\epsilon_l^n = \sqrt{l^2 - n^2/4l^2 - 1}$ and ω_h is the $h-th$ Gaussian quadrature weight. The superscripts lv and $lv+1$ appearing in the wave samples (θ, ϕ) indicate that the grid points are sampled for each refinement level lv. For instance, θ_h^{lv} is the $h-th$ θ grid point for refinement level lv and θ_h^{lv+1} is the $h-th$ θ node for refinement level $lv+1$. The same notation applies to grid points in the ϕ direction. Finally, the shifting step from centroids of children boxes to centroids of parent boxes using plane wave expansions is computed as

$$M(\vec{o'}, \vec{k}) = e^{i\vec{k}\cdot\overrightarrow{oo'}} M(\vec{o}, \vec{k}). \tag{3.39}$$

Multipole to local calculations are performed by the diagonal translation operator

$$D(\overrightarrow{oo'}, \vec{k}) = \sum_{n=0}^{\infty} i^n (2n+1) h_n(k|\overrightarrow{oo'}|) P_n\left(\vec{k}/|\vec{k}| \cdot \overrightarrow{oo'}/|\overrightarrow{oo'}|\right) \tag{3.40}$$

and local to local translations are performed by a formulation similar to that used in the multipole to multipole expansions. The first step consists of shifting local representations from centroids of parent boxes to centroids of children boxes using plane waves

$$L(\vec{o'}, \vec{k}) = e^{i\vec{k}\cdot\overrightarrow{oo'}} L(\vec{o}, \vec{k}). \tag{3.41}$$

Then, a filtering process is applied using the spectral truncation method

$$f^n(\theta_h^{lv-1}) = \frac{2\pi}{J} \sum_{j=1}^{J} L(\vec{o'}, \theta_h^{lv-1}, \phi_j^{lv-1}) e^{-in\phi_j^{lv-1}}, \tag{3.42}$$

$$\widehat{f^n}(\theta_h^{lv}) = \sum_{h^{lv+1}=1}^{H^{lv-1}} f^n(\theta_h^{lv-1}) \omega_h^{lv-1} \epsilon_{N+1}^n \tag{3.43}$$

$$\times \left[\frac{P_{N+1}^n(\cos(\theta_h^{lv})) P_{N+1}^n(\cos(\theta_h^{lv-1}))}{\cos(\theta_h^{lv}) - \cos(\theta_h^{lv-1})} - \frac{P_{N+1}^n(\cos(\theta_h^{lv})) P_{N+1}^n(\cos(\theta_h^{lv-1}))}{\cos(\theta_h^{lv}) - \cos(\theta_h^{lv-1})} \right]$$

and

$$L(\vec{o'}, \theta_h^{lv}, \phi_j^{lv}) = \frac{1}{2} \sum_{n=-N}^{N} \widehat{f^n}(\theta_h^{lv}) e^{in\phi_j^{lv}}. \tag{3.44}$$

In order to perform fast interpolation and filtering, a Fast Fourier Transform is applied to Eqs. 3.36 and 3.42 and an inverse Fast Fourier Transform is applied to Eqs. 3.38 and 3.44.

Finally, similarly to the previous methods, we can also write the boundary integral equation for the plane wave expansion method as a function of the local expansions

$$\int_{S_0} \left[\frac{\partial p(\vec{y})}{\partial n_y} G(\vec{x},\vec{y}) - \frac{\partial G(\vec{x},\vec{y})}{\partial n_y} p(\vec{y}) \right] dS = \frac{ik}{16\pi^2} \sum_{s=1}^{S} \omega_s e^{i\vec{k}\cdot\vec{o}\vec{y}} L(\vec{o},\vec{k}), \tag{3.45}$$

where the sum on s is calculated for all wavenumber directions $\vec{k}$ and ω_s represents the multiplication of weights of the trapezoidal and Gaussian integrations performed over the unit sphere.

3.2.5 Wideband Fast Multipole Method

The wideband FMM described here uses the partial wave expansion formulation with rotation-coaxial translation for computations in the low-frequency regime and the plane wave expansion formulation with fast spherical interpolation and filtering and diagonal translation in the high-frequency regime. A schematic diagram of the method can be observed in Fig. 3.4. In this figure, the subscript terms LF and HF stand for low-frequency (operations are performed by the rotation-coaxial translation formulation) and high-frequency (operations are performed by the plane wave expansion formulation), respectively.

Conversions from multipole expansions to local representations around centroids of well-separated boxes are the most expensive step when the FMM is applied to the BEM. The computational costs for the M2L operations performed by the rotation-coaxial translation and plane wave expansion formulations scale with $O(\varphi_{lv}^3)$ and $O(\varphi_{lv}^2)$, respectively, where φ_{lv} is the number of truncation terms per level of refinement, lv, in the FMM series. Therefore, the latter formulation should be used whenever possible. However, computations performed using the plane wave expansion method become unstable for higher levels of refinement with small local Helmholtz numbers or for simulations with very low frequencies. This problem is referred in the literature as subwavelength breakdown and the authors refer to the work from Dembart and Yip (1998), Nishimura (2002), Hastriter *et. al* (2003) and Cheng *et. al* (2006) for a detailed discussion on the topic. In order to overcome this drawback, the rotation-coaxial translation formulation, which is stable for low-frequencies, is applied to the higher levels of refinement with small local Helmholtz numbers. The cost for these computations are reduced since this formulation is only used for high levels of refinement where the number of truncation terms φ_{lv} is relatively small. The boundary between the low-frequency and high-frequency regimes is defined by the desired accuracy of the method. Following the

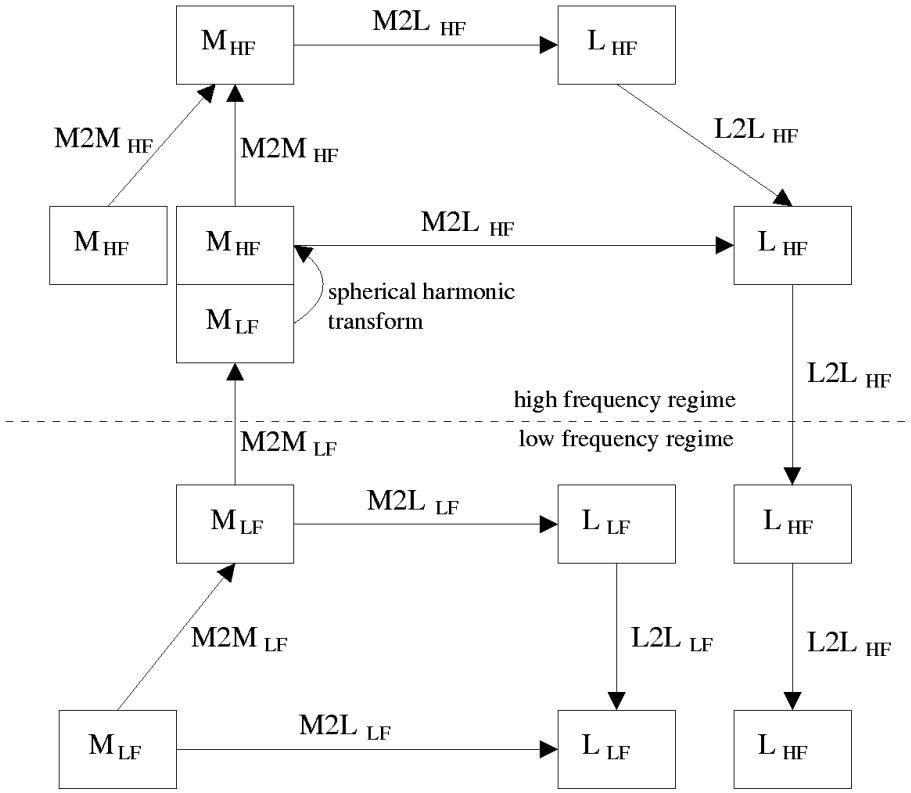

Figure 3.4: Schematic diagram for the wideband multi-level FMM algorithm.

results presented by Cheng *et. al* (2006), the low-frequency formulation is applied when the local box size a_{lv} becomes $a_{lv} < 0.25\lambda$, where λ is the acoustic wavelength. Gumerov and Duraiswami (2009) presented a more sophisticated method to select between low and high-frequency limits. However, their method seems to be over restrictive.

In the FMM formulations, the number of terms used in the functions O, I and D and the number of plane wave samples $\vec{k}$ along the unit sphere have to be truncated. Different formulae are presented in the literature for the computation of the number of truncation terms and plane wave samples for each refinement level. Coifman *et. al* (1993) proposed the empirical formula $\varphi_{lv} = \lfloor ka_{lv} + c\ log(ka_{lv} + \pi) \rfloor$, where $\lfloor \cdot \rfloor$ stands for the integer part. Darve (2000a) considered this formula on his error analysis and study of asymptotic complexity of the Gegenbauer series. Koc *et. al* (1999) proposed the excess bandwidth formula (EBF) $\varphi_{lv} = ka_{lv} + c\ (ka_{lv})^{1/3}$ that is used by Hastriter *et. al* (2003) and Cecka and Darve (2013). In these formulae, a_{lv} is the box size at refinement level lv and the constant c controls the desired accuracy of the solution. An empirically determined common choice (Hastriter *et. al*, 2003; Cecka and Darve, 2013) is given by $c = 1.8(d)^{2/3}$ where d is the number of digits of accuracy. The former formula is slightly more conservative than the latter and is used in the current computations of acoustic scattering. In these simulations, the number of plane wave samples per refinement level is $2\varphi_{lv}$ along the azimuthal direction and φ_{lv} along the polar direction. In order to verify

the performance of the wideband FMM, numerical simulations were performed for the acoustic scattering along a rigid sphere for Helmholtz number 1.57 for different ratios a_{lv}/λ. Stable and accurate results are obtained for a less restrictive ratio of $a_{lv}/\lambda = 0.1$ for values of the parameter $c = 8$ and the reduction of the low-frequency/high-frequency switch improves the performance of the method in terms of computational time.

During the translations from higher to lower levels of refinement the local Helmholtz numbers increase and the high-frequency formulation can be applied. Therefore, the multipole expansions are converted from the low-frequency to the high-frequency formulation through a spherical harmonic transform as shown in the wideband FMM diagram from Fig. 3.4. The spherical harmonic transform and its inverse operation are given by

$$M(\vec{o},\vec{k}) = \sum_{n=0}^{\infty} i^n(2n+1)(-1)^{n-1} \sum_{m=-n}^{n} \overline{Y_n^m}(\theta,\phi) M_n^m(\vec{o})$$

and

$$M_n^m(\vec{o}) = \frac{1}{4\pi} \oint i^{-n}\overline{Y_n^m}(\theta,\phi)(-1)^{n-1} M(\vec{o},\vec{k}) d(\vec{k}/|\vec{k}|),$$

where θ and ϕ are the polar and azimuthal angles from the plane wave sample $\vec{k}$.

As pointed out by Cheng *et. al* (2006), FMM solutions with higher accuracy can be obtained by increasing the ratio a_{lv}/λ and a higher computational cost is associated with this accuracy increase. This increase in computational cost is hard to estimate because it depends on the number of φ_{lv} terms and also on the number of boxes per level of adaptive refinement. It is shown by Cheng *et. al* (2006) that very accurate solutions can be obtained by a wideband FMM formulation. However, in this reference the authors do not solve a boundary integral equation (BIE) problem and only present a discussion about the accuracy of the FMM solution. If a BIE method is solved, additional errors are introduced by the mesh discretization and numerical integrations. For instance, it is possible to obtain very accurate matrix-vector multiplications with the FMM depending on the value of parameter c and on the ratio a_{lv}/λ, but still one can obtain a large overall error due to BEM discretization errors such as those mentioned above. Therefore, if very accurate FMM-BEM solutions are required, all sources of error have to be treated adequately.

3.3 Pseudo-Spectral Method

The classical Kirchhoff-Love plate theory is applied to model thin plates. To obtain the equations of motion for rectangular plates including the appropriate boundary conditions we employ the variational approach (Timoshenko and Woinowsky-Krieger, 1959; Dym and

Shames, 2013). Assuming a harmonic excitation, the free vibration of isotropic plates is governed by the following differential equation

$$\tilde{D}\nabla^4\tilde{w} - \tilde{m}\tilde{\omega}^2\tilde{w} = 0 \tag{3.46}$$

where ∇^4 is the bi-harmonic differential operator, $\tilde{w}$ is the transverse displacement, $\tilde{\omega}$ is frequency, $\tilde{D} = \tilde{E}\tilde{h}^3/12(1-\nu^2)$ is the bending rigidity, $\tilde{E}$ is the Young modulus, $\tilde{h}$ is plate thickness, ν is Poisson's ratio and $\tilde{m}$ is the mass density per unit of area of the plate. The non-dimensional version of the above equation can be written as

$$\nabla^4 w - \beta^4 w = 0 \tag{3.47}$$

with $\beta^4 = \tilde{\omega}^2\tilde{c}^4\tilde{m}/\tilde{D}$ as a non-dimensional parameter for frequency. In this work, we are mostly interested in the study of cantilever configurations and, hence, the important boundary conditions for the plate are those of clamped and free edges. The boundary conditions may be applied to any edge parallel to the y-axis, for example, the boundaries $x = 0$ and $x = c$. The corresponding conditions can be obtained for the edges parallel to the x-axis, for example, the boundaries $y = 0$ and $y = b$, by interchanging x and y in the equations (3.48) and (3.49). The boundary condition for a clamped edge can be written as

$$\begin{aligned} w &= 0, \\ \frac{\partial w}{\partial x} &= 0. \end{aligned} \tag{3.48}$$

The free edges require the application of two boundary conditions, one for the bending moment and another for the shear forces and, for rectangular coordinates, they can be written as

$$\begin{aligned} M_{xx} &= -D\left[\frac{\partial^2 w}{\partial x^2} + \nu\frac{\partial^2 w}{\partial y^2}\right] = 0, \\ V_x &= -D\left[\frac{\partial^3 w}{\partial x^3} + (2-\nu)\,\frac{\partial^3 w}{\partial x \partial y^2}\right] = 0. \end{aligned} \tag{3.49}$$

Finally, we have to consider the corner condition that must be applied to the free corner formed by the intersection of the free edges. The twisting moment M_{xy} must be set to zero as

$$-D\,(1-\nu)\,\frac{\partial^2 w}{\partial x \partial y} = 0. \tag{3.50}$$

The edge conditions presented above are valid only for rectangular plates. In the present work, we are interested in the study of the effects of non-zero sweep angles Λ and, in this case, we must decompose all bending and twisting moments applied to the boundary edges in the normal and tangential directions. Figure (3.5) shows a quadrilateral

plate with a sweep angle Λ at the trailing edge and Eqs. (3.48) – (3.50) must be rewritten in function of the coordinate system (n, s) (Dym and Shames, 2013). Therefore, for a clamped condition one has

$$\begin{aligned} w &= 0, \\ \frac{\partial w}{\partial n} &= 0, \end{aligned} \tag{3.51}$$

and for a free edge,

$$\begin{aligned} M_{nn} &= -D\left[\frac{\partial^2 w}{\partial n^2} + \nu\frac{\partial^2 w}{\partial s^2}\right] = 0, \\ V_n &= -D\frac{\partial}{\partial n}\left[\frac{\partial^2 w}{\partial n^2} + (2-\nu)\frac{\partial^2 w}{\partial s^2}\right] = 0. \end{aligned} \tag{3.52}$$

For a corner condition, we have

$$-D\,(1-\nu)\,\frac{\partial^2 w}{\partial n \partial s} = 0. \tag{3.53}$$

We know that the transverse displacement $w(x, y)$ is computed in the original coordinate system (x, y) and, therefore, Eqs. (3.51) - (3.53) must be rewritten in terms of the original system. The local system (n, s) created to represent the sweep effects at the trailing edge, can be written as $n = n(x, y)$ and $s = s(x, y)$. Considering a sweep angle Λ at the trailing edge, as shown in Fig. 3.5, and applying the chain rule, we can write the derivatives as

$$\frac{\partial w}{\partial n} = \frac{\partial w}{\partial x}n_x + \frac{\partial w}{\partial y}n_y, \tag{3.54a}$$

$$\frac{\partial w}{\partial s} = -\frac{\partial w}{\partial x}n_y + \frac{\partial w}{\partial y}n_x, \tag{3.54b}$$

$$\frac{\partial^2 w}{\partial n^2} = \frac{\partial^2 w}{\partial x^2}n_x^2 + \frac{\partial^2 w}{\partial y^2}n_y^2 + 2\frac{\partial^2 w}{\partial x \partial y}n_x n_y, \tag{3.54c}$$

$$\frac{\partial^2 w}{\partial s^2} = \frac{\partial^2 w}{\partial x^2}n_y^2 + \frac{\partial^2 w}{\partial y^2}n_x^2 - 2\frac{\partial^2 w}{\partial x \partial y}n_x n_y. \tag{3.54d}$$

Using the set of equations (3.54), one can rewrite the boundary conditions for the clamped edge as

$$\begin{aligned} w &= 0, \\ \frac{\partial w}{\partial x}n_x + \frac{\partial w}{\partial y}n_y &= 0, \end{aligned} \tag{3.55}$$

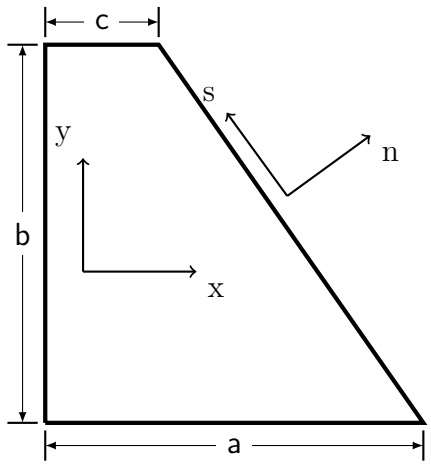

Figure 3.5: Sketch of a quadrilateral plate with a sweep angle at the trailing edge.

and for the swept free edge as

$$M_{nn} = -D\left(\frac{\partial^2 w}{\partial x^2} + \nu\frac{\partial^2 w}{\partial y^2}\right)n_x^2 - D\left(\frac{\partial^2 w}{\partial y^2} + \nu\frac{\partial^2 w}{\partial x^2}\right)n_y^2 - 2\left(1-\nu\right)D\frac{\partial^2 w}{\partial x \partial y}n_x n_y,$$
$$V_n = -D\left[\frac{\partial^3 w}{\partial x^3} + \left(2-\nu\right)\frac{\partial^3 w}{\partial x \partial y^2}\right]n_x^3 - D\left[\frac{\partial^3 w}{\partial y^3} + \left(2-\nu\right)\frac{\partial^3 w}{\partial x^2 \partial y}\right]n_y^3 \quad (3.56)$$
$$-D\left(2-\nu\right)\left[\frac{\partial^3 w}{\partial x^3}n_x n_y^2 + \frac{\partial^3 w}{\partial y^3}n_x^2 n_y\right] + D\left(1-2\nu\right)\left[\frac{\partial^3 w}{\partial x \partial y^2}n_x n_y^2 + \frac{\partial^3 w}{\partial x^2 \partial y}n_x^2 n_y\right]$$

For the corner, one has

$$-D\left(1-\nu\right)\left[\left(\frac{\partial^2 w}{\partial y^2} - \frac{\partial^2 w}{\partial x^2}\right)n_x n_y + \frac{\partial^2 w}{\partial x \partial y}\left(n_x^2 - n_y^2\right)\right] = 0. \quad (3.57)$$

The vibration of the plate is obtained by solving Eq. (3.47) subjected to the boundary conditions from Eqs. (3.51) - (3.53) and the pseudo-spectral method (also known as collocation spectral method) is employed to achieve spectral accuracy. The pseudo-spectral method is applied as an interpolatory method for an unknown function $w(\xi_i, \eta_j)$ which requires that the interpolant at each set of grid points $\{\xi_i, \eta_j\}$ provides zero residual, in other words, the approximation must be exact on the grid points (Boyd, 2001). We use the Chebyshev Gauss-Lobatto points to set up a grid which can be written as

$$\begin{aligned} \xi_i &= \cos\left(\frac{\pi i}{N_x}\right), \quad i = 0, 1, \ldots, N_x \quad with \quad x \in [-1, 1], \\ \eta_j &= \cos\left(\frac{\pi j}{N_y}\right), \quad i = 0, 1, \ldots, N_y \quad with \quad y \in [-1, 1]. \end{aligned} \quad (3.58)$$

This grid based on Chebyshev points is used to obtain $\{\xi_i, \eta_j\}$ independently in each direction so we can apply the *tensor product grid* (Trefethen, 2000), also known as

Kronecker product. In this work, the interpolant uses Lagrange polynomials based on the grid points $\{\xi_i, \eta_j\}$ and the Chebyshev differential matrices ($\mathcal{D}$) approach (Trefethen, 2000) is applied to approximate the derivatives. The Chebyshev differential matrix is written as $\mathcal{D}^1_{N_x}$, where N_x is the number of grid points along the x-axis and "1" represents the first derivative operator. The second derivative operator is computed by $\mathcal{D}^2_{N_x} = \mathcal{D}^1_{N_x}.\mathcal{D}^1_{N_x}$, *i.e.*, the square of $\mathcal{D}^1_{N_x}$. We also define auxiliary variables

$$w_1 = w \tag{3.59a}$$

$$w_2 = \frac{\partial^2 w}{\partial x^2} \tag{3.59b}$$

$$w_3 = \frac{\partial^2 w}{\partial y^2} \tag{3.59c}$$

such that the eigenvalue problem represented by Eq. (3.47) can be rewritten as

$$\begin{bmatrix} \mathcal{D}_x^2 & -\mathcal{I} & 0 \\ \mathcal{D}_y^2 & 0 & -\mathcal{I} \\ 0 & \nabla^2 & \nabla^2 \end{bmatrix} \begin{bmatrix} w_1 \\ w_2 \\ w_3 \end{bmatrix} = \beta^4 \begin{bmatrix} 0 & 0 & 0 \\ 0 & 0 & 0 \\ \mathcal{I} & 0 & 0 \end{bmatrix} \begin{bmatrix} w_1 \\ w_2 \\ w_3 \end{bmatrix}, \tag{3.60}$$

where $\mathcal{D}_x = \partial/\partial x$, $\mathcal{D}_y = \partial/\partial y$ and $\mathcal{I}$ is the identity operator. The derivative operators are obtained by the *Kronecker product* (Trefethen, 2000) written as $\mathcal{D}^2_x = \mathcal{D}^2_{N_x} \otimes \mathcal{I}$ and $\mathcal{D}^2_y = \mathcal{I} \otimes \mathcal{D}^2_{N_y}$.

The pseudo-spectral method uses orthogonal polynomials that are restricted on the domain $[-1, 1]$. In this work, the physical domain is arbitrary even for rectangular plates, *i.e.*, we can obtain the modal basis for a plate of arbitrary geometry $\{x_i, y_j\}$. We must then transform the grid in the physical space $\{x_i, y_j\}$ to a rectangular grid in terms of a computational space $\{\xi_i, \eta_j\}$, that is, the governing equations of the problem including the boundary conditions must be transformed from (x, y) to (ξ, η) as the new independent variables. In other words, we need to replace the x, y derivatives in the equations with the corresponding derivatives with respect to ξ, η (Anderson and Wendt, 1995; Liseikin, 2009). Boundary conditions are then imposed by replacing the lines of the above system with the required conditions at the plate edges. The numerical solution of the eigenvalue problem provides the values of the natural frequencies and the mode shapes of the vibrating plates which are interpolated in a grid with locations chosen to be appropriate for the application of the boundary element method for the acoustic problem.

3.4 Finite Element Method

In the present work, the finite element method, FEM, is employed to obtain the vibration modes of the plate using the commercial software ANSYS. The finite element model of a Kirchhoff plate theory is developed using its virtual work statement and an interpolation of the displacement field over the finite element (Reddy, 2006). The plate is discretized using a linear function with four nodes element SHELL181 or quadratic function with for eight nodes element SHELL281 implemented in the ANSYS Mechanical package. The elements have six degrees of freedom at each node and assume a finite element approximation of the form

$$\tilde{w}(\tilde{x},\tilde{y},\tilde{t}) = \sum_{j=1}^{n} \Delta_j^e(\tilde{t})\varphi_j^e(\tilde{t})(\tilde{x},\tilde{y}), \tag{3.61}$$

where Δ_j^e are the values of $\tilde{w}$ and its derivatives at the nodes, and φ_j^e are the interpolation functions. The element SHELL181 uses linear Lagrange polynomials as the interpolation function and the element SHELL281 uses quadratic polynomial. For these both elements the reduced integration schemes is employed. In the case of the free vibration problem, the response of the plate is assumed to be periodic in time. Thus, the final equation has the form of

$$([K^e] - \tilde{\omega}^2[M^e])\Delta^e = 0, \tag{3.62}$$

where $[K^e]$ is the structural stiffness matrix, $[M^e]$ is the structural mass matrix and $\tilde{\omega}$ is the frequency of natural vibration. Here, we have a generalized eigenproblem similar to that from the pseudo-spectral method discussed in section 3.3. However, the main difference is that, in the finite element method, the resultant matrix is symmetric and sparse, while in the spectral method the matrix is dense. To compute the eigenvalues and eigenvectors, the ANSYS software uses the block Lanczos method (ANSYS, Release 17.0). This formulation employs the weak form of the structural equations and, thus, the boundary conditions are satisfied for a free plate. So, for a cantilever plate configuration, one edge must be constrained with all degrees of freedom to avoid rotations and displacements. On the other hand, the other elements need to be constrained in three degrees of freedom including displacements along the x and y axes, and rotations in z. These conditions are required to satisfy the Kirchhoff plate theory.

Once the modal bases are computed from the FEM, their solutions must be adapted to employ in the FMM-BEM. Therefore, the displacements along the plate are interpolated to the centroids of the boundary elements using a linear interpolation. The application of the finite element method allows more general solutions in terms of arbitrary geometries.

Moreover, the method allows a fast convergence of the modal basis in terms of mesh refinement and the overall computational cost is reduced compared to the collocation spectral method. Hence, this is the method of choice in the investigations along this work, unless otherwise stated.

4 RESULTS AND DISCUSSION

4.1 Overview

This section presents results of acoustic scattering by square and trapezoidal poro-elastic plates for compact and non-compact acoustic sources. We also employ the current methodology for the calculation of acoustic scattering of poro-elastic plates including trailing-edge serrations, composite materials, different aspect ratios for plates immersed in air and submerged in water. The aim here is to investigate the effects of geometry and material properties on trailing-edge acoustic scattering by excitation from different acoustic sources. Once these effects are understood, we can provide a methodology for far-field noise mitigation through the design of quieter wings and blades.

Four plate configurations are employed in the first study and, for all cases, the plate surface area is kept constant. The leading edge is clamped and the trailing and lateral edges are free. This case is representative of a flap configuration, for example. The mean chord is unitary and the trailing edges have sweep angles of 0, 15, 30 and 45 deg. The BEM discretization needs to resolve both the acoustic and elastic waves along the plate surface and, for each plate configuration, a mesh convergence study is performed. It is found that, in order to resolve the bending wavelengths, the boundary element mesh requires 80000 quadrilateral elements for the square and trapezoidal plates.

The structural modes used in the simulations are previously computed and stored for fast calculation using the FMM-BEM. In Fig. 4.1, one can see the application of the FMM adaptive refinement technique along the plate surface for three configurations with and without sweep, and serrations. Figures 4.1 (a) and (b) provide a visualization of the FMM adaptive refinement for the plates with sweep angle $\Lambda = 0$ and 45 deg., respectively, and Fig. 4.1 (c) presents a detail view of the FMM adaptive refinement along the more complex plate geometry including serrations.

To use the present formulation of the FMM-BEM code, it is necessary to calculate the radiated sound by a plate of small but finite thickness. In the studies presented in this section, we have worked with plates of thickness h equal to 0.5% of the mean chord. In the cases analyzed, this thickness is much smaller than the acoustic wavelength and, therefore, the directivities obtained by the FMM-BEM are close to the expected results for plates of zero thickness (Crighton and Leppington, 1973). Throughout this chapter, unless otherwise stated, whenever elasticity effects are considered, we have chosen $\epsilon = 0.0021$ as

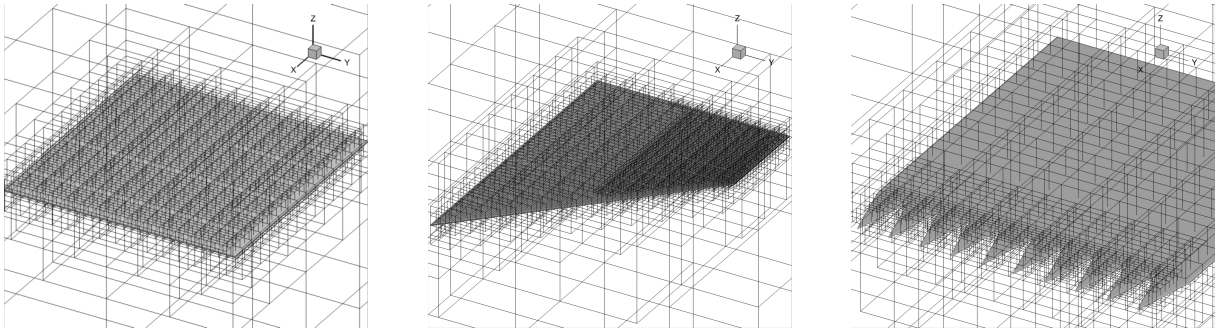

(a) Square plate. (b) Trapezoidal plate with sweep angle 45 deg. (c) Plate with serrations.

Figure 4.1: FMM adaptive refinement for different plate configurations.

representative of an aluminum plate immersed in air (Howe, 1998). This value is modified for the composite plates and when the plates are submerged in water, but these cases will be described in more details later.

The case of an impermeable elastic plate corresponds to $\alpha_H = 0$ in the present formulation and, then, Eq. (3.4) becomes

$$\frac{\partial p}{\partial n} = \frac{\epsilon k_0^5}{\Omega^6} \frac{\langle \Delta p, \phi_j \rangle}{\beta_j^4 - \frac{k_0^4}{\Omega^4}} \phi_j. \tag{4.1}$$

The case of a porous rigid plate corresponds to $\epsilon = 0$ in the present formulation, and Eq. (3.4) becomes

$$\frac{\partial p}{\partial n} = -\frac{\alpha_H K_R}{2R} \Delta p. \tag{4.2}$$

A poro-elastic plate has both $\alpha_H \neq 0$ and $\epsilon \neq 0$ and, therefore, it needs the full version of Eq. (3.4).

An overview of this chapter is provided as: in §4.2 we present a validation of the structural solutions for obtaining the modal bases. Section §4.3 shows the results of acoustic scattering by a compact quadrupole source. In this section, the plates are clamped on their leading edges simulating a flap. A study for different frequencies and sweep angles is presented for porous, elastic and poro-elastic plates. In §4.4 we discuss the results obtained for a non-compact source obtained from experiments. The source represents a turbulent jet and a jet-wing installation problem is modeled in the results presented in this section. A validation of the proposed formulation for acoustic scattering of poro-elastic plates is presented in §4.5. Here, we compare solutions in terms of three- and two-dimensional directivities of pressure in the far-field. Poro-elastic plates with serrated trailing edges are analyzed in §4.6 and, in §4.7 we provide results for elastic plates made of anisotropic composite materials. In the same section, we discuss the details for the choice of the composite plates. In §4.8 we present solutions of acoustic scattering

by poro-elastic plates of high aspect ratio, similar to configurations in helicopter rotors. Finally, in §4.9 we discuss about the noise reductions in the scattered field when the plates are submerged in water. This last section finds application in acoustic scattering by underwater devices such as submarines, for example.

4.2 Validation of the Modal Bases

In the present work, we employ a finite element solver (ANSYS, Release 17.0), FEM, to obtain the modal bases of the structural problem. We also implemented a collocation spectral method (CSM) to validate the modal bases through a comparison of the mode shapes and frequencies obtained by both formulations. It is worth mentioning that the finite element solution has a lower computational cost than that from the pseudo-spectral method.

Table 4.1 presents the natural frequencies for modes 1 to 4, 50, 100 and 500 obtained by the square plate used in the current studies. Results obtained by the spectral method and the FEM are compared to those obtained from the literature for the first four modes and a good agreement is found in terms of the natural frequencies, validating the current methodology for the vibration problem of square cantilever plates. We also perform a comparison between the spectral method and the FEM for higher-order modes. As one can see, these modes also show a good comparison between the two different numerical methodologies. For example, for mode 500, the relative error computed between the spectral method and the FEM is around 0.50%. A mesh convergence analysis is performed for the FEM using the CSM as the "correct" solution. Figure 4.2 shows the relative error between the FEM and CSM results for different modes. As one can see, the relative errors converge fast for lower-order modes and for mode 500, the error is of the order of 1%. One should remind that the CSM is also prone to numerical errors due mesh discretization. Therefore, the figure only shows that the relative errors converge, showing what is the minimal discretization for the FEM to resolve the modes of interest.

Mode	Dickinson and Di Blasio (1986)	Bardell (1991)	CSM	FEM
1	3.4712	3.47	3.4710	3.4706
2	8.5080	8.51	8.5061	8.4951
3	21.2878	21.29	21.2837	21.2767
4	—	27.20	27.1987	27.1770
50	—	—	554.1307	552.9239
100	—	—	1125.9759	1123.4226
500	—	—	5996.8589	5966.6993

Table 4.1: Natural frequencies ($\tilde{\omega}\tilde{c^2}\sqrt{\tilde{m}/\tilde{D}}$) for a square plate with unit chord.

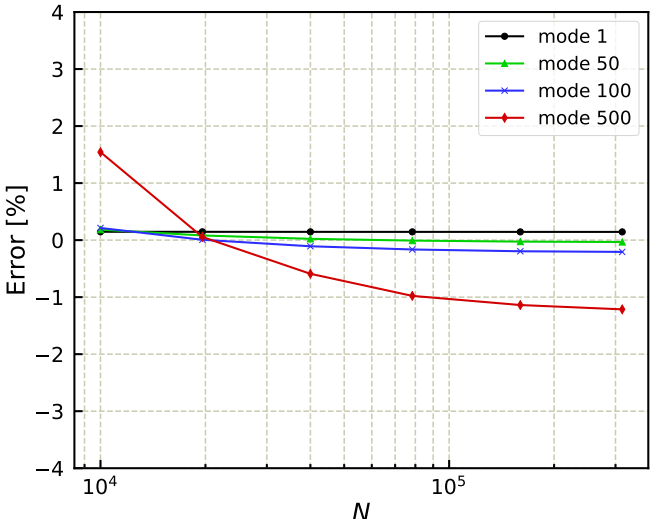

Figure 4.2: Convergence analysis of the FEM for a square plate.

In order to perform a similar validation procedure for trapezoidal plates, numerical results from the spectral method and the FEM are compared to those from Srinivasan and Babu (1983) in terms of frequencies of the first 4 modes on Table 4.2. As one can see, results are similar to those from the reference, although the agreement is not as good as for the rectangular plate. However, as a verification step, results from FEM and the spectral method have a good agreement.

In Figs. 4.3 and 4.4, one can observe the mode shapes obtained by the pseudo-spectral method and for the FEM for rectangular and trapezoidal plates for modes 1, 2 and 3. Here, the bottom sides of the plates are clamped, representing a clamped wing root. One of the edges of the plates is swept with an angle Λ. The visualization of the mode shapes obtained by different numerical techniques also serves to verify the solutions. From this figure, it is possible to see the lack of symmetry from the trapezoidal plates which should affect the propagation of elastic waves. Table 4.3 shows the natural frequencies for modes 1, 2 and 3, obtained by both numerical methods employed here. One can see that the increase in the trailing-edge sweep angle leads to a reduction of the natural frequencies for modes 1 and 3, while an increase in the natural frequency is observed for mode 2. This effect is expected and occurs for the first modes. For the higher order modes, this pattern is lost.

4.3 Compact Quadrupole Sources

Firstly, we calculate the sound radiated by a lateral point quadrupole source in the proximity of a free edge of several trapezoidal plates. The source has unit intensity and

Mode	Srinivasan and Babu (1983)	CSM	FEM
1	4.685	4.630	4.639
2	14.291	18.731	18.709
3	23.453	24.647	24.650
4	44.444	46.400	46.350

Table 4.2: Natural frequencies ($\tilde{\omega}\tilde{c}^2\sqrt{\tilde{m}/\tilde{D}}$) for trapezoidal plates ($a/b = 1$ & $c = 0.25a$ in Fig. 3.5).

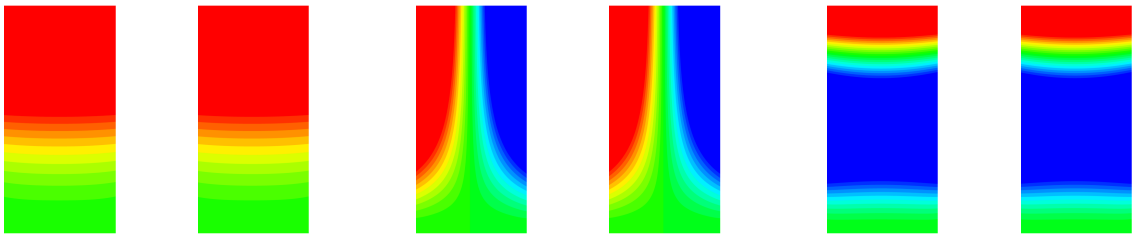

(a) Mode 1 (b) Mode 2 (c) Mode 3

Figure 4.3: Comparative modal basis between CSM (left) and FEM (right) solutions for rectangular plates.

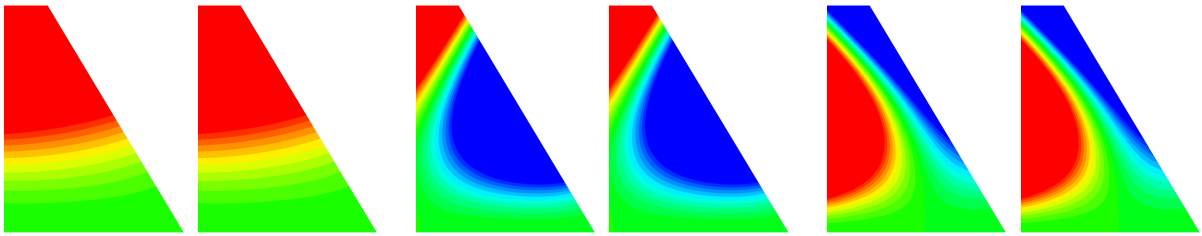

(a) Mode 1 (b) Mode 2 (c) Mode 3

Figure 4.4: Comparative modal basis between CSM (left) and FEM (right) solutions for swept plates.

Mode number	$\Lambda = 0°$	$\Lambda = 15°$	$\Lambda = 30°$	$\Lambda = 45°$
1	3.4706	3.3886	3.1308	2.6564
2	8.4951	8.6495	9.1225	9.6898
3	21.2767	20.2249	17.4699	14.3033

Table 4.3: Natural frequencies ($\tilde{\omega}\tilde{c}^2\sqrt{\tilde{m}/\tilde{D}}$) for different trapezoidal plates.

is placed in the proximity of the trailing edge of a 3D plate with normalized mean chord. Hence, from Eq. 3.3,

$$\mathcal{S}_i = \frac{\partial^2 G(\vec{x},\vec{z}_s)}{\partial z_{s_1}\partial z_{s_3}} = \frac{e^{ik_0|\vec{x}-\vec{z}_s|}}{4\pi|\vec{x}-\vec{z}_s|}\left(-k_0^2 - \frac{i\,3\,k_0}{|\vec{x}-\vec{z}_s|} + \frac{3}{|\vec{x}-\vec{z}_s|^2}\right)\frac{(x_1-z_{s_1})(x_3-z_{s_3})}{|\vec{x}-\vec{z}_s|^2}, \quad (4.3)$$

where $\vec{z}_s$ is the source position. The source is placed at the mid-span of the plate at $(x, y, z) = (1, 0, 0.01)$ and we present directivity plots for observers in the acoustic far-field

located 50 chords from the plate trailing edge, in the mid-span plane.

Besides the differences in sweep angle at the trailing edge, here, we also analyze the noise reduction effects from permeable-rigid, impermeable-elastic and poro-elastic plates. For all cases analyzed, the Helmholtz number is defined by $\mathrm{He} = \tilde{k}_0\tilde{L} = k_0$. In Figs. 4.5 (a) and (b), one can see the effects of sweep angle for impermeable-rigid plates for $k_0 = 1$ and 10. This figure allows an assessment of the plate compactness. For $k_0 = 1$, the acoustic wavelength is 2π and, therefore, the plate can be considered as compact. On the other hand, for $k_0 = 10$, the plate mean chord is larger than the acoustic wavelength and the plate behaves as a non-compact surface. When the trailing edge is not aligned with the axis of the incident quadrupole source, there is a considerable reduction in the noise scattering as discussed by Ffowcs Williams and Hall (1970). As expected, for the lower Helmholtz number analyzed, the far-field directivity resembles that of a compact dipole while, for the higher Helmholtz number, the typical multi-lobed directivity is observed. This multi-lobed directivity should approach a cardioid pattern in the limit of an infinite Helmholtz number, however, secondary leading-edge diffraction of the present finite chord plate will prevent such result (Roger and Moreau, 2005).

Figures 4.5 (c) and (d) present the results in terms of directivity plots for poro-elastic plate configurations with $\Omega = 0.1$, $\alpha_H = 0.002$ and $R = 0.001$, for $k_0 = 1$ and 10, respectively. We also add a small imaginary component to Ω to avoid singularities at resonances. For all cases analyzed of plates immersed in air, this component is equal to 3% of the real value of Ω. The combined effects of porosity and elasticity, together with trailing-edge sweep, lead to expressive reductions in the scattered sound. It is well known that the way elasticity changes the radiated sound depends critically on Ω (Howe, 1993a, 1998; Jaworski and Peake, 2013; Howe, 1993b) and significant changes compared to the rigid limit are expected for $\Omega \ll 1$, where theory predicts reductions in the radiated sound by elastic plates. In the results of Fig. 4.5, we notice significant reductions in noise scattering for poro-elastic plates compared to the rigid ones.

Cavalieri *et. al* (2016) show that, for plates of finite chord and infinite span, porosity is efficient in reductions of sound scattered for lower Helmholtz numbers whereas elasticity effects become more efficient for higher Helmholtz numbers. In the present study of plates with finite chord and span, three-dimensional effects are important in the acoustic scattering by poro-elastic plates since that bending waves propagate along all directions over the plate and suffer secondary diffraction along leading and lateral edges and corners, impacting the acoustic far-field radiation.

An assessment of the individual effects of porosity and elasticity on the noise reduction of plates with swept trailing edges is provided in Fig. 4.6 for $k_0 = 1$. In this figure, one can see that both porosity and elasticity have a similar effect in the noise reduction for

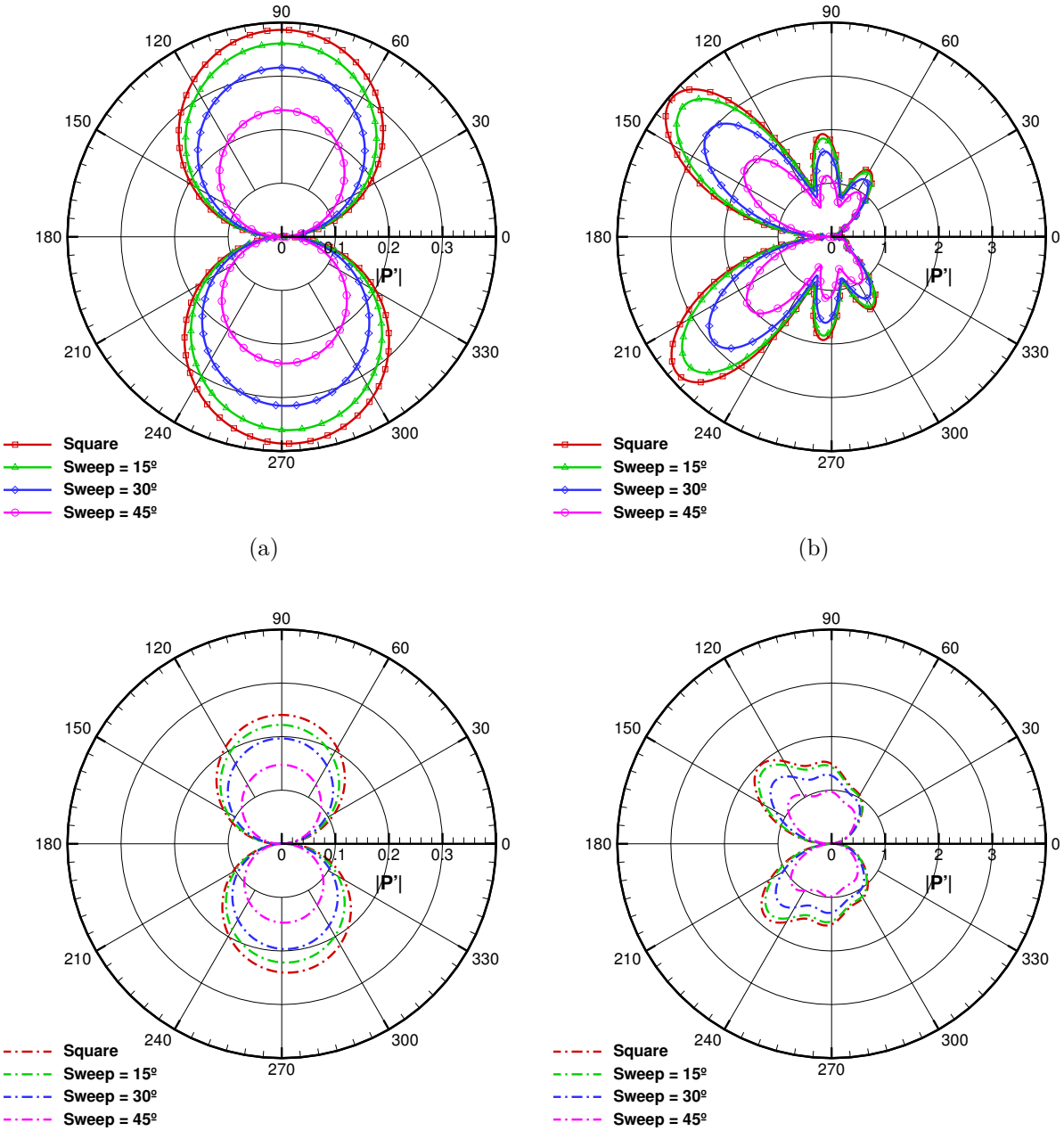

Figure 4.5: Directivities for different plate configurations at $k_0 = 1$ (left column) and $k_0 = 10$ (right column) due to a point quadrupole source placed at the plate trailing edge. Figs. (a) and (b) present the effects of the sweep angle for rigid plates, and Figs. (c) and (d) present the additional far-field noise reduction from poro-elastic plates with $\Omega = 0.1$, $\alpha_H = 0.002$ and $R = 0.001$.

the square and trapezoidal plates. As expected, porosity plays a more important role than elasticity for the current low Helmholtz number.

Figure 4.7 presents the total acoustic pressure for the rigid and poro-elastic plates analyzed, highlighting the plate trailing and leading edges by the abbreviations TE and

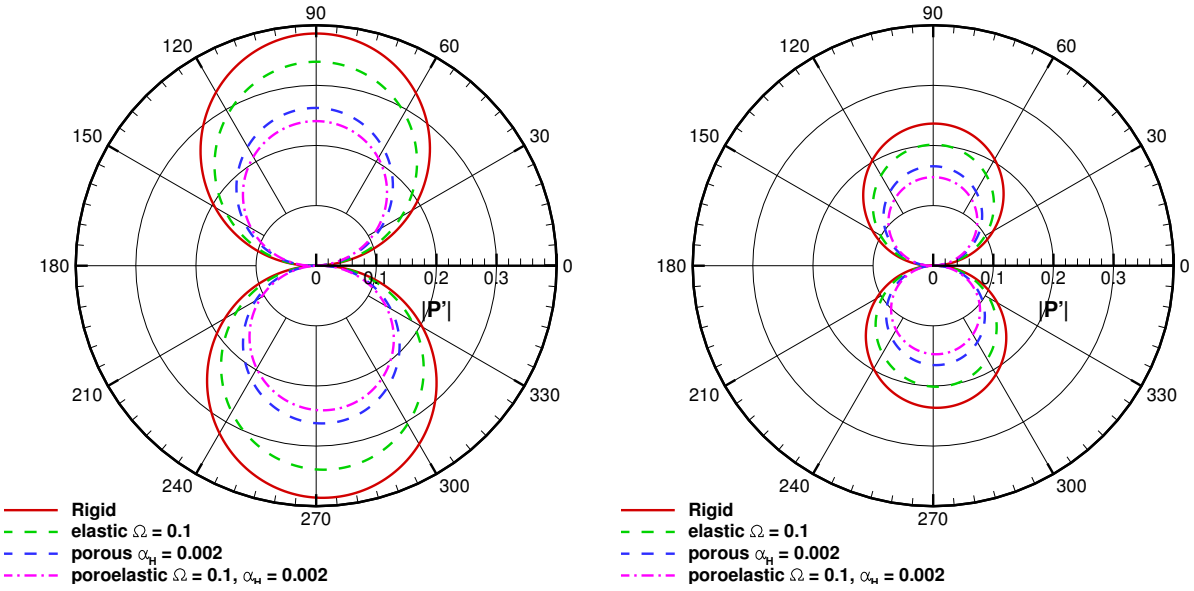

(a) Sweep angle of 0 deg.

(b) Sweep angle of 45 deg.

Figure 4.6: Directivities for different plate configurations for $k_0 = 1$ due to a point quadrupole source placed at the plate trailing edge.

LE, respectively. For this case, the total pressure is mainly composed by the scattered component since the proximity of the quadrupole source to the plate edge provides an efficient scattered field proportional to $\frac{1}{r^3}$ where r is the distance from the source to the trailing edge. A comparison between rectangular and swept rigid plates shows that the scattered field is aligned with the trailing edge and, therefore, for the swept edge, the scattering is more efficient along a plane inclined of Λ to the x-axis. This effect leads to the noise reduction observed in the directivity plots and it was already discussed by Ffowcs Williams and Hall (1970).

In Figs. 4.7 (b) and (e), one can see a comparison in terms of the total acoustic pressure for the poro-elastic plates with and without sweep. For both cases, the elasticity effect excites vibration modes at specific frequencies which can be visualized in Figs. 4.7 (c) and (f). The plate vibrations modify the scattered field inducing further surface pressure fluctuations which provide a destructive interference effect on the far-field radiated noise.

From the previous discussion, one should expect more expressive noise reductions from elasticity at higher Helmholtz numbers. Figure 4.8 presents directivity plots for different plate configurations for $k_0 = 10$ due to a point quadrupole source placed at the plate trailing edge. The effects of the sweep angle, porosity and elasticity are individually assessed considering $\Omega = 0.1$, $\alpha_H = 0.002$ and $R = 0.001$. Porosity shows a lower noise reduction in the current setup while the elasticity and trailing-edge sweep have a major role in the far-field noise reduction, both being more pronounced for the current

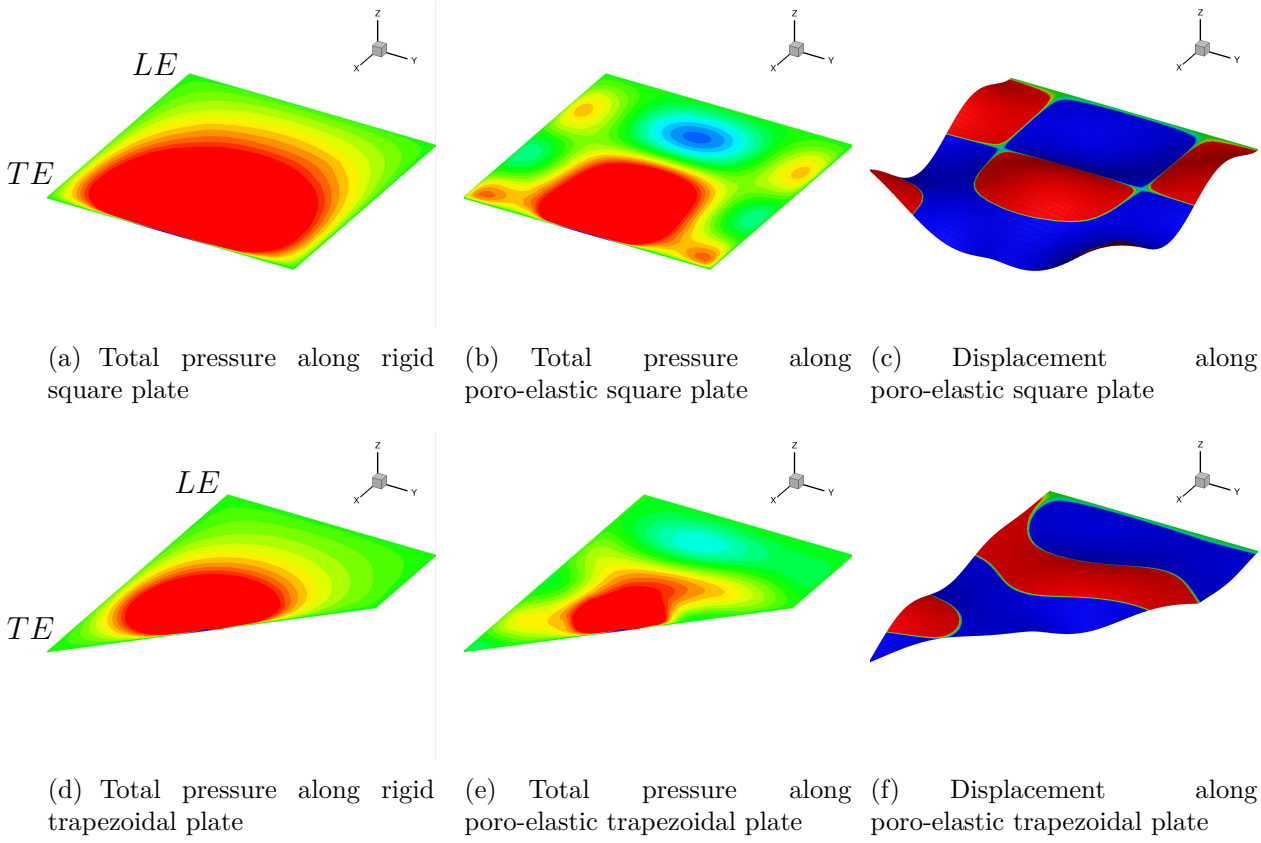

(a) Total pressure along rigid square plate

(b) Total pressure along poro-elastic square plate

(c) Displacement along poro-elastic square plate

(d) Total pressure along rigid trapezoidal plate

(e) Total pressure along poro-elastic trapezoidal plate

(f) Displacement along poro-elastic trapezoidal plate

Figure 4.7: Total acoustic pressure and plate displacement for different plate configurations for $k_0 = 1$ due to a point quadrupole source placed at the plate trailing edge.

high frequency scattering problem than for the previous low frequency case. While the increase in trailing-edge sweep reduces noise equally along all observer positions, elasticity leads to a more efficient noise reduction in the upstream lobe direction.

Figure 4.9 presents the total acoustic pressure and displacement for different plate configurations for $k_0 = 10$ due to a point quadrupole source placed at the plate trailing edge. The poro-elastic plate has the same parameters as before. For this case, the plate behaves as a non-compact source and, hence, one can see that the acoustic waves have a shorter wavelength compared to the plate chord. From the total acoustic pressure, it is possible to observe that the waves suffer diffraction along the leading and lateral edges of the plate. This effect is more pronounced for the swept trailing edge since it breaks the symmetry of the acoustic signature on the plate surface. The poro-elastic plates show a relatively similar acoustic pattern on their surfaces compared to the rigid ones. However, high frequency elastic waves propagate along the plate, leading to a cancellation effect of the total acoustic field. For example, one can see that at the leading edge, the poro-elastic plates show reduced acoustic pressure levels compared to the rigid ones. Moreover, for the swept trailing edge, the poro-elastic plate seems to provide an even more pronounced

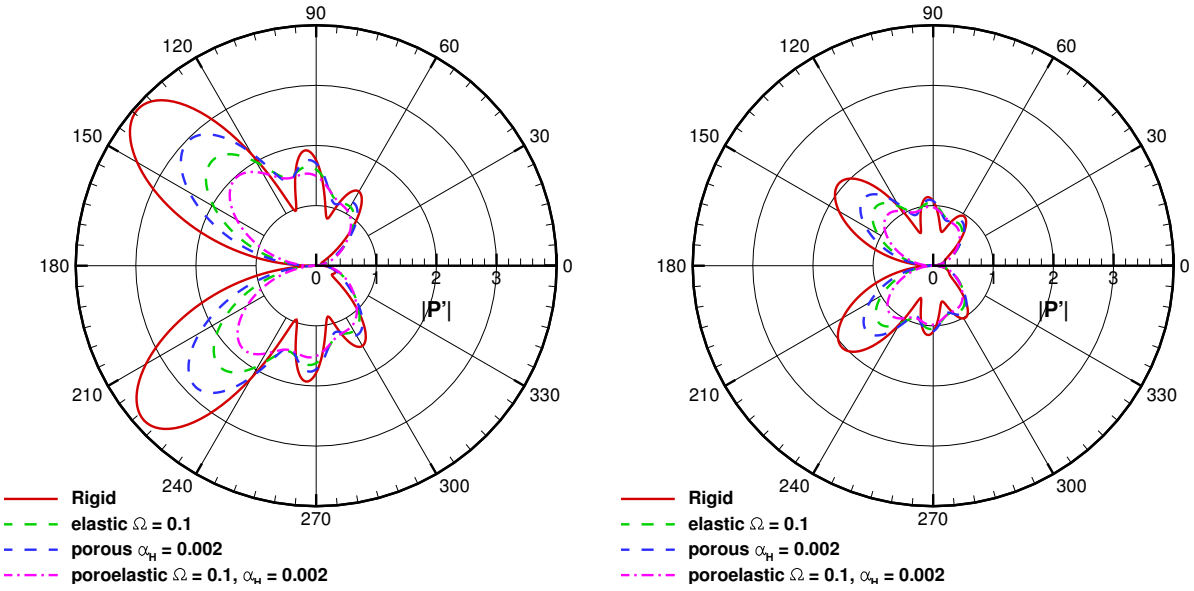

(a) Sweep angle of 0 deg.

(b) Sweep angle of 45 deg.

Figure 4.8: Directivities for different plate configurations for $k_0 = 10$ due to a point quadrupole source placed at the plate trailing edge.

reduction of the acoustic pressure levels along the plate surface as can be visualized in the proximity of the leading edge. One should remind that the modal basis for this case is non-symmetric and this may affect the propagation of elastic waves and, hence, the overall acoustic scattering mechanism. The displacement along the poro-elastic plates obtained using the current modal bases can be seen in Figs. 4.9 (c) and (f).

The results presented so far show directivity plots computed for observers positioned in a plane at the mid-span of the plates. In order to assess the overall noise reduction of the poro-elastic plates, Fig. 4.10 presents the integrated sound power level, PWL, computed over a spherical surface at a radial distance of 50 L from the trailing edge. The current results are calculated using the PWL of the rigid square plate as reference: $\Delta\text{PWL} = 10\log_{10}(\Pi/\Pi_0)$. Here, Π is the acoustic power radiated by the plate under analysis and Π_0 is the acoustic power radiated by the rigid-impermeable square plate. Hence, the values shown in the figure show the reduction in the PWL compared to the rigid plate. The Helmholtz numbers k_0 vary from 1 to 10 and it is possible to see the influence of porosity and elasticity for a broad range of frequencies, from acoustically compact to non-compact plates.

Figure 4.10 shows that the total sound power level is reduced when porosity and elasticity are applied when compared to the rigid-impermeable square plate. Figure 4.10(a) shows that, for lower Helmholtz numbers, the effects of porosity are more pronounced than those from elasticity. On the other hand, as the frequency increases, the effects of elasticity become more prominent, surpassing those of porosity. The poro-elastic

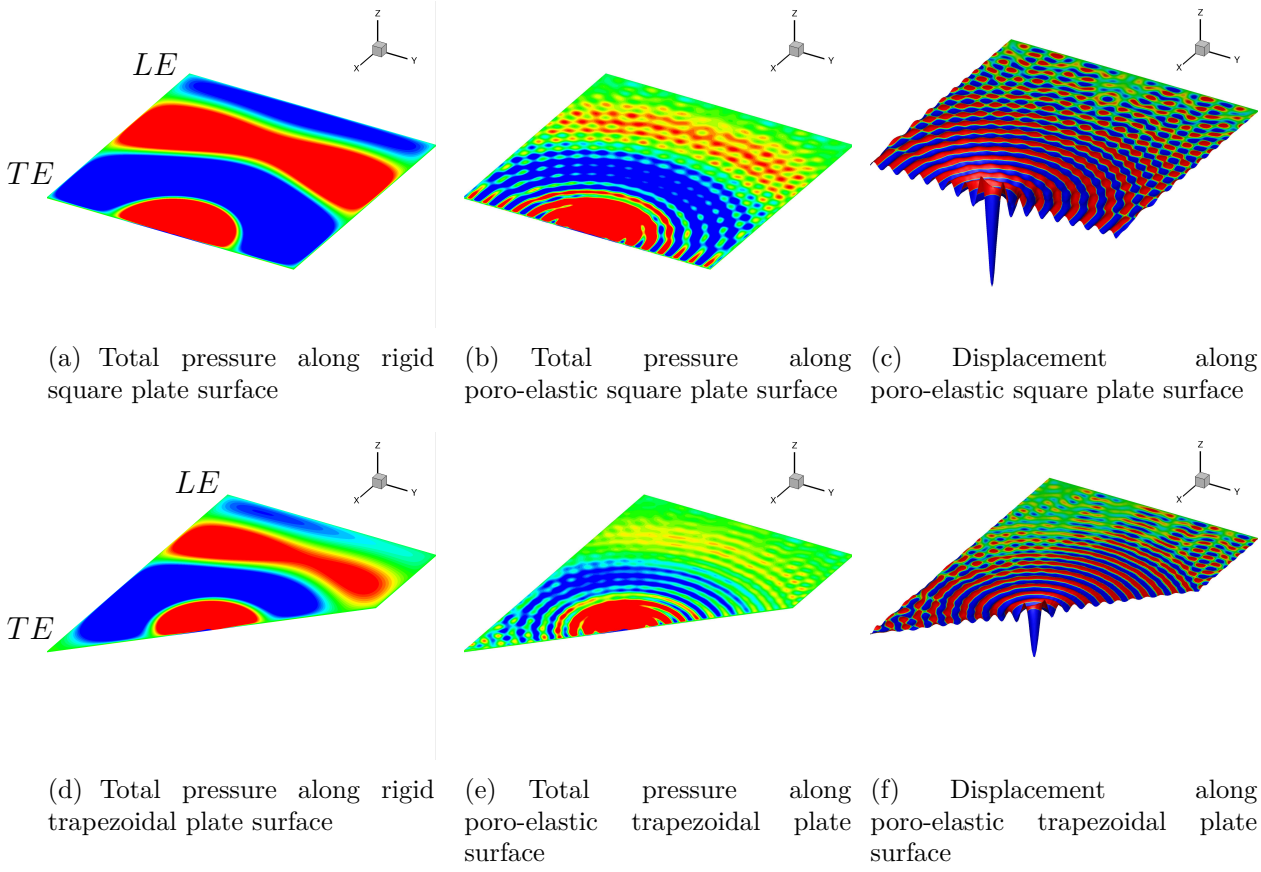

(a) Total pressure along rigid square plate surface

(b) Total pressure along poro-elastic square plate surface

(c) Displacement along poro-elastic square plate surface

(d) Total pressure along rigid trapezoidal plate surface

(e) Total pressure along poro-elastic trapezoidal plate surface

(f) Displacement along poro-elastic trapezoidal plate surface

Figure 4.9: Total acoustic pressure and plate displacement for different plate configurations for $k_0 = 10$ due to a point quadrupole source placed at the plate trailing edge.

plate combines both properties, leading to a further reduction in the sound power level at all frequencies. Figure 4.10(b) presents the results for a poro-elastic plate with a swept trailing edge. The sweep angle is set as 45 deg. and, for this case, one can also see the reduction in PWL for the trapezoidal rigid-impermeable plate compared to the square plate. Porosity and elasticity have similar effects for the trapezoidal plate and when both features are included, noise reduction is further increased.

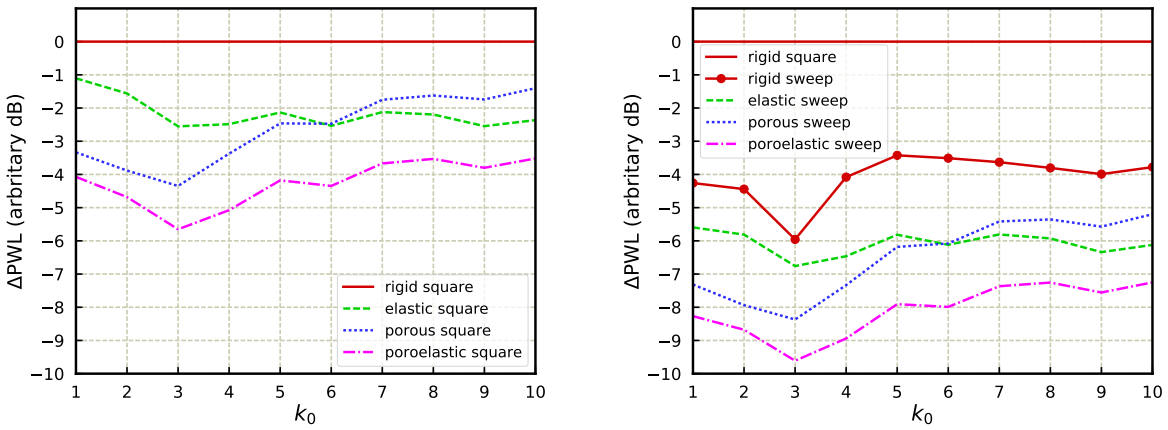

(a) Sound power level for square plate.

(b) Sound power level for swept trailing edge.

Figure 4.10: Effects of trailing-edge sweep angle, porosity and elasticity on sound power level reduction, ΔPWL, for different plates.

The acoustic pressure field in the mid-plane is shown in Fig.4.11 along the chordwise direction for square and trapezoidal rigid plates for $k_0 = 10$. The trapezoidal plate has a sweep angle of 45 deg. Both figures use the same levels of color contours and one can observe the reduction in noise scattering for Fig. 4.11(b) due to the sweep at the trailing edge when compared to the square plate in Fig. 4.11(a). In this case, the intensity of the acoustic waves propagating to the far-field for the square plate is more pronounced then for the trapezoidal plate, as demonstrated above.

Poro-elasticity reduces significantly the noise scattered by the plates as shown in Fig. 4.12. A comparison between Figs.4.11(a) and 4.12(a) show that the radiation pattern is also modified by porosity and elasticity. The combination of these two features and trailing-edge sweep, as presented in Fig. 4.12(b), leads to a considerable reduction in the acoustic field compared to that of the poro-elastic square plate in Fig. 4.12(a). For the trapezoidal poro-elastic plate, no upstream sound radiation is observed, differently from the trapezoidal rigid plate. In the former case, the radiation pattern is similar to that from a compact dipole source.

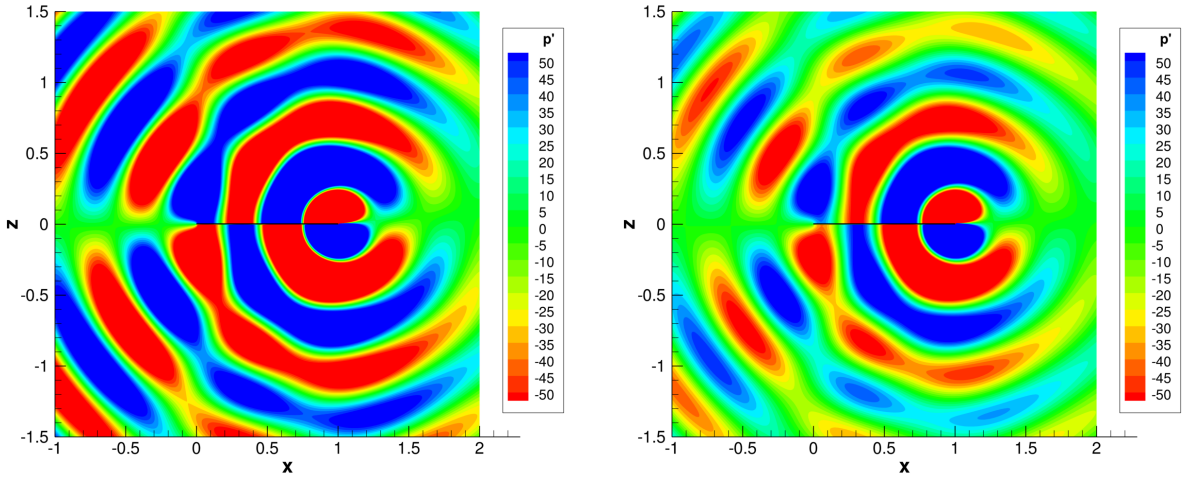

(a) Square rigid plate.

(b) Trapezoidal rigid plate.

Figure 4.11: Acoustic pressure field plotted in the mid-plane of square and trapezoidal ($\Lambda = 45$ deg.) rigid plates in air.

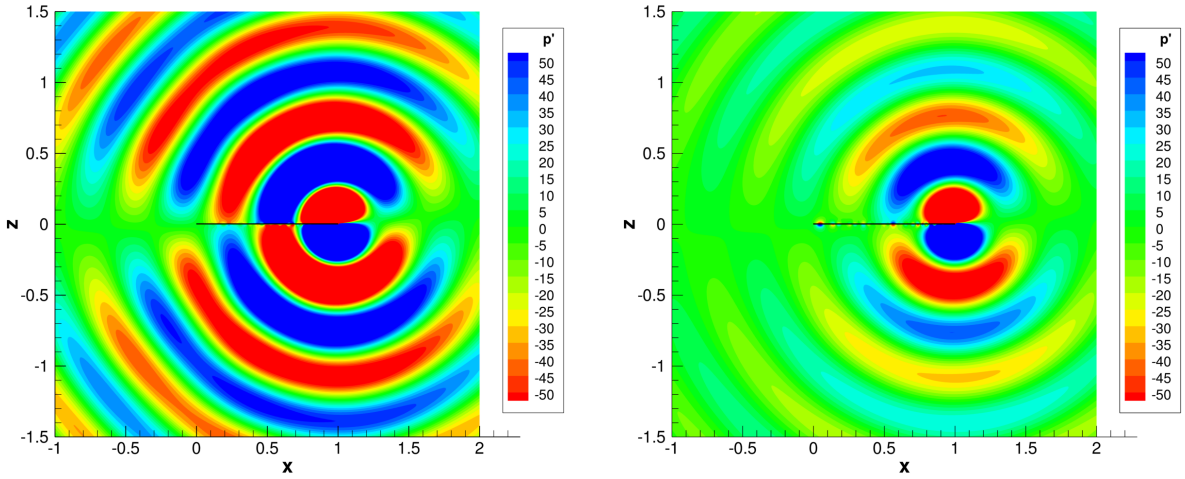

(a) Square poro-elastic plate.

(b) Trapezoidal poro-elastic plate.

Figure 4.12: Acoustic pressure field plotted in the mid-plane of square and trapezoidal ($\Lambda = 45$ deg.) poro-elastic plates in air.

4.4 Turbulent Jet Wavepacket Source

The scattering of turbulent jet wavepackets has been recently studied by Cavalieri *et. al* (2014a) for rectangular rigid plates and by Piantanida *et. al* (2016) for rigid plates with swept trailing edges. In the current work, we employ the proposed fast numerical methodology to investigate the effects of jet-plate interaction for poro-elastic plates with

swept trailing edges. This problem is representative of a jet installed under a wing. It is shown in Cavalieri *et. al* (2014a); Piantanida *et. al* (2016); Faranosov *et. al* (2017) that, at lower Strouhal numbers, jet-installation may lead to important trailing-edge diffraction mechanisms that increase the noise levels for observers perpendicular to the jet axis.

The wavepacket model presented by Cavalieri *et. al* (2012) is employed here to represent a non-compact turbulent jet noise source. The source term in Eq. 3.3 is written as

$$\mathcal{S}_i = \int_V \frac{\partial^2 T_{11}(\vec{z}_s)}{\partial z_{s_1} \partial z_{s_1}} G(\vec{x}, \vec{z}_s) d\vec{z}_s. \tag{4.4}$$

In the equation above, T_{ij} represents the i, j component of the Lighthill stress term. The volume integration is performed along a cylindrical volume for which the source intensity is non-negligible. More details of the wavepacket source model can be found in Cavalieri *et. al* (2012). This source was successfully employed in jet noise installation problems in Cavalieri *et. al* (2014a); Piantanida *et. al* (2016).

Here, the jet is placed one jet diameter D under the plate, pointing in the negative x-axis direction. The square plate has dimensions of $9D$ in chord and span, and the plate with a swept trailing edge has mean chord of $9D$ and sweep angle of 45 deg. The Helmholtz number based on the mean chord is $He = \tilde{k_0}\,\tilde{L} = k_0 = 6.8$. Figure 4.13 presents acoustic pressure directivities computed for impermeable-rigid, porous-rigid, impermeable-elastic and poro-elastic plates positioned above the turbulent jet source. Observers are placed $50D$ from the plate trailing edge along the jet axis. In Fig. 4.13 (a), one can see the directivities computed for the square plate. The jet points towards $\theta = 180$ deg. in this figure and the noise radiation has two distinct contributions. The main lobe radiation is due to the incident jet noise and it is slightly shifted upwards due to jet-trailing-edge diffraction. The secondary lobes are mainly due to the trailing-edge noise but they also depend on the distances from leading and lateral edges.

For the present analysis, both porosity and elasticity reduce the magnitudes of the secondary lobes due to trailing-edge scattering. Their combined effects lead to a further noise reduction in the side lobes. In Fig. 4.13 (b), results are presented for a plate with the swept trailing edge. This figure shows that the trailing-edge sweep is very efficient in reducing the scattered noise along the jet axis. In fact, Piantanida *et. al* (2016) demonstrate that a reduction in the overall acoustic efficiency of the scattering mechanism occurs for the swept trailing edge, for rigid-impermeable plates. In this case, the poro-elastic trapezoidal plate provides further noise reduction.

Figure 4.14 presents the total acoustic pressure along the top surfaces of the plates analyzed. While the bottom surfaces have the combined effects of incident and scattered pressure, the top surfaces show mainly the scattered pressure. A comparison between Figs. 4.14 (a) and (d) show that the scattered field for the swept rigid plate is redirected

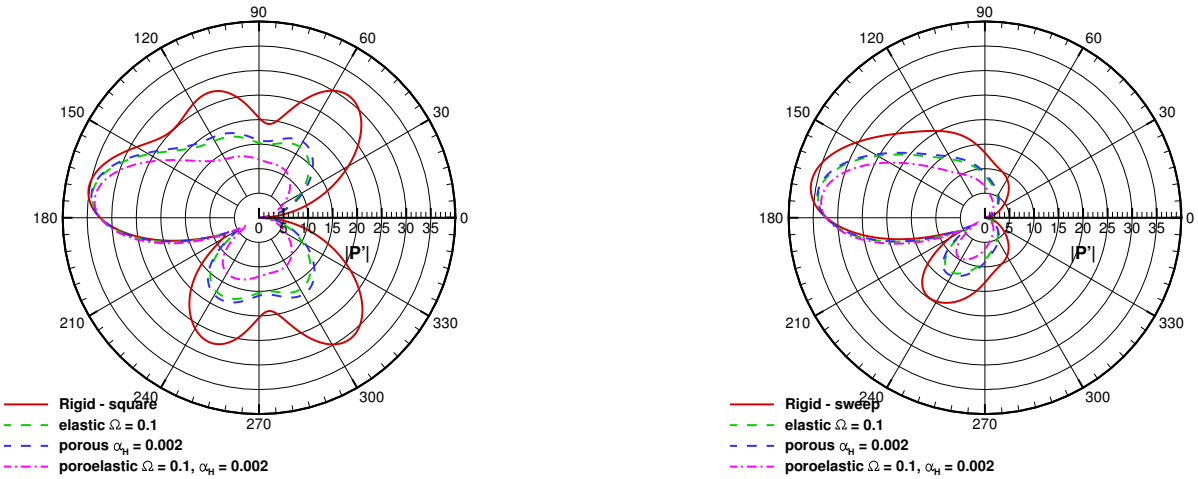

(a) $\Lambda = 0$ deg. (b) $\Lambda = 45$ deg.

Figure 4.13: Directivities computed for observers positioned along the jet axis for plate configurations with $\Lambda = 0$ and 45 degs. due to a turbulent jet wavepacket source placed in the proximity of the plate trailing edge. The parameters of the porous and elastic plates are $\Omega = 0.1$, $\alpha_H = 0.002$ and $R = 0.001$.

to the negative y-axis due to the sweep angle. The same effect is not observed in a comparison between Figs. 4.14 (b) and (e) for the poro-elastic plates. In this latter case, the acoustic waves along the top surface of the swept poro-elastic plate are still aligned with the x-axis, similarly to the square plate. This effect is associated with the plate displacement shown in Figs. 4.14 (d) and (f) and which occurs along the x-axis due to the incident jet source.

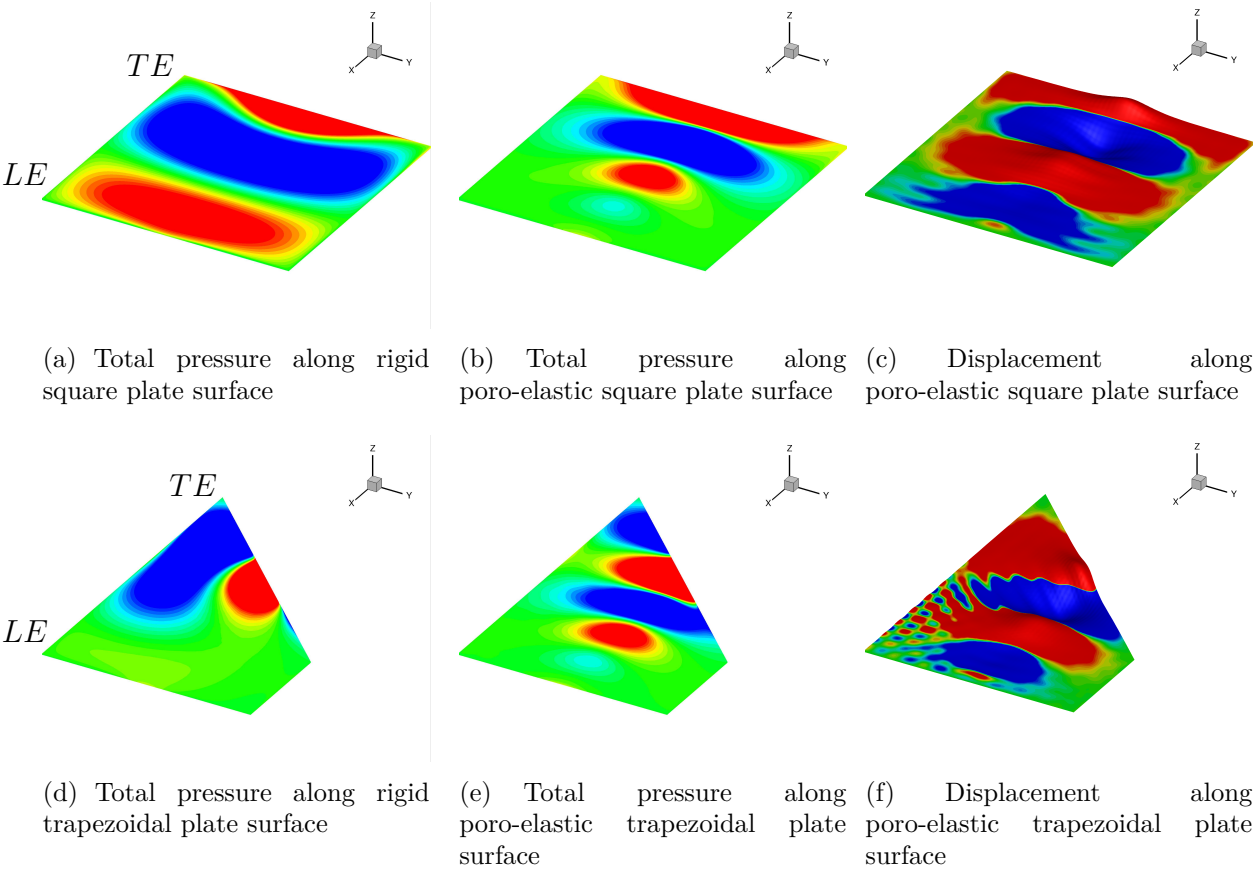

(a) Total pressure along rigid square plate surface

(b) Total pressure along poro-elastic square plate surface

(c) Displacement along poro-elastic square plate surface

(d) Total pressure along rigid trapezoidal plate surface

(e) Total pressure along poro-elastic trapezoidal plate surface

(f) Displacement along poro-elastic trapezoidal plate surface

Figure 4.14: Total acoustic pressure and plate displacement along top surfaces of rigid and poro-elastic plates placed in the proximity of a turbulent jet wavepacket. The parameters of the poro-elastic plate are $\Omega = 0.1$, $\alpha_H = 0.002$ and $R = 0.001$.

Directivities computed at observer locations positioned in a plane traverse to the jet axis, $50D$ from the trailing edge, can be seen in Fig. 4.15. For the square plate, the radiation is dipolar and elasticity causes a reduction in the magnitude of the far-field radiation. On the other hand, the swept trailing edge modifies the radiation since the scattered field is redirected towards the traverse plane as observed in Fig. 4.14(a). For this case, poro-elasticity leads to a further reduction in the scattered acoustic field as shown in Fig. 4.15 (b).

4.5 Validation of the Numerical Framework

In this section, a validation of the current numerical framework is presented. Results are shown in terms of directivity plots computed for the acoustic scattering by quadrupole sources in the proximity of the trailing edge of two- and three-dimensional plates. The former have a finite chord and infinite span while the latter are rectangular, having finite chord and span. The validation is performed for impermeable-rigid, impermeable-elastic,

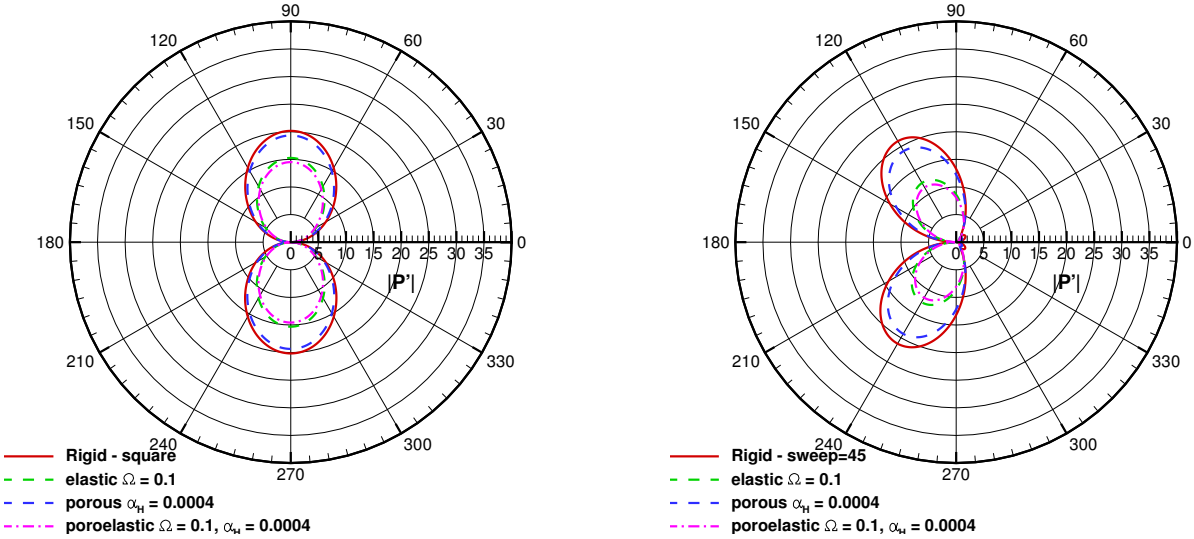

(a) $\Lambda = 0$ deg. (b) $\Lambda = 45$ deg.

Figure 4.15: Directivities computed for observers positioned perpendicularly to the jet axis for plate configurations with $\Lambda = 0$ and 45 degs. due to a turbulent jet wavepacket source placed in the proximity of the plate trailing edge. The parameters of the porous and elastic plates are $\Omega = 0.1$, $\alpha = 0.0004$ and $R = 0.001$.

porous-rigid and poro-elastic plate configurations. The solutions of the two-dimensional scattering problem is obtained by the method discussed by Cavalieri *et. al* (2016). For both cases, lateral quadrupole sources computed by Eqs. 4.5 and 4.3 for the 2D and 3D configurations, respectively, are placed at $(x, z) = (1, 0.005)$ and $(x, y, z) = (1, 0, 0.005)$. The directivity plots are computed for observers positioned 50 chords from the trailing edge (at the mid span of the plate for the 3D case) for aluminum plates submerged in water ($\epsilon = 0.135$). We choose to immerse the plates in water to test the methodology in more extreme conditions, at larger values of the fluid loading parameter ϵ.

When properly scaled, it is expected that the three-dimensional far-field solutions converge to the two-dimensional solutions for plates of large aspect ratios. In order to compare both solutions, we employ the scaling analysis of Jaworski and Peake (2013) for the 3D case and that presented by Cavalieri *et. al* (2016) for the 2D plate. For all comparisons, the Helmholtz number is set as $k_0 = 20$. Jaworski and Peake (2013) applied the reciprocity theorem to calculate the acoustic scattering by a point quadrupole in the vicinity of a trailing edge. Hence, they solved for the acoustic near-field at the trailing edge subject to an incident spherical wave coming from the far-field. In order to perform a similar analysis for the 2D case, Cavalieri *et. al* (2016) specified the incident field as a cylindrical wave emitted from a far-field position employing the asymptotic form of the Hänkel function for large arguments.

To compare the solutions obtained by the 2D and 3D plates at the far-field

observer positions, the magnitudes of the 2D and 3D acoustic pressures are multiplied by $4\pi r^{3/2}\sqrt{r_0}/\cos(3\theta/2)$ and $\sqrt{32}\pi^{3/2}r^{3/2}r_0/\left(\sqrt{k_0}\cos(3\theta/2)\right)$, respectively. This scaling allows a comparison to the rigid limit as discussed by Jaworski and Peake (2013); Cavalieri *et. al* (2016). In the previous equations, θ is the angle measured from the axis positioned along the plate chord to the source position, in the counterclockwise direction. The terms r and r_0 refer to the source and observer distances to the trailing edge. Here, $\theta = \pi/2$, $r = 0.005$ and $r_0 = 50$.

Figure 4.16(a) presents a comparison of the directivity plots for rigid-impermeable plates. The solutions obtained for 3D plates of aspect ratios 1, 2, 4 and 8 are compared to that of the plate with an infinite span (2D case). The solutions obtained by the plates with aspect ratios 4 and 8 show excellent agreement with the 2D case when the scaling is employed. On the other hand, clear differences can be observed for the directivity plot computed for the square plate due to diffraction effects on the lateral edges.

The solutions for elastic, porous and poro-elastic plates are shown in Figs. 4.16(b–d). In these figures, the 2D case is compared to plates of aspect ratios 1 and 8. For the elastic-impermeable case (Fig. 4.16(b)), one can see that the solution computed for the square plate is considerably different than that presented for the 2D plate. In this case, the 3D plate generates higher noise levels than the case with infinite span. The rectangular plate with aspect ratio 8 shows a good agreement with the plate of infinite span. A perfect agreement is not expected since the elastic waves propagate along the chordwise and spanwise directions in the 3D modal basis while they only propagate along the chordwise direction for the 2D configuration. The solutions obtained for the porous-rigid plate (Fig. 4.16(c)) shows an excellent agreement with the 2D case for both 3D plates (although not shown, the agreement for the square plate deteriorates for lower porosities). This suggests that an increase in the porosity parameters reduces the effects of scattering on the lateral edges. Finally, the poro-elastic case is depicted in (Fig. 4.16(d)) and the plate with large aspect ratio shows a good agreement with the 2D case. Here, the 3D configuration presents a more pronounced noise reduction compared to the 2D poro-elastic plate.

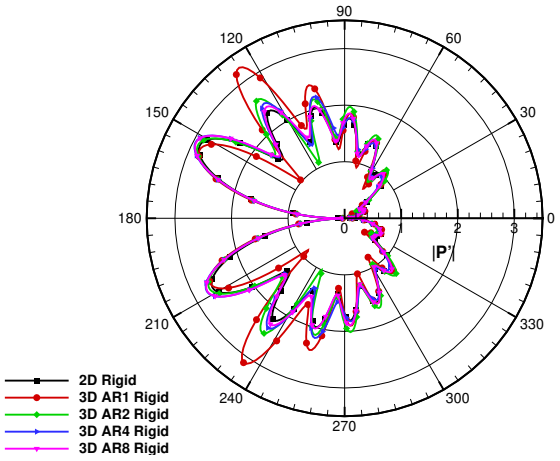

(a) Directivities of impermeable-rigid plates 2D and 3D

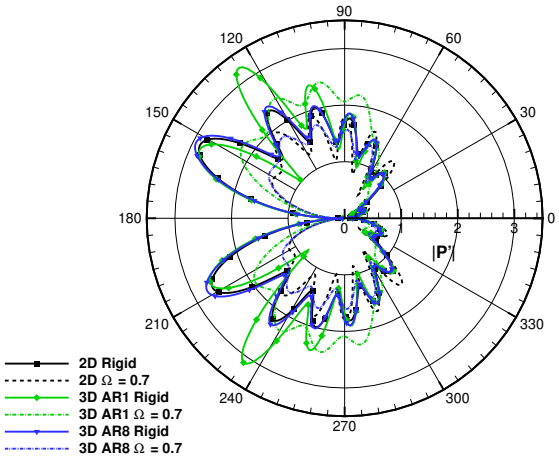

(b) Directivities of impermeable-elastic plates 2D and 3D

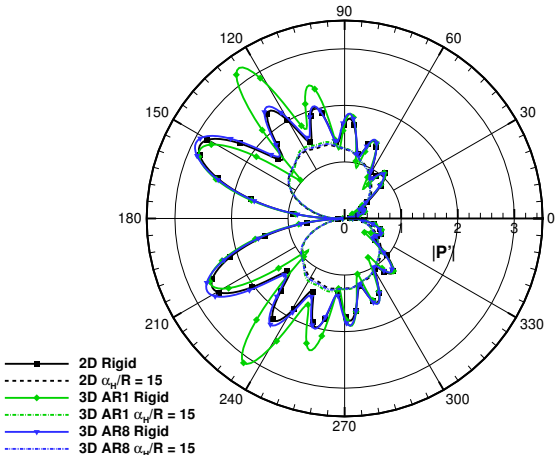

(c) Directivities of perfurated-rigid plates 2D and 3D

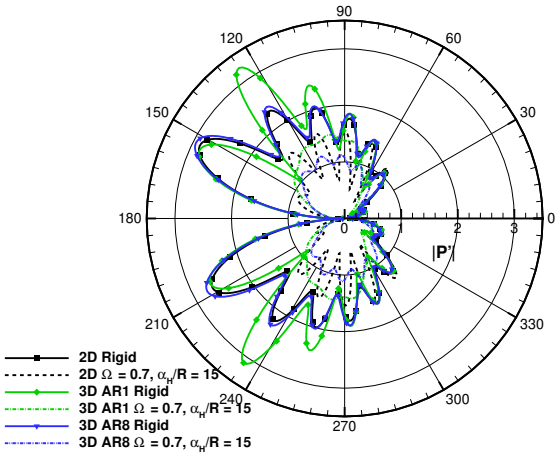

(d) Directivities of poro-elastic plates 2D and 3D

Figure 4.16: Directivities obtained by the 2D and 3D plates at the far-field observer positions for impermeable-rigid, impermeable-elastic, perfurated-rigid and poro-elastic plates.

4.6 Serrated Trailing Edges

In this section, the fast numerical framework is employed to compute the acoustic scattering by plates with serrations. The topic of noise reduction from trailing-edge serrations has been recently studied by several authors using analytical methods, numerical simulations and wind tunnel experiments (Howe, 1991; Jones and Sandberg, 2012; Karimi *et. al*, 2017; León *et. al*, 2017). The presence of trailing-edge scattering of spanwise-aligned highly correlated aeroacoustic sources is discussed by Abreu *et. al* (2017); Ribeiro and Wolf (2017). Here, in order to model a spanwise correlated acoustic

source, a two-dimensional quadrupole with unit intensity is placed in the proximity of the trailing edge of the plate, at $(x, z) = (L, 0.01)$. The two-dimensional source is given by

$$\mathcal{S}_i = \frac{\partial^2 G_{2D}(\vec{x}, \vec{z}_s)}{\partial z_{s_1} \partial z_{s_3}} = \frac{i\, k_0}{8}(x_1 - z_{s_1})(x_3 - z_{s_3}) \left\{ \frac{2H_1^{(1)}(k_0\, r)}{r^3} - \frac{k_0 \left[H_0^{(1)}(k_0\, r) - H_2^{(1)}(k_0\, r) \right]}{r^2} \right\}, \tag{4.5}$$

where $r = \sqrt{(x_1 - z_{s_1})^2 + (x_3 - z_{s_3})^2}$, and $G_{2D}(\vec{x}, \vec{z}_s) = {}^{i}/_{4} H_0^{(1)}(k_0\, r)$. In the equations above, $H_n^{(1)}$ stands for the Hankel function of the first kind and order n.

Figure 4.17(a) shows the geometries analyzed which consist of square plates with unitary chord L clamped along the y axis. We use the same notation as in Howe (1991) and the sawtooth serrations extend from the free trailing edge of the plate by a length of $2h$. Here, h is the half distance from the root to tip of the serrations. The wavelengths of the serrations are $\lambda = 1.0h$ and $\lambda = 0.4h$.

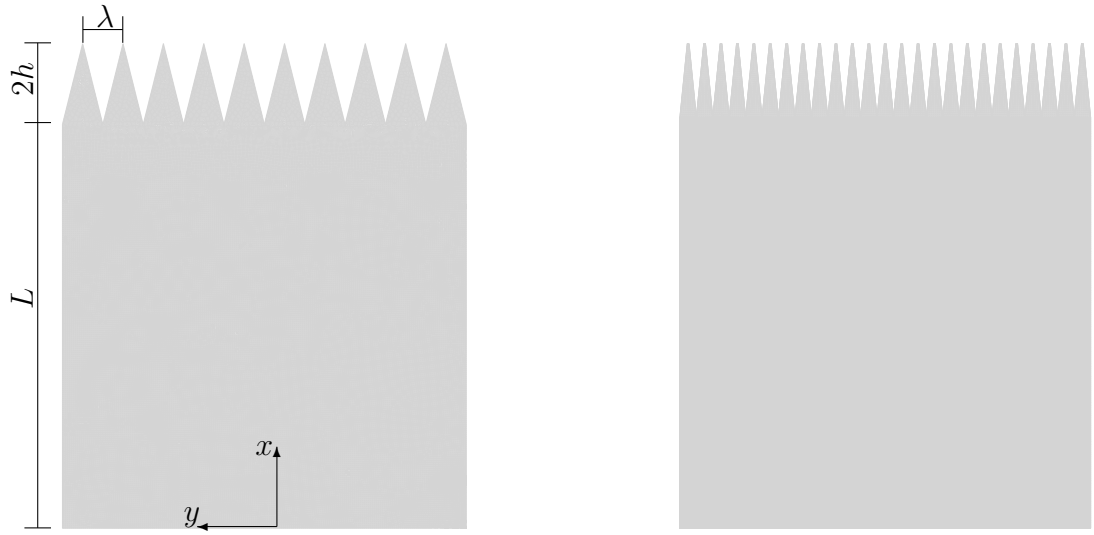

(a) Plate with wide trailing-edge serrations with $\lambda/h = 1.0$

(b) Plate with narrow trailing-edge serrations with $\lambda/h = 0.4$

Figure 4.17: Different configurations of plates with trailing-edge serrations analyzed.

In Fig. 4.18 the directivities computed for observers positioned $50L$ from the trailing edges are shown for rigid plates with and without serrations. In this figure, the wider serrations with $\lambda = 1.0h$ are employed and, for this simulation, the Helmholtz number is set as He$= k_0 = 5$. In order to resolve the bending wavelengths in the serrations, the boundary element mesh has around 150000 quadrilateral elements. The serrated trailing edge leads to a considerable noise reduction compared to the case without serrations. These results demonstrate the advantage of employing rigid serrations for reducing the trailing-edge noise from coherent sources spanwise-aligned with the edge. The mechanism here is similar to that observed in the swept edges.

Figure 4.19 presents the directivities obtained for the different serrations. In these

figures, the porosity and elasticity parameters are $\Omega = 0.1$, $\alpha_H = 0.002$ and $R = 0.001$. The results are shown for the wider and narrow serrations in Figs 4.19(a) and (b), respectively. In these figures, the solutions are compared only to the rigid plate with serrations and, as one can see, additional noise reduction is obtained by the poro-elastic plates. It is interesting to notice that the wider serrations generate less noise the the far-field than the narrow ones for all plate configurations.

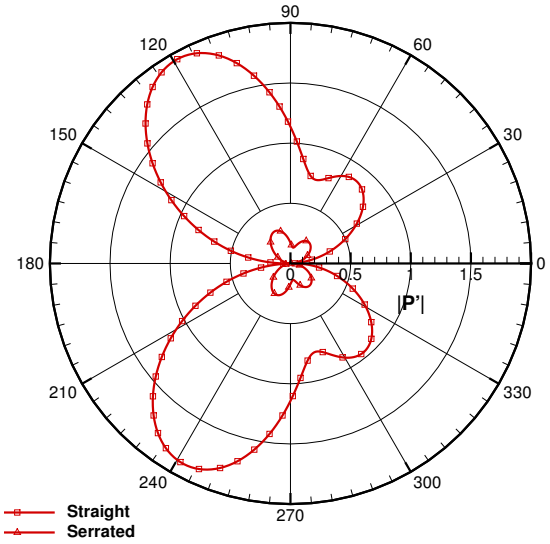

Figure 4.18: Acoustic scattering by a 2D quadrupole source placed in the proximity of the trailing edge of different rigid plates with and without serrations.

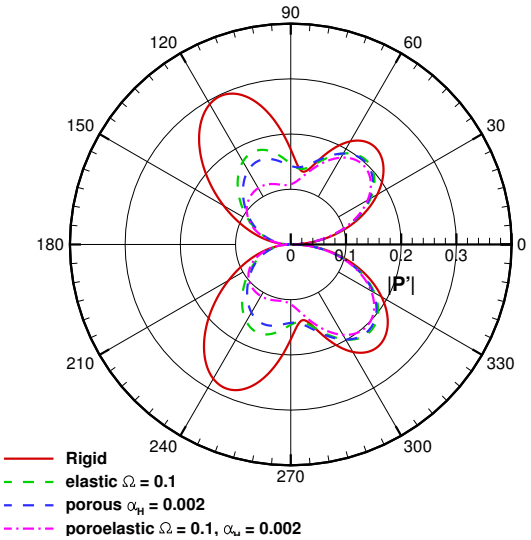

(a) Directivities of rigid, elastic, porous and poro-elastic plates with wide serrations, $\lambda/h = 1.0$.

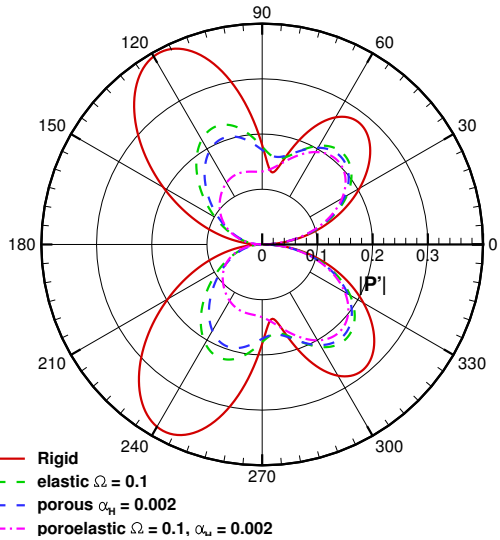

(b) Directivities of rigid, elastic, porous and poro-elastic plates with narrow serrations, $\lambda/h = 0.4$.

Figure 4.19: Acoustic scattering by a 2D quadrupole source placed in the proximity of different serrated trailing edges.

The total surface acoustic pressure is shown in Figs. 4.20(a) and (d) for the rigid plates with different serrations. In Figs. 4.20(b) and (e), the acoustic pressure is presented for the poro-elastic plates with wide and narrow serration extensions, respectively. The figures have the same contour levels and, compared to the rigid cases, the poro-elastic plates have modified acoustic signatures along their surfaces, with reduced pressure levels. One can see that the negative wave pulse (in blue color) reaching the leading edge of the plate is not present in the acoustic signature of the poro-elastic plates. Moreover, this negative wave is less pronounced for the rigid plate with narrow serrations. In Figs. 4.20(c) and (f), the plate displacements are presented for the poro-elastic plates showing the two-dimensional bending waves excited by the incident acoustic source. In these figures, it is possible to see that the serrations also vibrate in phase due to the two-dimensional acoustic excitation.

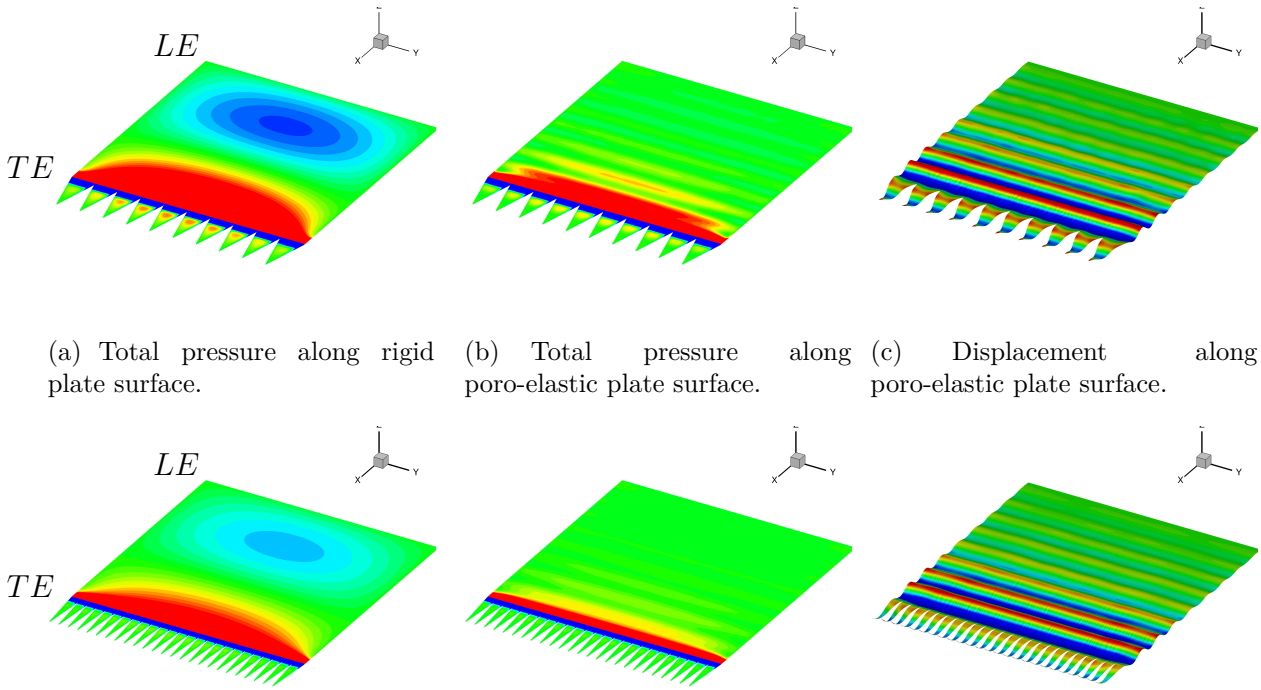

(a) Total pressure along rigid plate surface.

(b) Total pressure along poro-elastic plate surface.

(c) Displacement along poro-elastic plate surface.

(d) Total pressure along rigid plate surface.

(e) Total pressure along poro-elastic plate surface.

(f) Displacement along poro-elastic plate surface.

Figure 4.20: Acoustic scattering by a 2D quadrupole source placed in the proximity of the trailing edge of rigid and poro-elastic plates with different types of serrations. The parameters of the poro-elastic plate are $\Omega = 0.1$, $\alpha_H = 0.002$ and $R = 0.001$.

4.7 Description of Composite Materials

In this section, we present the details of the composite materials analyzed in the present investigation of acoustic scattering. Here, the plates will be either considered

rigid or elastic. The description of the problem is shown schematically in Fig. 4.21(a). A sound source S is placed in the vicinity of one of the edges of a finite composite plate of chord L, and we wish to determine the scattered sound at an arbitrary observer position. In the figure, the plate is clamped at the leading edge and the trailing edge and lateral edges are free to vibrate. The sound source can be compact or non-compact as before. The orientation of the principal direction of the laminae is given by the angle θ. Figure 4.21(b) shows a lateral view including the several layers of the symmetric laminate (with respect to the x-axis) of the composite plate with thickness h. Hence, the x-axis is positioned in the mid-plane of the plate.

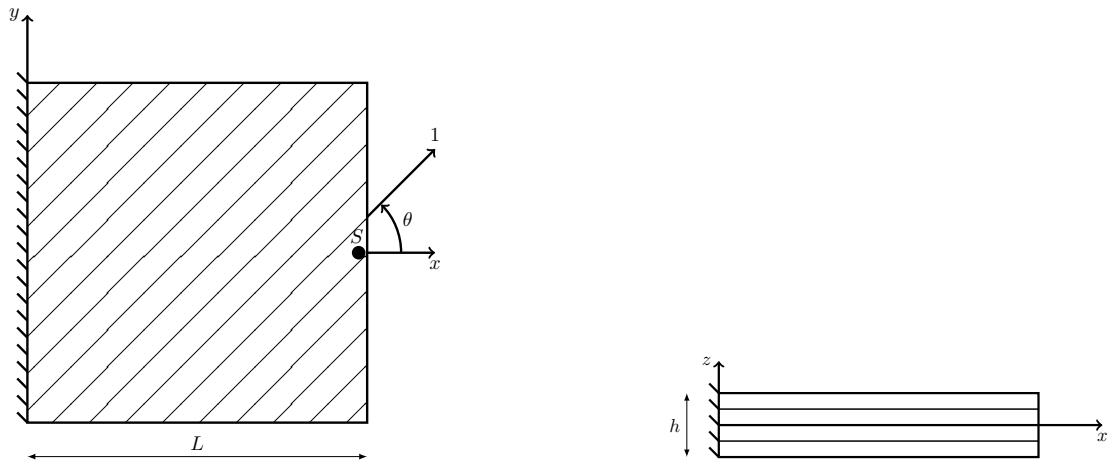

(a) Top view of the composite plate.

(b) Lateral view showing the several laminae.

Figure 4.21: Sketch of a sample rectangular plate with one clamped edge along the y axis and three free edges, subjected to an incident acoustic field from a source S.

The effects of composite plates will arise through the following fluid loading parameters: the vacuum bending wave Mach number Ω and the intrinsic fluid loading parameter ϵ, which depend on the plate specific mass $\tilde{m}$ and the bending stiffness $\tilde{D}_{11}$ in the chordwise direction. To satisfy the assumptions considered by the FMM-BEM code and the Classical Laminate Plate Theory (CLPT), the plate is required to have a small thickness. For laminated plates, the number of layers and the thicknesses of each layer will determine the total thickness of the plate. Unless otherwise stated, we have worked with a plate thickness h of 0.5% of its chord. For all cases analyzed, this thickness is much smaller than the acoustic wavelength and, therefore, the directivities obtained by the FMM-BEM are close to the expected results for plates of zero thickness (Crighton and Leppington, 1973).

The non-dimensional frequency parameter (β^2) for bending waves is defined as $\beta^2 = \tilde{\omega} L^2 (\tilde{m}/\tilde{D}_{11})^{1/2}$. In order to validate the procedure employed to obtain the modal bases, we compute the frequency parameter to compare with previous numerical and experimental

work by Narita and Leissa (1992) and Crawley (1979). Table 4.4 shows the material properties of graphite/epoxy (Hercules) used to validate results. Observe that the ratio

Material	$E_{11}(GPa)$	$E_{22}(GPa)$	$G_{12}(GPa)$	ν_{12}	E_{11}/E_{22}	$h(mm)$	$\rho_s(kg^3/m^3)$
Graphite/epoxy	128.0	11.0	4.48	0.25	11.6	0.13	1500

Table 4.4: Material properties employed to validate the procedure.

E_{11}/E_{22} is the degree of orthotropy of the material. Table 4.5 presents the frequency parameter for modes 1 to 5 obtained by a square plate for different stacking sequences and the results obtained by the FEM are compared to those from the literature (Narita and Leissa, 1992; Crawley, 1979), validating the current methodology for the vibration problem of cantilever laminated composite plates.

Mode	Narita and Leissa (1992)	Crawley (1979) FEM	Crawley (1979) Exp.	Present
Stacking Sequence $[0, 30°]_s$				
1	3.409	3.379	3.021	3.309
2	4.725	4.468	4.670	4.587
3	9.874	8.827	9.395	9.585
4	20.78	21.44	18.69	20.179
5	23.32	19.39	19.39	20.769
Stacking Sequence $[45°, -45°, -45°, 45°]_s$				
1	1.813	1.792	1.692	1.759
2	6.553	6.443	6.089	6.351
3	10.48	10.38	10.20	10.155
4	17.29	17.11	15.07	16.775
5	21.49	21.26	19.17	20.824

Table 4.5: Comparison of the non-dimensional frequency parameter β^2 for cantilever square plates.

The main differences between metallic and symmetric laminated plates will arise through the fluid pressure loading parameters (ϵ, Ω). We have chosen five samples of laminated plates to evaluate how these parameters vary in comparison with a sample aluminum plate, all of which are considered to be in air or submerged in water. Table 4.6 shows the arrangement of laminated plates composed of eight layers, symmetrically stacked about the mid plane of the plate. In this case, there is no coupling between bending and extension (Jones, 1998). The θ angles of the stacking sequence are measured with reference to the chordwise direction x as illustrated by Fig. 4.21(a). The three plates labelled as quasi-isotropic are chosen so as to have nearly isotropic extensional stiffness. However, their bending stiffness is not isotropic and have a maximum near the direction of the outermost layers. Accordingly, plate B has a maximum bending stiffness in the chordwise direction, whereas plate C has a minimum bending stiffness in that direction.

Laminate	Layer orientation (deg.)
Cross-ply	[0/90/0/90/90/0/90/0]
Cross-ply	[90/0/90/0/0/90/0/90]
Quasi-isotropic A	[45/-45/90/0/0/90/-45/45]
Quasi-isotropic B	[0/45/-45/90/90/-45/45/0]
Quasi-isotropic C	[90/45/-45/0/0/-45/45/90]

Table 4.6: Sample composite plates considered in this study.

The material specified for all laminated plates is taken to have a stronger and a weaker orthotropy, with mechanical properties in terms of ratio given as $E_{11}/E_{22} = 10$, $E_{11}/E_{22} = 2$, respectively. To understand the impact of the degree of orthotropy, two different materials are created and labelled as fabric 1 and fabric 2. Aluminum is considered for the study of the isotropic plates with the same thickness of the composite plates. Values for the mechanical properties and thicknesses of the plates are provided in Table 4.7.

Material	$E_{11}(GPa)$	$E_{22}(GPa)$	$G_{12}(GPa)$	ν_{12}	E_{11}/E_{22}	$h(mm)/layer$	$\rho_s(kg/m^3)$
Aluminum	72.0	72.0	–	0.34	1.0	5.0	2700
Fabric 1	100.0	50.0	30.0	0.25	2.0	0.5	1500
Fabric 2	100.0	10.0	6.0	0.25	10.0	0.5	1500

Table 4.7: Material properties employed in the current study.

Table 4.8 and 4.9 show the values of the coincidence frequency in the chordwise direction, the intrinsic fluid loading parameter ϵ, the vacuum bending wave Mach number $\Omega(w)$, the surface density $\tilde{m}$ for all cases studied when the plates are immersed in air, considering fabric 1 and 2. The lower specific mass of the composite plate increases the values of ϵ compared with aluminum. It is important to notice that ϵ is fixed for each plate and it is usually very small for thin plates. The influence of the fluid loading on the mechanical properties of the plate increases as Ω decreases. The fluid loading effects are significant for bending waves propagating subsonically $\Omega \ll 1$ (Howe, 1998).

Plate	Aluminum	$[0, 90, 0, 90]_s$	$[90, 0, 90, 0]_s$	A	B	C
$\tilde{D}_{11}$ (N·m)	434	464	361	389	485	330
$\tilde{m}$	10.8	6.0	6.0	6.0	6.0	6.0
ω_c (rad/s)	18554	13370	15161	14602	13079	15849
ϵ	0.0021	0.0051	0.0045	0.0047	0.0053	0.0043
$\Omega(k_0 = 1)$	0.1360	0.1602	0.1504	0.1533	0.1619	0.1471
$\Omega(k_0 = 5)$	0.3040	0.3581	0.3363	0.3427	0.3621	0.3289
$\Omega(k_0 = 10)$	0.4299	0.5065	0.4756	0.4847	0.5121	0.4652

Table 4.8: Bending stiffness and fluid loading parameters of sample plates for fabric 1 in air.

Plate	Aluminum	$[0,90,0,90]_s$	$[90,0,90,0]_s$	A	B	C
$\tilde{D}_{11}$ (N·m)	434	385	204	177	386	115
$\tilde{m}$	10.8	6.0	6.0	6.0	6.0	6.0
ω_c (rad/s)	18554	14672	20146	21644	14652	26861
ϵ	0.0021	0.0051	0.0034	0.0032	0.0047	0.0026
$\Omega(k_0 = 1)$	0.1360	0.1602	0.1305	0.1259	0.1530	0.1130
$\Omega(k_0 = 5)$	0.3040	0.3419	0.2918	0.2815	0.3421	0.2527
$\Omega(k_0 = 10)$	0.4299	0.4835	0.4126	0.3981	0.4838	0.3573

Table 4.9: Bending stiffness and fluid loading parameters of sample plates for fabric 2 in air.

For plates submerged in water the fluid pressure loading is heavy. Tables 4.10 and 4.11 show the values of the coincidence frequency in the chordwise direction, the intrinsic fluid loading parameter ϵ, the vacuum bending wave Mach number $\Omega(w)$, and the surface density $\tilde{m}$ for all cases studied for plates submerged in water considering fabric 1 and 2.

Plate	Aluminum	$[0,90,0,90]_s$	$[90,0,90,0]_s$	A	B	C
$\tilde{D}_{11}$ (N·m)	434	464	361	389	485	330
$\tilde{m}$	10.8	6.0	6.0	6.0	6.0	6.0
ω_c (rad/s)	347326	250289	283801	273344	244838	296686
ϵ	0.3948	0.9862	0.8698	0.9030	1.0082	0.8320
$\Omega(k_0 = 1)$	0.0654	0.0770	0.0723	0.0737	0.0779	0.0707
$\Omega(k_0 = 5)$	0.1462	0.1722	0.1617	0.1648	0.1741	0.1581
$\Omega(k_0 = 10)$	0.2067	0.2435	0.22287	0.2330	0.2462	0.2236

Table 4.10: Bending stiffness and fluid loading parameters of sample plates for fabric 1 in water.

Plate	Aluminum	$[0,90,0,90]_s$	$[90,0,90,0]_s$	A	B	C
$\tilde{D}_{11}$ (N·m)	434	385	204	177	386	115
$\tilde{m}$	10.8	6.0	6.0	6.0	6.0	6.0
ω_c (rad/s)	347326	274658	377118	105163	274285	502819
ϵ	0.3948	0.8987	0.6545	0.6092	0.8999	0.4909
$\Omega(k_0 = 1)$	0.0654	0.0735	0.0627	0.0605	0.0736	0.0543
$\Omega(k_0 = 5)$	0.1462	0.1644	0.1403	0.1353	0.1645	0.1215
$\Omega(k_0 = 10)$	0.2067	0.2324	0.1984	0.1914	0.2326	0.1718

Table 4.11: Bending stiffness and fluid loading parameters of sample plates for fabric 2 in water.

4.8 High Aspect Ratio Plates

In the current section, we investigate plates of high aspect ratios which can find application in helicopter rotors and aircraft wings. The plate with high aspect ratio

at hand is shown schematically in Fig. 4.22. The plate has an aspect ratio $AR = 8$ and is clamped along the x-axis at $y = -4$, simulating a wing root. A point quadrupole sound source $\mathcal{S}$ is placed at $x, y, z = (1, 4, 0.01)$ and we wish to determine the scattered sound at a given observer position r relative to the mid-span plane (xz-axis). Figure 4.22 illustrates a plate with one unit of chord and eight chords in the span direction, with one clamped edge and three free lateral edges. The coordinate system is located at $x, y, z = (0, 0, 0)$. The idea here is to investigate the fundamental mechanics of noise scattering considering different material configurations due to a source placed at the trailing-edge tip. Therefore, the point quadrupole source could represent the wing-tip vortex.

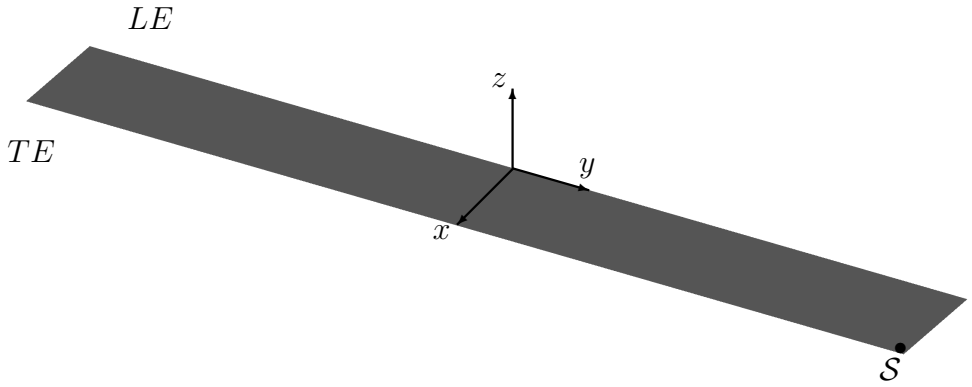

Figure 4.22: High aspect ratio plate analyzed (AR=8).

Figure 4.23 presents directivity plots for plates with aluminum and symmetric laminate cross-ply configurations ($[0/90]_s$) with fabric 1 and 2. A high-frequency problem is set considering $k_0 = 10$. Firstly, the effects of porosity and elasticity are individually assessed in Fig. 4.23(a) for the aluminum plate considering $\Omega = 0.1$, $\epsilon = 0.0021$, $\alpha_H = 0.004$ and $R = 0.001$. As one can see, for this case where the high aspect ratio plate is excited at the tip, the elasticity does not play a significant role in terms of reduction of noise scattering. The directivity is altered compared to that of the rigid plate, changing the directions of the main lobes. However, the magnitudes of the directivities are similar. Porosity shows a minor reduction in the scattered pressure, without changing the radiation pattern. The combined effects of poro-elasticity lead to improved results, although not as intense as for the previous analyses. Since the source is placed on the end of the plate, it excites mostly low frequencies of the structure along the y-axis, as Fig. 4.24 shows below. Furthermore, for the current aluminum plate, the fluid loading parameter leads to a weak fluid-structure interaction.

For the current study, the thickness of the plates is fixed in $0.004\tilde{L}$ and the fluid loading parameters are computed for each plate as shown in Tables 4.8 - 4.9. As one can see in Fig. 4.23(b), the fluid loading parameters for the composite plates are higher than for the aluminum plate. For the simulations of these plates, we had to increase the

imaginary component of Ω to avoid singularities at resonances. For all cases analyzed, this component was chosen equal to 5% of the real value of Ω. Figure 4.23(b) shows

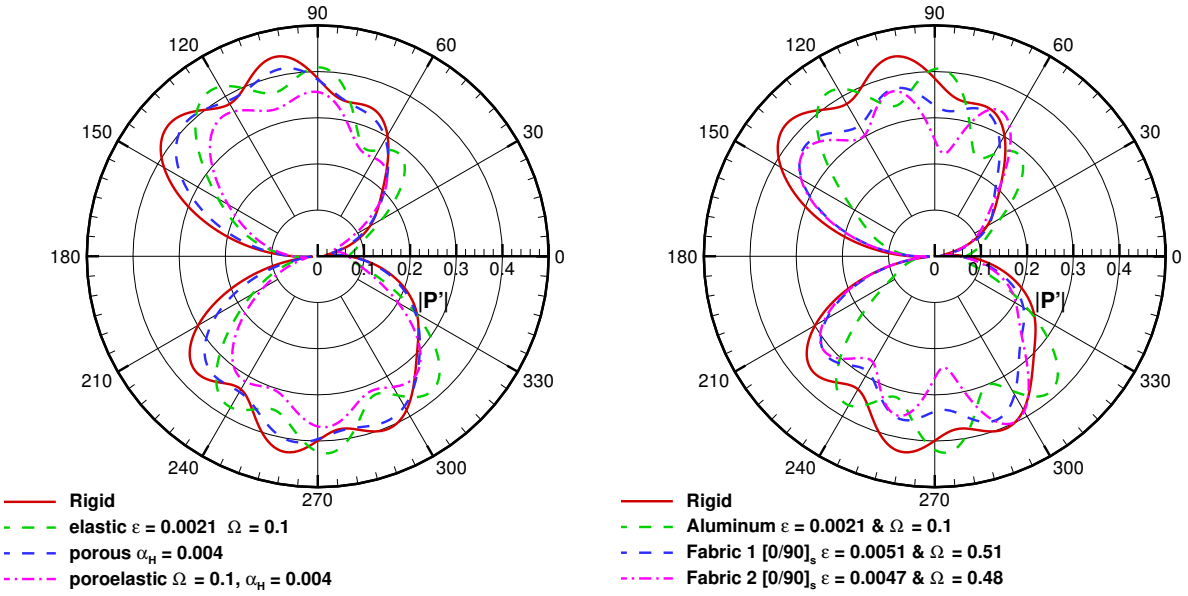

(a) Aluminum plate.

(b) Cross-ply $[0/90]_s$.

Figure 4.23: Directivities for high aspect ratio plates for $k_0 = 10$ and different fabrics.

a comparison of the pressure directivities computed for the composite and aluminum (elastic) plates, and for a rigid plate. One can see that the plates made of the symmetric laminate cross-ply $[0/90]_s$ present a more pronounced noise reduction than both the rigid and the aluminum plates. Here, the materials fabric 1 and fabric 2 have weak and strong degrees of orthotropy, respectively (see Table 4.7 for details). Even though the laminates have the same stacking sequence, the ratio between the elasticity properties E_{11}/E_{22} leads to a preferential direction for the elastic waves, modifying the fluid-structure mechanisms of sound radiation. As can be observed in the figure, the plate configuration employing the fabric 2 (stronger orthotropy) material provides a further noise reduction for directivity angles perpendicular to the plate surface compared to those from fabric 1.

Figure 4.24 presents the total acoustic pressure signatures and the displacement fields for the aluminum and composite plates. The porosity (when applicable) and elasticity parameters are the same as before. In Fig. 4.24 (a), one can see that, for the rigid plate, the acoustic waves follow a quasi one-dimensional pattern along the span of the plate. Figures 4.24 (b) and (d) show the pressure signature for the poro-elastic and elastic aluminum plates. The wave patterns are similar and one can see that high-order acoustic modes are excited due to the surface displacement of the elastic plates. The effects of porosity do not seem to modify the overall wave acoustic propagation along the plates between both plates. Similarly to the previous results discussed in §4.3, the rapid pressure

oscillations along the plate surface should lead to a destructive interference in the acoustic field. However, this interference is not as pronounced as before for the square plates.

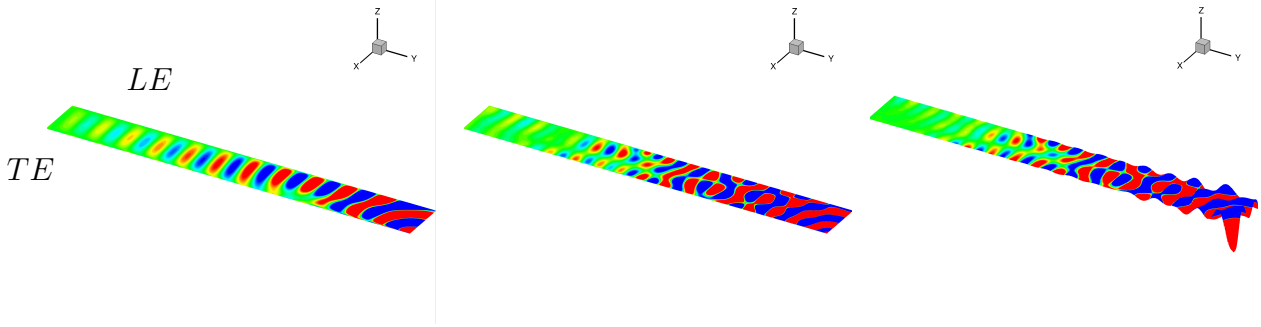

(a) Total pressure along rigid plate

(b) Total pressure along poro-elastic plate

(c) Displacement along poro-elastic plate

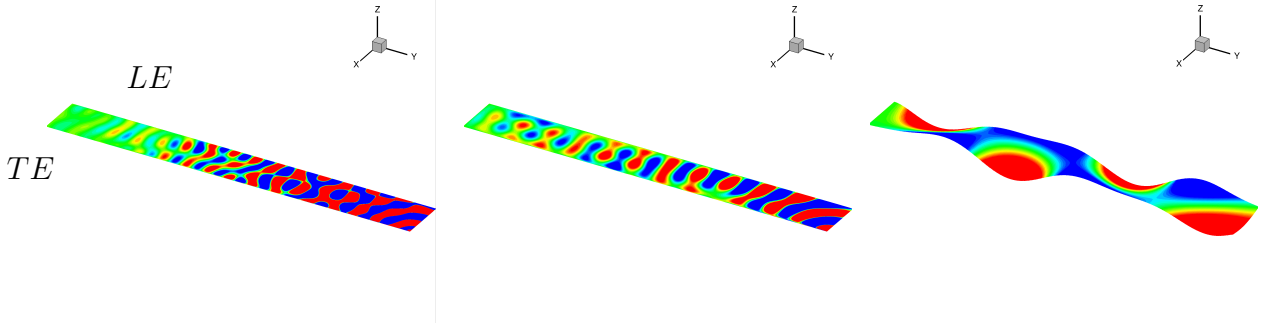

(d) Total pressure along elastic aluminum plate

(e) Total pressure along laminate cross-ply $[0/90]_s$

(f) Displacement along laminate cross-ply $[0/90]_s$

Figure 4.24: Total acoustic pressure and displacement for aluminum and laminate cross-ply $[0/90]_s$ plates for $k_0 = 10$ and fabric 2.

As discussed before, the porosity effects are not evaluated for the composite materials. Therefore, the results obtained for the elastic aluminum plate in Fig. 4.24(d) are used as a reference to compare with those obtained for the composite material (fabric 2) in Fig. 4.24(e). One can see that the directional effects of the laminate cross-ply [0/90] plate in Fig. 4.24(e) produce a different acoustic signature for this stacking sequence of layers, comparing to the aluminum plate. For the composite plate, the noise reduction is more prominent as observed in the directivity plot. In Fig. 4.24(f), it is possible to observe the displacement of the plate for the laminate cross-ply [0/90] for fabric 2. Clearly, lower frequency modes are excited for the composite plate although they do not appear in a clear fashion for the surface acoustic pressure.

In order to perform a further assessment of the effects of composite materials on the noise scattering of elastic plates, different laminated materials are investigated. Figure 4.25 shows results for four configurations of symmetric laminated plates with two different materials (fabric 1 and 2), in which the fluid loading parameters are distinct as shown in Tables 4.8 - 4.9. For the cross-ply $[90/0]_s$ configuration, the directivities are

shown in Fig. 4.25(a), compared to the rigid and aluminum plates. For both composite plates, a reduction in the scattered noise is observed. Fabric 1 and 2 seems to lead to similar results in the far-field radiation, differently from the $[0/90]_s$ stacking sequence.

The quasi-isotropic plates are chosen to have isotropic extensional stiffness. However, their bending stiffnesses are not isotropic, having a maximum near the direction of the outermost layers. Figures 4.25(b) and (c) show the directivities for the quasi-isotropic A and B laminates. Both elatic plates provide a reduction in the far-field noise scattering compared to the rigid plate and the elastic aluminum plate. The quasi-isotropic C plate has the minimum bending stiffness in the chordwise direction for the fabrics studied and the results obtained for this configuration show differences compared to the other quasi-isotropic ones. For example, fabric 1 has a weak degree of orthotropy for laminate plate C and it presents the worst efficiency in noise reduction compared to the others laminates. In fact, the directivity plot for this case shows an increase in the scattered main lobe upstream the plate relative to the rigid plate. On the other hand, the results for fabric 2, which has a strong degree of orthotropy, have the most pronounced noise reduction in the upstream direction compared to all other configurations analyzed. Hence, the current study shows that the composite materials can be designed in terms of degree of orthotropy and stacking sequence to mitigate sound scattering, as well as the plate thickness.

Figure 4.26 presents the total acoustic pressure and displacement for several laminate plates for $k_0 = 10$ considering fabric 2. Figures 4.26(a), (b) and (c) present the acoustic signature for the quasi-isotropic A, B and C laminates, respectively. The signatures of acoustic pressure on the surface are modificated by the anisotropy of the materials as can be see in the regions approaching the clamped edge. These modifications occur due the flexural waves that propagate along the structure. The displacement fields for the three plates can be observed in Figs. 4.26(d), (e) and (f).

The results presented so far show directivity plots computed for observers positioned at the mid-span plane of the plates. In order to assess the overall radiated sound for all directions, we employ the same procedure of §4.3 and compute the sound power level (PWL) for the different composite plates investigated. Figures 4.27 - 4.29 presents the integrated sound power level, PWL, computed over a spherical surface at a radial distance of 50 L from the center of the plate $(x, y, z) = (0.5, 0.0, 0.0)$. The values shown in the figures present the reduction in the PWL compared to the rigid plate which is used as reference. The Helmholtz numbers k_0 vary from 1 to 10 and it is possible to see the influence of elasticity for the different composite materials, for low and high frequency acoustic excitations.

Figure 4.27(a) shows results for the aluminum plate. In a comparison with the

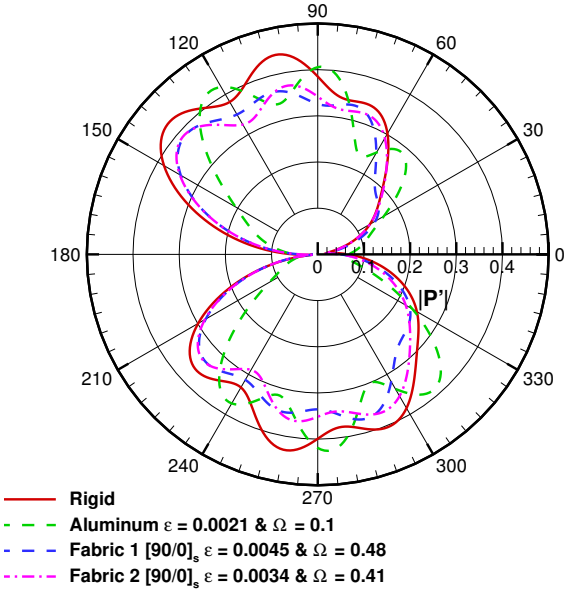

(a) Cross-ply $[90/0]_s$.

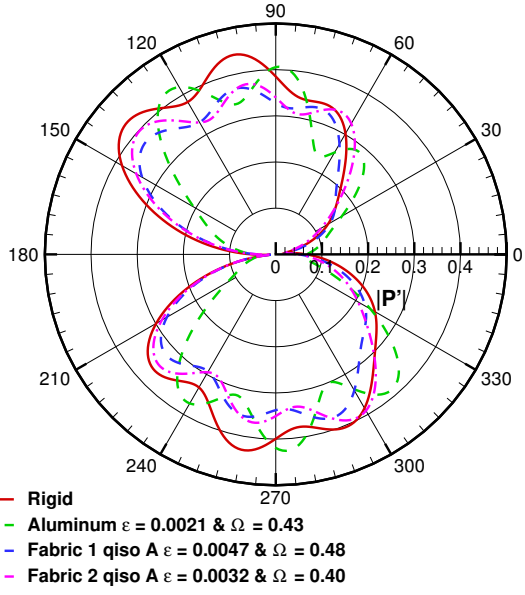

(b) Quasi-isotropic A.

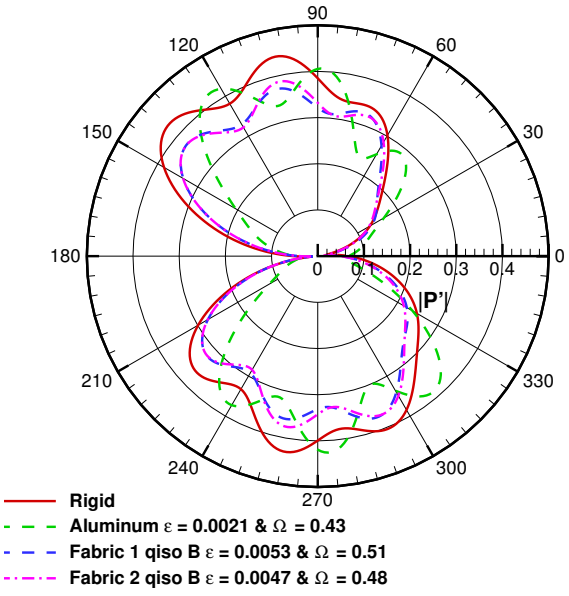

(c) Quasi-isotropic B.

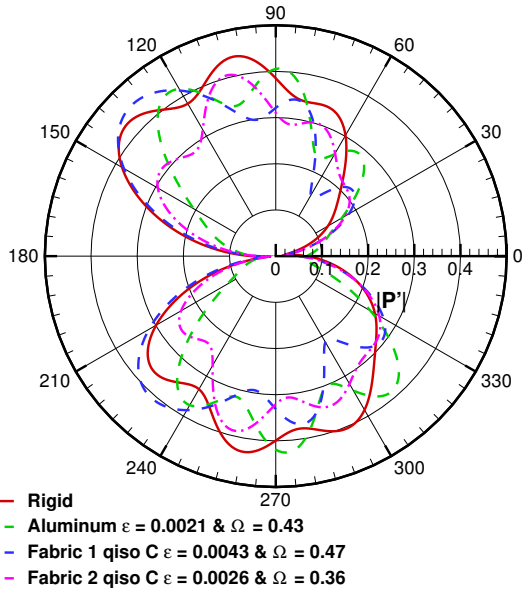

(d) Quasi-isotropic C.

Figure 4.25: Directivities for high aspect ratio plates for laminate cross-ply $[0/90]_s$ and quasi-isotropic plates with different fabrics.

rigid-impermeable plate, the total sound power level is reduced when porosity is applied. The previous directivity plots show that elasticity leads to modification in the radiated sound computed at the mid-span plane for $k_0 = 10$, leading to a slight reduction in the scattered noise. However, when we compute the total sound power level for several frequencies, we observe a reduction in the PWL at low frequencies and an increase in PWL at moderate and high frequencies. For a high aspect ratio plate, the natural frequencies of

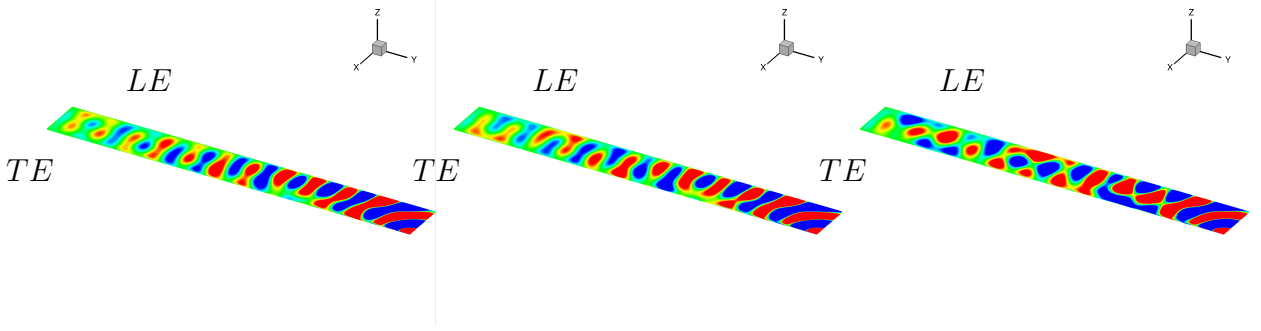

(a) Quasi-isotropic A plate (b) Quasi-isotropic B plate (c) Quasi-isotropic C plate

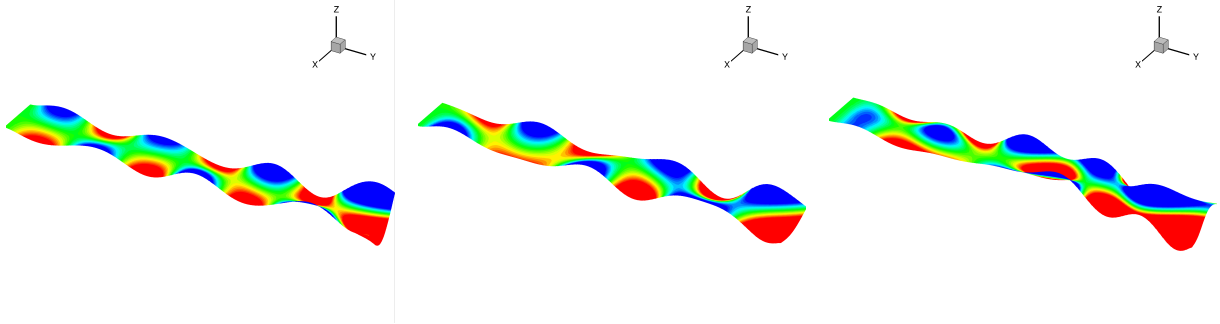

(d) Quasi-isotropic A plate (e) Quasi-isotropic B plate (f) Quasi-isotropic C plate

Figure 4.26: Total acoustic pressure (top row) and displacement (bottom row) for different laminate plate configurations for $k_0 = 10$ and fabric 2.

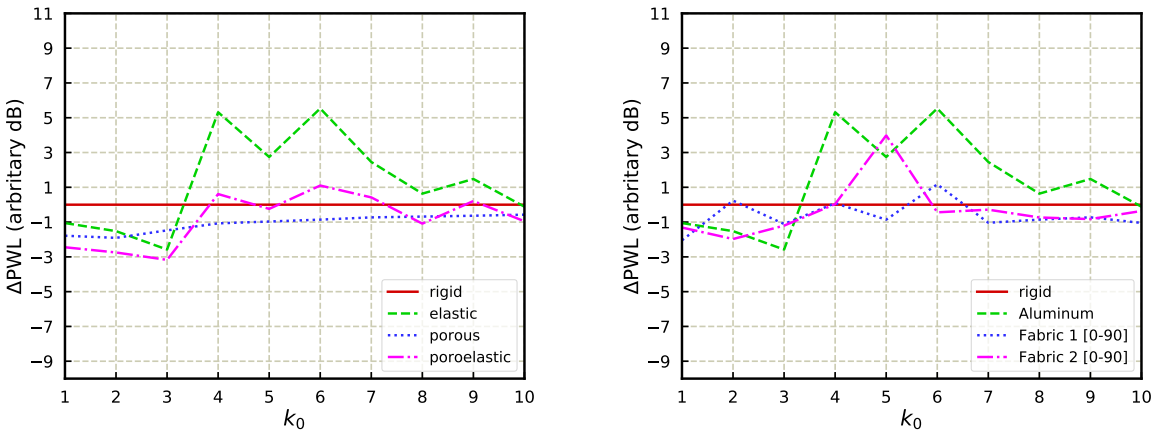

(a) Aluminum plate. (b) Laminate cross-ply $[0/90]_s$ plate.

Figure 4.27: Effects of porosity and elasticity on sound power level reduction, ΔPWL, for different plates.

the vibration modes become closer as the frequency increases. Hence, for these cases, the plate is excited at frequencies close to resonance which cause a constructive interference between acoustic waves created by the flexural waves reaching the edges and corners of the plate. For $k_0 = 4$ and $k_0 = 6$, one can see peaks of PWL in Fig. 4.27(a) indicating that noise scattering is indeed increased due to these resonances. Although for previous

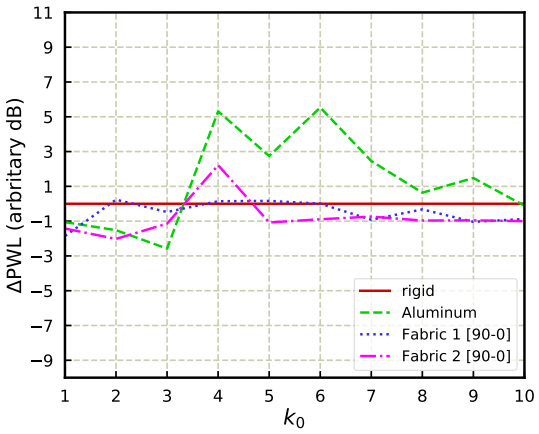

(a) Laminate cross-ply $[90/0]_s$ plate.

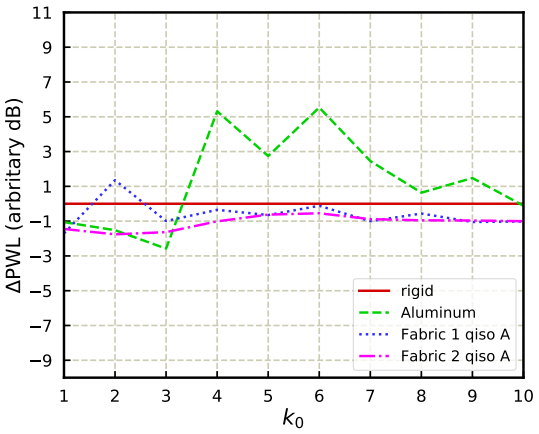

(b) Lamimate quasi-isotropic A plate.

Figure 4.28: Effects of elasticity on sound power level reduction, ΔPWL, for different plates.

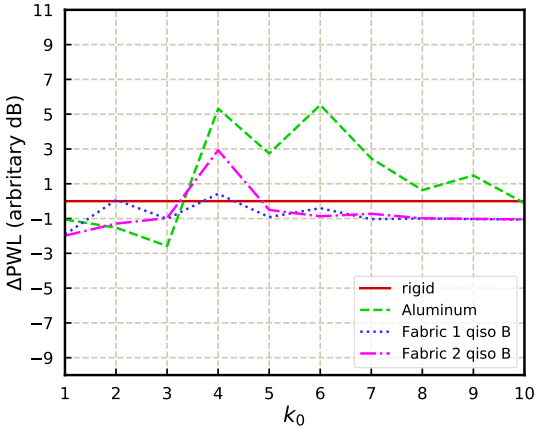

(a) Lamimate quasi-isotropic B plate.

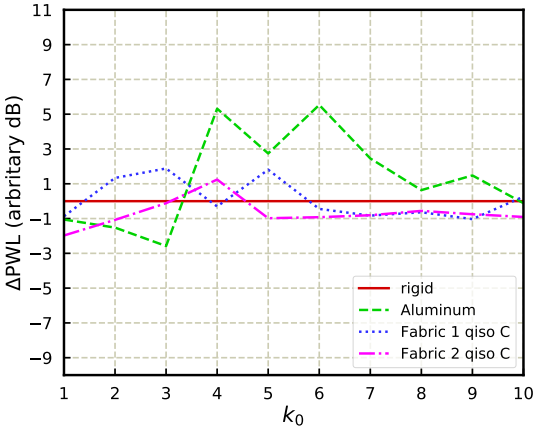

(b) Lamimate quasi-isotropic C plate.

Figure 4.29: Effects of elasticity on sound power level reduction, ΔPWL, for different plates.

cases elasticity was efficient in reducing the noise scattering in the high-frequency range, for the current configuration, the trends are different. On the other hand, the poro-elastic plate shows that the resonance peaks are attenuated by porosity.

In order to analyze the effective noise variations of the plates of composite materials, the sound power level is computed for each individual laminate plate considering both fabrics 1 and 2. In Fig. 4.27(b), one can see the results for the laminate cross-ply $[0/90]_s$ plates. Fabric 1 is more efficient in terms of noise reduction noise for higher frequencies while fabric 2 presents better results at lower frequencies. Fabric 2 also presents a resonance peak at $k_0 = 5$. Overall, the noise reduction of the composite plates is more prominent than that of the aluminum plate. However, the results are similar to those

obtained for the rigid plate model.

The stacking sequence is an important parameter to understand how composite materials can modified the radiated sound. Figure 4.28(a) shows the results for laminate cross-ply $[90/0]_s$ plate using fabrics 1 and 2. Modifying the stacking sequence from $[0/90]_s$ to $[90/0]_s$ in the laminate slightly improves the efficiency in terms of PWL. For example, the resonance peak has a lower peak value for the $[90/0]_s$ laminate with fabric 2 and its frequency is shifted to a lower frequency, at $k_0 = 4$. Similar considerations can be made for fabric 2 in a comparison for the different stacking sequences. Figure 4.28(b) shows the sound power levels for the laminate quasi-isotropic A for fabrics 1 and 2. Here, fabric 2 leads to a noise reduction for the entire range of frequencies while fabric 1 shows a peak for $k_0 = 2$ due to resonance.

Figures 4.29(a) and (b) present the results for laminates quasi-isotropic B and C, respectively. For the former case, fabrics 1 and 2 provide similar results in terms of PWL reduction for high frequencies. The most considerable difference for this case is observed for $k_0 = 4$ in Fig. 4.29(a) where fabric 2 presents an increase in the scattered noise compared with fabric 1, due to a more pronounced resonance effect. In Fig. 4.29(b), one can see that fabric 2 leads to a better performance than fabric 1 in terms of noise reduction, especially at lower frequencies. It is important to highlight that all composite materials investigated in this section lead to noise reductions when compared with the aluminum plate. Despite of the five different laminates studied, the results show that the improvements in terms of noise reduction are similar. The choice of laminate and fabric impact directly in the fluid loading parameters and can be optimized to reduce the level of noise scattered for a broad range of frequencies. The noise reductions are small for the current high aspect ratio plate analyzed. However, more prominent noise reductions could be obtained for similar plate configurations excited by different acoustic sources. In the present case, the source mainly excites the chordwise diretion of the plate. If a source was placed along the lateral edge of the plate, parallel to the clamped edge, exciting the plate along the spanwise direction, we believe that the noise reductions would be more effective. In this case, the application of specific stacking sequences and fabrics would lead to more appealing results by composite materials.

4.9 Plates submerged in water

The investigation of plates submerged in water represent another interesting application of the current numerical framework. Noise reduction in submarines and underwater gliders are possible applications for such studies. Up to here, all cases analysed are performed considering plates immersed in air (except along the validation section

presented before). In this section, we would like to evaluate the effects of elasticity in underwater applications, where a stronger fluid structure interaction occurs.

Fluid properties, such as, density and speed of sound, directly affect the fluid loading parameters on the surface of the structures. Sound travels in water about 4.3 times faster than in air and the density of the water is around 1000 times higher than that of air. Therefore, structures submerged in water have a stronger coupling between bending waves and acoustic waves, leading to a heavy fluid pressure loading (Howe, 1998). In order to simulate the current configurations of underwater acoustic scattering, we had to increase the imaginary component of Ω to avoid singularities at resonances. This was a necessary feature to obtain convergence using the present iterative linear solver CGS, described in the numerical methods section. For all cases analyzed above $k_0 = 4$, the imaginary component of Ω was set equal to 10% of its real value Ω. For lower frequencies, the imaginary component had to be increased to 15% of the real value of Ω.

Figure 4.30 presents directivity plots for plates of aluminum and symmetric laminate cross-ply $[0/90]_s$ with fabrics 1 and 2 for $k_0 = 10$. The plates are squared, clamped along the leading edge, excited by a a point quadrupole source placed at the trailing edge. Hence, the configurations are similar to those studied in §4.3, however, now, the fluid under consideration is water. For the aluminum plate, the effects of porosity and elasticity are individually assessed considering $\Omega = 0.21$, $\alpha_H = 0.004$ and $R = 0.001$. The thickness of the plate is fixed in $0.004\tilde{L}$ and the fluid loading parameters are computed for each material as shown in Tables 4.10 - 4.11.

In Fig. 4.30(a), porosity provides a moderate reduction in the sound scattered, being more effective in upstream direction. Such results are similar, in terms of magnitude of noise reduction, to those obtained for a plate immersed in air. However, as can be also observed in Fig. 4.30(a), elasticity effects present much more effective reductions in the scattered noise compared to those of plates immersed in air. This is due to the stronger interaction of the flexural waves with the sound waves. Figure 4.30(b) shows a comparison in terms of pressure directivities between the aluminum and laminate cross-ply $[0/90]_s$ plates. The composite plates are investigated for fabrics 1 and 2. From this figure, one can see that the composite plates provide further reductions in the far-field scattered noise. For these laminates, the fluid loading parameters are very high for both fabrics and the degrees of orthotropy do not change the scattered sound significantly.

Figure 4.31 presents the total acoustic pressure and displacement for both the aluminum and composite plates for $k_0 = 10$ due to a point quadrupole source placed at the trailing edge. The total acoustic pressure for a rigid plate is also shown (Fig. 4.31(a)) and, similarly to the plate immersed in air, secondary diffraction occurs at the leading and lateral edges. The acoustic pressure for a poro-elastic aluminum plate is shown in

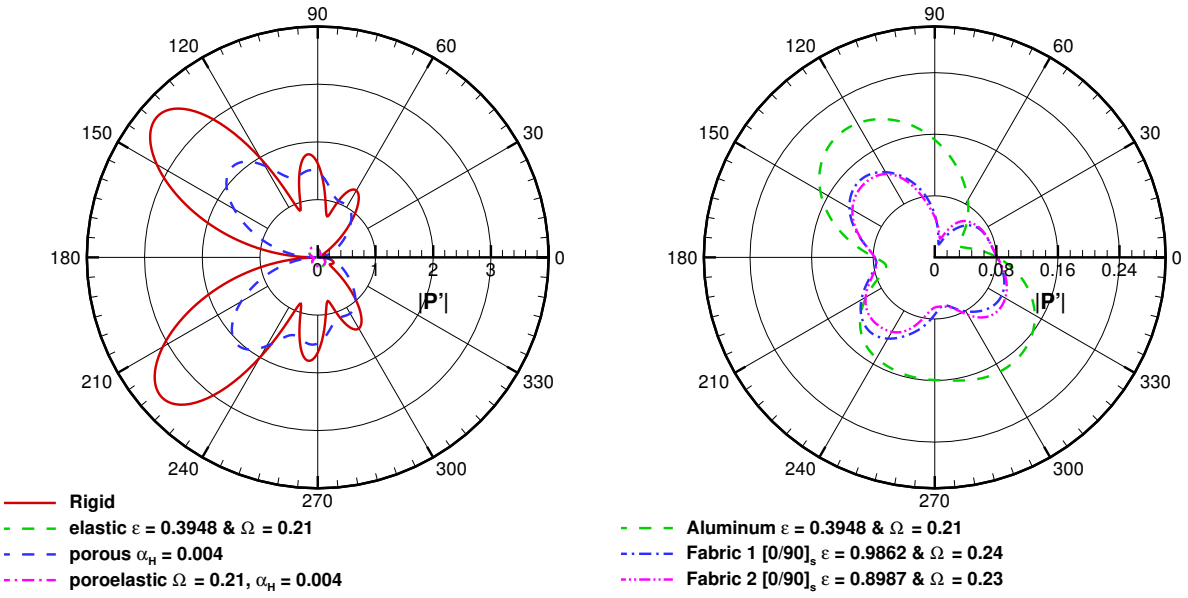

(a) Aluminum plate.

(b) Cross-ply $[0/90]_s$.

Figure 4.30: Pressure directivities for different plates and $k_0 = 10$.

Fig. 4.31(b) and it is possible to see that the acoustic signature on the plate surface is totally modified by porosity and elasticity effects. Considering that the current model has damping effect due to the imaginary value of Ω, one should expect that the waves would attenuate along the plate surface, which is observed in the displacement of the bending waves along the poro-elastic plate in Fig. 4.31(c). For this case, the elastic waves do not hit on the leading edge and, therefore, do not produce a secondary diffraction mechanism. Clearly, the acoustic waves on the plate surface follow the displacement field and, therefore, the overall effect is a destructive interference that leads to a noise reduction in the far field.

Figure 4.31(d) shows the total acoustic pressure along the aluminum plate, which is similar to the solution obtained by the poro-elastic plate. This solution is used as a reference to compare with those obtained by the composite materials. One advantage to use composite materials is that the directional effects of the stacking sequence of layers, combined with the degree of orthotropy of the material, can change the propagation of the bending waves along the plate. In Fig. 4.31(e), one can see the acoustic signature on the surface of the laminate cross-ply [0/90] plate. Here, it is possible to compare the solution with that of the aluminum plate. One can observe the directional effects of the laminate on the displacement field (Fig. 4.31(f)) and, consequently, in the acoustic field.

Figure 4.32 presents the integrated sound power level, PWL, computed over a spherical surface at a radial distance of 50 L from the center of the plate. The values shown in

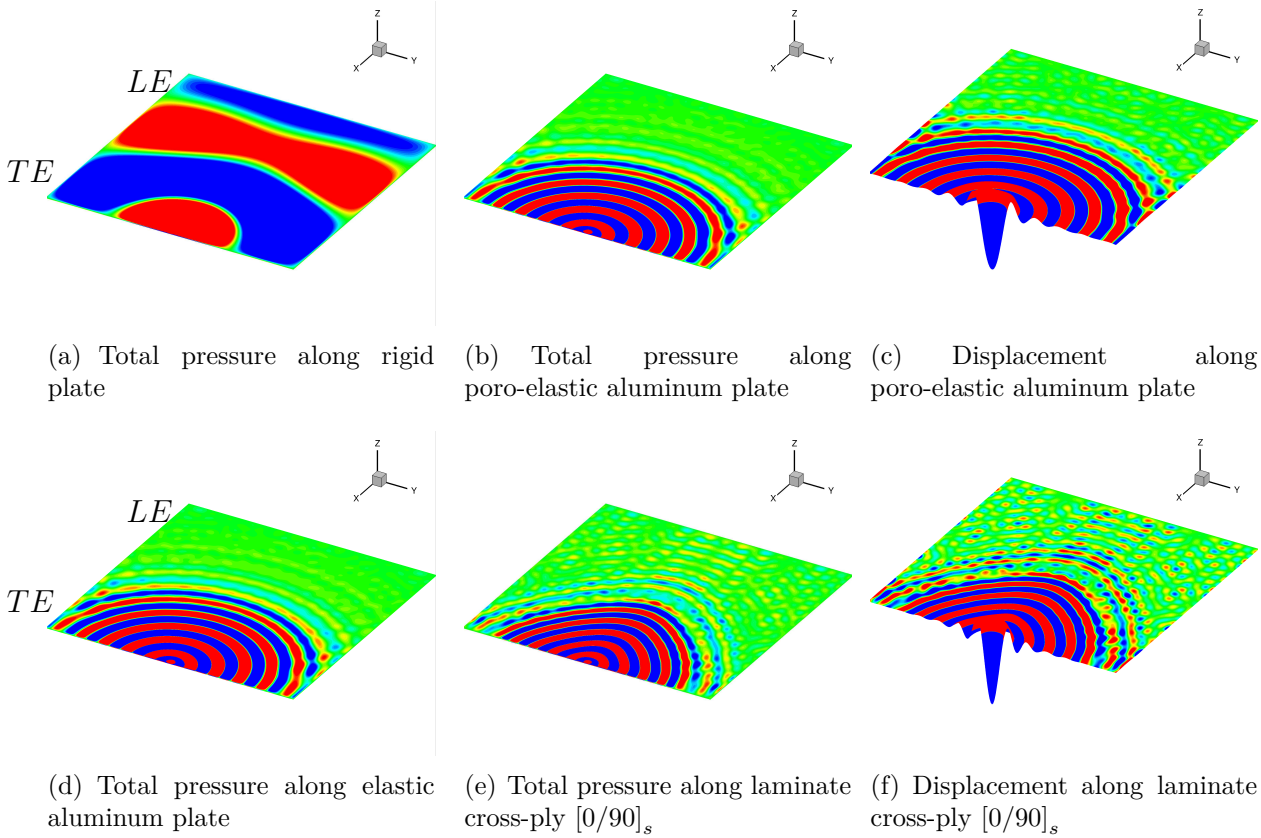

(a) Total pressure along rigid plate

(b) Total pressure along poro-elastic aluminum plate

(c) Displacement along poro-elastic aluminum plate

(d) Total pressure along elastic aluminum plate

(e) Total pressure along laminate cross-ply $[0/90]_s$

(f) Displacement along laminate cross-ply $[0/90]_s$

Figure 4.31: Total acoustic pressure and plate displacement for aluminum plate and laminate crossply $[0/90]_s$ plate with fabric 2 for $k_0 = 10$.

the figures represent the reduction in the PWL compared to the rigid plate, which is used as reference. The Helmholtz numbers k_0 vary from 3 to 10 for the current case with heavy fluid loading parameters. Figure 4.32(a) shows the results for the aluminum plate. Porosity leads to a moderate noise reduction when compared to the rigid-impermeable plate, with more pronounced reductions at low frequencies, as expected. Here, the heavy fluid pressure loading on the surface leads to a strong dependence of the elasticity. For underwater applications, we can see that the interaction of bending and acoustic waves can drastically reduce the sound scattering. Figure 4.32(a) shows that the sound power level reduction for elastic plates is much more effective for submerged plates. Hence, both poro-elastic and elastic plates present identical results in terms of PWL.

Figure 4.32(b) shows the results for the laminate cross-ply $[0/90]_s$ plates with fabrics 1 and 2 compared to the aluminum plate. The composite plates studied provide a further reduction in PWL compared to the aluminum plate once the directional effects of the laminates in the bending waves appear to improve the interaction with acoustic waves, leading to a further noise reduction. Both fabrics analyzed produce the same results in terms of PWL.

The acoustic pressure fields computed in the mid-span position are shown in Fig.4.33

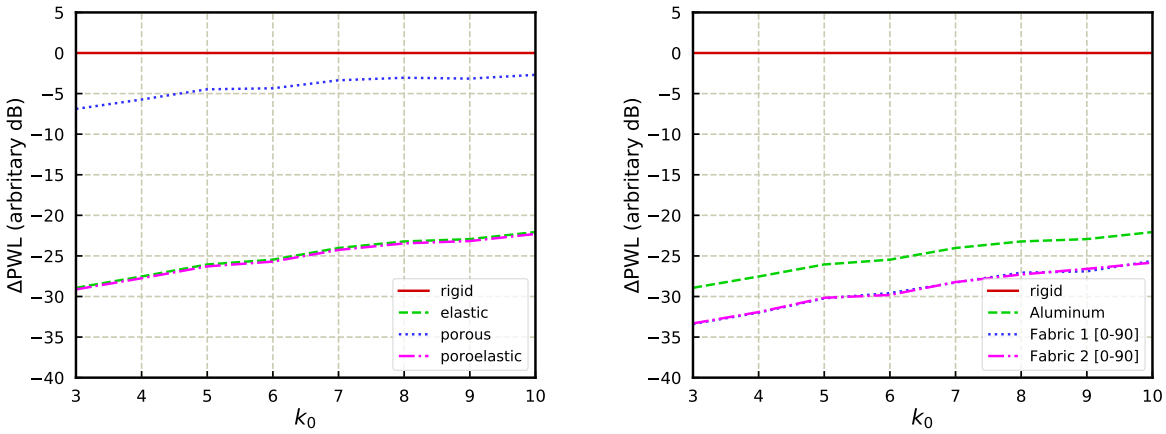

(a) Aluminum plate.

(b) Laminate cross-ply $[0/90]_s$ plates.

Figure 4.32: Effects of elasticity on sound power level reduction, ΔPWL, for different plates.

for the rigid, aluminum and laminate crossply $[0/90]_s$ plates. The plates are submerged in water and the Helmholtz number is $k_0 = 10$. Figure 4.33(a) presents the acoustic field for the rigid plate and it shows the typical trailing-edge scattering pattern with a strong upstream radiation. Figures 4.33(b) and (c) show the results for the aluminum and composite plates, respectively. It is possible to observe the bending waves propagating along the plate surface and being attenuated by the damping due to the imaginary part of Ω. For the elastic plates, the acoustic field is almost imperceptible due to the reduction in noise scattering. The outgoing waves for this material is less than aluminum one. One should see that the plots are shown for the same levels of pressure contours. This demonstrates that the application of elastic trailing edges for underwater configurations results in considerable reductions in the noise radiation. This is a topic for future investigation and we demonstrate that the current numerical framework can be employed for such study.

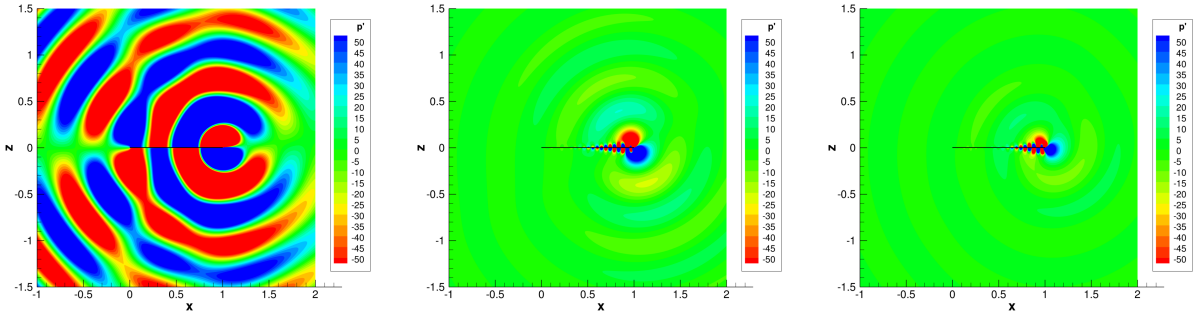

(a) Rigid plate.

(b) Aluminum plate.

(c) Laminate cross-ply $[0/90]_s$ plate.

Figure 4.33: Acoustic pressure field computed in the mid-span for different plates submerged in water.

5 CONCLUSIONS

We present a numerical framework to compute the acoustic scattering by isotropic and anisotropic materials for arbitrary geometries. An existing structural model is recast in terms of the modal basis from the associated free-vibration problem which is solved by a finite element method or a pseudo-spectral method. The model enables a fully coupled solution of the fluid-structure interaction problem through coupling of boundary conditions in the acoustic formulation which is solved by a boundary element method, BEM. The BEM is implemented together with a multi-level adaptive wideband fast multipole method, FMM, to accelerate the solution of the large dense linear systems arising from the boundary integral equations.

In the present methodology, it is possible to study the acoustic scattering by fully three-dimensional structures including elasticity and porosity effects, isolated or combined. Several structural configurations with free and/or clamped edges can be analyzed for plates with arbitrary geometries including swept trailing edges and serrations. An investigation of acoustic scattering by a point quadrupole source is provided for a range of frequencies and we show that elasticity is more efficient in reducing the far field noise radiation at high acoustic frequencies. This effect is more evident if high-frequency bending waves are excited on the structural problem. On the other hand, results show that porosity is more efficient in reducing the scattered noise at low frequencies.

The present numerical framework is validated by a comparison of solutions obtained by the 3D plates submerged in water with those obtained by 2D plates. In this analysis, a proper scaling is performed to compare the solutions and it is shown that elasticity effects are less efficient for plates of lower aspect ratios.

The study of acoustic scattering by trapezoidal plates shows that swept trailing edges lead to a considerable noise reduction for low and high acoustic frequencies. In this sense, the sweep angle changes the acoustic signature along the plate through an alignment of the scattered field with the direction perpendicular to the trailing edge. It is shown that the noise reduction from elasticity is caused by a destructive interference of the acoustic surface pressure induced by the plate displacement. When elasticity and porosity are combined with a swept trailing edge, a further reduction in the far-field scattered sound power level is observed when compared to that from a poro-elastic square plate.

The present methodology allows the analysis of noise scattering from general compact and non-compact acoustic sources. A non-compact turbulent jet wavepacket source model is employed in a jet-installation problem including rigid and poro-elastic plates with swept

trailing edges. The present study shows that sweep leads to a major reduction of the scattered far-field pressure reducing the magnitude of the secondary lobes above and below the plate. For rigid plates, the acoustic waves are scattered towards the plate sideline due to sweep. However, for the poro-elastic plate the scattered waves along the surface are still aligned with the jet excitation through displacement of the elastic waves.

The numerical framework is employed in the study of acoustic scattering from poro-elastic plates with trailing-edge serrations. Results demonstrate that the serrations provide a considerable noise reduction for a spanwise-correlated quadrupole source placed close to a rigid trailing edge. The poro-elastic case including serrations leads to a further reduction in the far-field noise radiation.

The reduction in noise scattering by a high aspect ratio plate is investigated to represent real applications such as those found in helicopter rotor blades and aircraft wings. For this case, a source is placed at the wing tip to represent the noise generated by wing-tip vortices. Different composite materials are analyzed in order to assess the performance of the stacking sequences of layers for symmetric laminates. The degrees of orthopropy of different fabrics are also studied. The results indicate that the right choice of the fabric and laminate can lead to a better performance of the fluid structure interaction problem leading to more pronounced noise reductions. In general, the composite plates studied present more effective reductions in the sound radiation when compared to similar aluminum plates.

Finally, the methodology is applied to study a problem where a plate is submerged in water. This analysis allows an assessment of the numerical framework to an important fluid structure interaction problem where the fluid loading parameters are heavy. Results show that porosity and elasticity are efficient mechanisms to reduce noise scattering by plates submerged in water. In this context, elasticity is a very effective mechanism of noise reduction due to the strong coupling between bending and acoustic waves. The application of composite materials shows that further noise reductions can be achieved when compared to isotropic materials. In the former case, directional properties of the laminates can impact on the propagation of the bending waves and, therefore, on the interference of acoustic waves via a destructive interference effect which would lead to a far-field cancellation of the scattered noise.

5.1 Suggestions for Future Work

Below, we present suggestions for further developments and applications of the present numerical framework.

- The proposed methodology can be employed for the design of devices with low acoustic signature, for example, drones, rotor blades, high-lift systems, and submarine systems. In this sense, it could be coupled with tools of multidisciplinary design optimization (MDO) to achieve particular solutions including the application of composite materials and metamaterials. For example, gradient-based optimization with adjoint methods for sensitivity analysis are promising approaches to improve the present numerical framework.

- The methodology could be extended for the study of metallic and composite materials for thicker plates. Here, one could use, for example, less restrictive structural models and theories of isotropic and laminated composite plates. Along the same ideas, other models of porosity could be employed. For example, more accurate models would be able to specify parameters such as porosity, tortuosity and resistivity of the materials.

- In aeronautical applications, flow effects may modify the scattering of acoustic waves. The inclusion of flow effects to the current formulation would allow the assessment of the Mach number effects on the noise reduction by poro-elastic trailing edges. One possibility that can be implemented is the Prandtl-Glauert transformation of the spatial variables that will lead to a Helmholtz equation with a modified wavenumber.

- In the present work, we employed model sources representative of turbulent eddies and a turbulent jet. The current numerical framework could also be used together with other models of engineering sources. In this case, semi-analytical and semi-empirical models could be developed for representing turbulent boundary layers developing along the plate surface. One could employ, for example, surface pressure spectra obtained in the proximity of the trailing edge to obtain the magnitude of the incident field excitations.

References

ABREU, L.I.; CAVALIERI, A.V.G. and WOLF, W.R. Coherent hydrodynamic waves and trailing-edge noise. In **AIAA Aeroacoustics Conference**. American Institute of Aeronautics and Astronautics, 2017.

ANDERSON, J.D. and WENDT, J. **Computational fluid dynamics**, vol. 206. Springer, 1995.

ANSYS. **ANSYS® Academic Research Mechanical, Release 17.0**. ANSYS, Inc., Release 17.0.

ASSIER, R.C. and PEAKE, N. On the diffraction of acoustic waves by a quarter-plane. **Wave Motion**, vol. 49, 64–82, 2012.

AYTON, L.J. Acoustic scattering by a finite rigid plate with a poroelastic extension. **Journal of Fluid Mechanics**, vol. 791, 414–438, 2016.

BACHMANN, T.; WAGNER, H. and TROPEA, C. Inner vane fringes of barn owl feathers reconsidered: morphometric data and functional aspects. **Journal of Anatomy**, vol. 221, n. 1, 1–8, 2012.

BARDELL, N.S. Free vibration analysis of a flat plate using the hierarchical finite element method. **Journal of sound and vibration**, vol. 151, n. 2, 263–289, 1991.

BOYD, J.P. **Chebyshev and Fourier spectral methods**. Dover, 2001.

CARRIER, J.; GREENGARD, L. and ROKHLIN, V. A fast adaptive multipole algorithm for particle simulations. **SIAM journal on scientific and statistical computing**, vol. 9, n. 4, 669–686, 1988.

CAVALIERI, A.V.G.; JORDAN, P.; COLONIUS, T. and GERVAIS, Y. Axisymmetric superdirectivity in subsonic jets. **Journal of Fluid Mechanics**, vol. 704, 388, 2012.

CAVALIERI, A.V.G.; JORDAN, P.; WOLF, W.R. and GERVAIS, Y. Scattering of wavepackets by a flat plate in the vicinity of a turbulent jet. **Journal of Sound and Vibration**, vol. 333, 6516–6531, 2014a.

CAVALIERI, A.V.G.; WOLF, W.R. and JAWORSKI, J.W. Acoustic scattering by finite poroelastic plates. In **20th AIAA/CEAS Aeroacoustics Conference**. 2014b.

CAVALIERI, A.V.G.; WOLF, W.R. and JAWORSKI, J.W. Numerical solution of acoustic scattering by finite perforated elastic plates. **Proceedings of the Royal Society A**, vol. 472, 20150767, 2016.

CECKA, C. and DARVE, E. Fourier-based fast multipole method for the Helmholtz equation. **SIAM Journal on Scientific Computing**, vol. 35, n. 1, A79–A103, 2013.

CHEN, K.; LIU, Q.; LIAO, G.; YANG, Y.; REN, L.; YANG, H. and CHEN, X. The sound suppression characteristics of wing feather of owl (bubo bubo). **Journal of Bionic Engineering**, vol. 9, n. 2, 192–199, 2012.

CHENG, H.; CRUTCHFIELD, W.Y.; GIMBUTAS, Z.; GREENGARD, L.F.; ETHRIDGE, J.F.; HUANG, J.; ROKHLIN, V.; YARVIN, N. and ZHAO, J. A wideband fast multipole method for the Helmholtz equation in three dimensions. **Journal of Computational Physics**, vol. 216, n. 1, 300–325, 2006.

CIPRA, B.A. The best of the 20th century: Editors name top 10 algorithms. **SIAM news**, vol. 33, n. 4, 1–2, 2000.

COIFMAN, R.; ROKHLIN, V. and WANDZURA, S. The fast multipole method for the wave equation: A pedestrian prescription. **IEEE Antennas and Propagation Magazine**, vol. 35, n. 3, 7–12, 1993.

CRAWLEY, E.F. The natural modes of graphite/epoxy cantilever plates and shells. **Journal of Composite Materials**, vol. 13, n. 3, 195–205, 1979.

CRIGHTON, D.G. Acoustic edge scattering of elastic surface waves. **Journal of Sound and Vibration**, vol. 22, n. 1, 25–32, 1972.

CRIGHTON, D.G. Basic principles of aerodynamic noise generation. **Progress in Aerospace Sciences**, vol. 16, n. 1, 31–96, 1975.

CRIGHTON, D.G. The 1988 rayleigh medal lecture: fluid loading—the interaction between sound and vibration. **Journal of Sound and Vibration**, vol. 133, n. 1, 1–27, 1989.

CRIGHTON, D.G. and INNES, D. The modes, resonances and forced response of elastic structures under heavy fluid loading. **Proceedings of the Royal Society of London A**, vol. 312, n. 1521, 295–341, 1984.

CRIGHTON, D.G. and LEPPINGTON, F.G. Singular perturbation methods in acoustics: diffraction by a plate of finite thickness. **Proceedings of the Royal Society of London A**, vol. 335, n. 1602, 313–339, 1973.

CURLE, N. The influence of solid boundaries upon aerodynamic sound. **Proceedings of the Royal Society of London A**, vol. 231, n. 1187, 505–514, 1955.

DARVE, E. The fast multipole method i: error analysis and asymptotic complexity. **SIAM Journal on Numerical Analysis**, vol. 38, n. 1, 98–128, 2000a.

DARVE, E. The fast multipole method: numerical implementation. **Journal of Computational Physics**, vol. 160, n. 1, 195–240, 2000b.

DEMBART, B. and YIP, E. The accuracy of fast multipole methods for Maxwell's equations. **IEEE Computational Science and Engineering**, vol. 5, n. 3, 48–56, 1998.

DICKINSON, S.M. and DI BLASIO, A. On the use of orthogonal polynomials in the rayleigh-ritz method for the study of the flexural vibration and buckling of isotropic and orthotropic rectangular plates. **Journal of Sound and Vibration**, vol. 108, n. 1, 51–62, 1986.

DOYLE, J.F. **Wave propagation in structure: spectral analysis using fast discrete Fourier transforms**. Springer-Verlag, New York, 1997.

DYM, C.L. and SHAMES, I.H. **Solid Mechanics: A Variational Approach, Augmented Edition**. Springer, 2013.

EPTON, M.A. and DEMBART, B. Multipole translation theory for the three-dimensional Laplace and Helmholtz equations. **SIAM Journal on Scientific Computing**, vol. 16, n. 4, 865–897, 1995.

FARANOSOV, G.; KOPIEV, V.; BELYAEV, I.V. and CHERNYSHEV, S. On the azimuthal structure of installed jet noise. In **23rd AIAA/CEAS Aeroacoustics Conference**. 2017.

FFOWCS WILLIAMS, J.E. and HALL, L.H. Aerodynamic sound generation by turbulent flow in the vicinity of a scattering half plane. **Journal of Fluid Mechanics**, vol. 40, n. 4, 657–670, 1970.

GATTI, P.L. and FERRARI, V. **Applied structural and mechanical vibrations: theory, methods and measuring instrumentation**. CRC Press, 2002.

GEYER, T.; SARRADJ, E. and FRITZSCHE, C. Silent owl flight: Comparative acoustic wind tunnel measurements on prepared wings. **Acta Acustica united with Acustica**, vol. 99, n. 1, 139–153, 2013.

GRACE, S.; HORAN, K. and HOWE, M. The influence of shape on the rayleigh conductivity of a wall aperture in the presence of grazing flow. **Journal of fluids and structures**, vol. 12, n. 3, 335–351, 1998a.

GRACE, S.M.; HORAN, K.P. and HOWE, M.S. The influence of shape on the Rayleigh conductivity of a wall aperture in the presence of grazing flow. **Journal of Fluids and Structures**, vol. 12, 335–351, 1998b.

GREENGARD, L. and ROKHLIN, V. A fast algorithm for particle simulations. **Journal of computational physics**, vol. 73, n. 2, 325–348, 1987.

GUMEROV, N.A. and DURAISWAMI, R. Recursions for the computation of multipole translation and rotation coefficients for the 3-d Helmholtz equation. **SIAM Journal on Scientific Computing**, vol. 25, n. 4, 1344–1381, 2004.

GUMEROV, N.A. and DURAISWAMI, R. A broadband fast multipole accelerated boundary element method for the three dimensional Helmholtz equation. **The Journal of the Acoustical Society of America**, vol. 125, n. 1, 191–205, 2009.

GYURE, M.F. and STALZER, M.A. A prescription for the multilevel Helmholtz fmm. **IEEE Computational Science and Engineering**, vol. 5, n. 3, 39–47, 1998.

HASTRITER, M.L.; OHNUKI, S. and CHEW, W. Error control of the translation operator in 3d mlfma. **Microwave and Optical Technology Letters**, vol. 37, n. 3, 184–188, 2003.

HOWE, M. On the added mass of a perforated shell, with application to the generation of aerodynamic sound by a perforated trailing edge. In **Proc. R. Soc. Lond. A**, vol. 365, pp. 209–233. The Royal Society, 1979a.

HOWE, M. On the theory of unsteady high reynolds number flow through a circular aperture. In **Proc. R. Soc. Lond. A**, vol. 366, pp. 205–223. The Royal Society, 1979b.

HOWE, M.; SCOTT, M. and SIPCIC, S. The influence of tangential mean flow on the rayleigh conductivity of an aperture. In **Proc. R. Soc. Lond. A**, vol. 452, pp. 2303–2317. The Royal Society, 1996a.

HOWE, M.S. Aerodynamic noise of a serrated trailing edge. **Journal of Fluids and Structures**, vol. 5, n. 1, 33–45, 1991.

HOWE, M.S. The compact Green's function for a semi-infinite elastic plate, with application to trailing edge noise and blade–vortex interaction noise. **The Journal of the Acoustical Society of America**, vol. 94, n. 4, 2353–2364, 1993a.

HOWE, M.S. Structural and acoustic noise produced by turbulent flow over an elastic trailing edge. **Proceedings of the Royal Society of London A**, vol. 442, n. 1916, 533–554, 1993b.

HOWE, M.S. **Acoustics of fluid-structure interactions**. Cambridge University Press, 1998.

HOWE, M.S.; SCOTT, M.I. and SIPCIC, S.R. The influence of tangential mean flow on the Rayleigh conductivity of an aperture. **Proceedings of the Royal Society of London A**, vol. 452, n. 1953, 2303–2317, 1996b.

HUGHES, I. and DOWLING, A. The absorption of sound by perforated linings. **Journal of Fluid Mechanics**, vol. 218, 299–335, 1990.

JAKOB-CHIEN, R. and ALPERT, B.K. A fast spherical filter with uniform resolution. **Journal of Computational Physics**, vol. 136, n. 2, 580–584, 1997.

JAWORSKI, J.W. and PEAKE, N. Aerodynamic noise from a poroelastic edge with implications for the silent flight of owls. **Journal of Fluid Mechanics**, vol. 723, 456–479, 2013.

JONES, L. and SANDBERG, R. Acoustic and hydrodynamic analysis of the flow around an aerofoil with trailing-edge serrations. **Journal of Fluid Mechanics**, vol. 706, 295–322, 2012.

JONES, R.M. **Mechanics of composite materials**. CRC Press, 1998.

KARIMI, M.; CROAKER, P.; KINNS, R. and KESSISSOGLOU, N. Effect of a serrated trailing edge on sound radiation from nearby quadrupoles. **The Journal of the Acoustical Society of America**, vol. 141, n. 5, 2997–3010, 2017.

KOC, S. and CHEW, W.C. Calculation of acoustical scattering from a cluster of scatterers. **The Journal of the Acoustical Society of America**, vol. 103, n. 2, 721–734, 1998.

KOC, S.; SONG, J. and CHEW, W. Error analysis for the numerical evaluation of the diagonal forms of the scalar spherical addition theorem. **SIAM journal on numerical analysis**, vol. 36, n. 3, 906–921, 1999.

LEÓN, C.A.; MERINO-MARTíNEZ, R.; RAGNI, D.; AVALLONE, F.; SCARANO, F.; PRÖBSTING, S.; SNELLEN, M.; SIMONS, D.G. and MADSEN, J. Effect of trailing edge serration-flow misalignment on airfoil noise emissions. **Journal of Sound and Vibration**, vol. 405, 19–33, 2017.

LEPPINGTON, F.G. Scattering of sound waves by finite membranes and plates near resonance. **The Quarterly Journal of Mechanics and Applied Mathematics**, vol. 29, n. 4, 527–546, 1976.

LEPPINGTON, F.G. Acoustic scattering by membranes and plates with line constraints. **Journal of Sound and Vibration**, vol. 58, n. 3, 319–332, 1978.

LEPPINGTON, F.G.; BROADBENT, E.G.; HERON, K.H. and MEAD, S.M. Resonant and non-resonant acoustic properties of elastic panels. I. the radiation problem. **Proceedings of the Royal Society of London A**, vol. 406, n. 1831, 139–171, 1986.

LEPPINGTON, F.G. and LEVINE, H. Reflexion and transmission at a plane screen with periodically arranged circular or elliptical apertures. **Journal of Fluid Mechanics**, vol. 61, n. 1, 109–127, 1973.

LISEIKIN, V.D. **Grid Generation Methods**. 2nd ed., 2009.

MESSIAH, A. Quantum mechanics. 1981.

NARITA, Y. and LEISSA, A.W. Frequencies and mode shapes of cantilevered laminated composite plates. **Journal of Sound and Vibration**, vol. 154, n. 1, 161–172, 1992.

NISHIMURA, N. Fast multipole accelerated boundary integral equation methods. **Applied Mechanics Reviews**, vol. 55, n. 4, 299–324, 2002.

OHNUKI, S. and CHEW, W. A study of the error controllability of mlfma. In **Antennas and Propagation Society International Symposium, 2001. IEEE**, vol. 3, pp. 774–777. IEEE, 2001.

PIANTANIDA, S.; VINCENT, J.; HUBER, J.; WOLF, W.R.; JORDAN, P. and CAVALIERI, A.V.G. Scattering of turbulent-jet wavepackets by a swept trailing edge. **Journal of the Acoustical Society of America**, vol. 140, 4350–4359, 2016.

RAYLEIGH, L. **The theory of sound**, vol. 1. Dover Publications, 1945.

REDDY, J.N. **Theory and analysis of elastic plates and shells**. CRC press, 2006.

RIBEIRO, J.H.M. and WOLF, W.R. Identification of coherent structures in the flow past a NACA0012 airfoil via proper orthogonal decomposition. **Physics of Fluids**, vol. 29, n. 8, 085104, 2017.

ROGER, M. and MOREAU, S. Back-scattering correction and further extensions of Amiet's trailing-edge noise model. Part 1. Theory. **Journal of Sound and Vibration**, vol. 286, n. 3, 477–506, 2005.

ROKHLIN, V. Rapid solution of integral equations of scattering theory in two dimensions. **Journal of Computational Physics**, vol. 86, n. 2, 414–439, 1990.

SAKUMA, T. and YASUDA, Y. Fast multipole boundary element method for large-scale steady-state sound field analysis. part I: setup and validation. **Acta Acustica united with Acustica**, vol. 88, n. 4, 513–525, 2002.

SARRADJ, E.; FRITZSCHE, C. and GEYER, T. Silent owl flight: bird flyover noise measurements. **AIAA Journal**, vol. 49, n. 4, 769–779, 2011.

SONG, J.; LU, C. and CHEW, W. Multilevel fast multipole algorithm for electromagnetic scattering by large complex objects. **IEEE Transactions on Antennas and Propagation**, vol. 45, n. 10, 1488–1493, 1997.

SRINIVASAN, R.S. and BABU, B.J.C. Free vibration of cantilever quadrilateral plates. **The Journal of the Acoustical Society of America**, vol. 73, 851, 1983.

TIMOSHENKO, S.P. and WOINOWSKY-KRIEGER, S. **Theory of plates and shells**. McGraw-hill, 1959.

TREFETHEN, L.N. **Spectral methods in MATLAB**, vol. 10. SIAM, 2000.

WHITE, C.A. and HEAD-GORDON, M. Rotating around the quartic angular momentum barrier in fast multipole method calculations. **The Journal of Chemical Physics**, vol. 105, n. 12, 5061–5067, 1996.

WILLIAMS, J.E.F. The acoustics of turbulence near sound-absorbent liners. **Journal of Fluid Mechanics**, vol. 51, n. 4, 737–749, 1972.

WOLF, W.R. and LELE, S.K. Wideband fast multipole boundary element method: Application to acoustic scattering from aerodynamic bodies. **International Journal for Numerical Methods in Fluids**, vol. 67, 2108–2129, 2011.

YASUDA, Y. and SAKUMA, T. Fast multipole boundary element method for large-scale steady-state sound field analysis. part II: Examination of numerical items. **Acta Acustica united with Acustica**, vol. 89, n. 1, 28–38, 2003.

YOSHIDA, K., **Applications of fast multipole method to boundary integral equation method**, PhD Thesis, Department of Global Environment Engineering, Kyoto University, Japan, 2001.